A STUDY OF OVERPRESSURE IN THE NAVARIN BASIN, ALASKA

By

Matthew Robison

A Project Submitted in Partial Fulfillment of the Requirements

for the Degree of

Master of Science

in

Petroleum Engineering

University of Alaska Fairbanks

December 2019

APPROVED:

Dr. Vahid Atashbari, Committee Chair
Dr. Mohabbat Ahmadi, Committee Member
Dr. Obadare Awoleke, Committee Member
Dr. Abhijit Dandekar, Chair
Department of Petroleum Engineering

Abstract

The Navarin basin is a region to the west of Alaska between the Aleutian Islands and Russia. It has been identified as a potential Petroleum prospect, and exploration wells have been drilled under the ocean up to depths of 17,000 feet. The exploration of the basin was started by Russia and the United States with several exploratory wells drilled in the 1980's. The geology of the region consists of tertiary sedimentary rock deposited during the Eocene age with mudstone and siltstone from Paleogenic deposition. When dealing with such depths, it is expected that the pressure will increase beyond the hydrostatic gradient. Overpressure, when unexpected, can cause blowouts or oil spills as well as danger to the oil production workforce. Herein, the origin of overpressure in this basin is examined using the well log and geological information, and potential mechanisms responsible for generating abnormal pressure are further discussed.

In this study, extensive existing well log data are thoroughly examined and organized to facilitate the characterization of overpressure zones in the basin. As a preliminary step, well logs from eight exploratory wells in the Navarin Basin were digitized and organized as the basis of the analysis. Next, overburden pressure is determined for each applicable well in the target area by examining well log and other geological information. Then, a shale discrimination scheme is applied on the log data to differentiate clay-rich formations (that undergo mechanical compaction) from other rock types. Overpressure horizons are identified and examined through velocity, resistivity and other well logging measurements of clay-rich deposits. As such, sonic velocity vs. density and resistivity vs. density cross plots are constructed to identify signatures of different mechanisms of

overpressure. Further characterization of the origin of overpressure involves examination of the tectonics, stratigraphy and source rock in order to characterize the pore pressure regime.

Finally, pore pressure is calculated using Eaton (1974) and Bowers (1995) method are utilized to calculate pore pressure within the studied wells and degree of confidence in such calculations are examined.

Table of Contents

List of Tables

List of Figures

List of Equations

1. Introduction

Exploration and Production History

The Navarin Basin has seen little exploration due to the remote location and difficulties in exploration and production in the marine environment. The earliest recorded history of exploration in the general Bering Sea is in 1959 when the Soviet Union began to explore the onshore portions of the Anadyr basin on the western side of the Bering Sea. In the 1960's and 1970's, the Soviet Union drilled over 30 onshore exploratory and stratigraphic wells in the Anadyr basin. These initial explorations were unsatisfactory as reservoir pressures were too low probably due to tight sandstones (Turner 1984). In 1984, economic quantities of oil and gas condensate were reportedly discovered in the Anadyr Basin (an offshore basin to the west of the Navarin Basin that extends to the onshore Siberia), but specific location and volume were not published (Bour 1994). These preliminary results encouraged the exploration of the Navarin basin hydrocarbons, since the Anadyr basin and the Navarin basin share geographical proximity and tectonic history (Worrall 1991). Private Industry inspection of the Navarin Basin has been more extensive including the collection of over 90,000 miles of seismic reflection data, so industry could gain more data about economic potential of the Navarin Basin prior to the first lease sale in 1984 (Turner 1984). Before drilling of the COST well in 1983, the only other lithographic information was available by dredge and gravity core sampling. During the lease sale in 1983, a total of 1.15 Billion dollars of bids were received for the nearly one million acres area of the Navarin Basin. Since the

lease sale, seven exploratory wells have been drilled, but petroleum production has yet to occur in the Navarin Basin (Figure 1).

Figure 1. The eight exploratory wells of the Navarin Basin and their relative positions surrounding the COST 1 well (Steffy, 1991).

Project Objective

The objective of this project is to discover the origins of overpressure in the Navarin Basin. In order to accomplish the objective, the following points are discussed.

1. The regional geology of the Navarin Basin.
2. The origins of overpressure in Sedimentary Basins.
3. Possible origins of overpressure in the Navarin Basin.
4. Crossplot analysis using well log data.
5. Pore pressure prediction in the Navarin Basin.

2. Regional Geology

Introduction

The Navarin Basin is one of five basins on the Bering Sea shelf covering an area of around 32,000 square miles to the northwest of the Aleutian Islands. The exploration of the Navarin Basin began in the 1960's by Russia, and continued until the exploratory wells studied herein were drilled in the 1980's. In this chapter, the geology of the Navarin basin is described in terms of geographical setting, exploration and production history, stratigraphy, and tectonic history. In General, the stratigraphy of the basin spans from the Pliocene age to the Eocene age. The lithology is predominately sandstone, mudstone, and other sedimentary formations, although shale, clay, and coal formations exist. Tectonically, the Navarin Basin is bordered by the SE Bering fault to the south, and the NW Bering fault to the northwest.

Geographical Setting

The Navarin Basin is one of five basins on the Bering Sea shelf covering an area of around 32,000 square miles (Figure 2). The Navarin Basin is located between the 63rd line of latitude in the north and the 58th line of latitude in the south. The southern edge is located from 174 degrees longitude on the east to 180 degrees longitude on the west. The northeast is bordered by the Khatyrka Basin and the Anadyr Basin. The Navarin Basin is bounded at the ocean floor by the Anadyr Ridge in the northwest, the Okhotsk-Chukotsk belt to the southeast, and by the continental shelf in the southwest. The larger Bering basin is comprised of six basins including the Navarin, St. George, and Norton basins (Steffy 1991, Worrall 1991). The Navarin basin has been explored with

eight exploratory wells. The first of which (the ARCO Cost 1 well) was drilled in 1984 (Turner 1985).

Figure 2. A map showing the Navarin Basin in relation to the other basins in the Bering Sea (Steffy, 1991).

The depositional history of the Navarin Basin shows that around 45 Million years ago, in the Late Eocene Age, the Navarin basin sedimentary fill was interrupted by erosion and uplift. The interruption of the sedimentary fill by erosion is named the “Red Event” and all prior sedimentation is considered basement (Worrall 1991). The beginning of the

tectonic history of the Navarin Basin is marked by the red event (Worrall 1991). The red event begins with evidence of erosion in high areas, a period of no deposition, the development of an en echelon normal fault system. The pre-red event en echelon faults are called normal due to the high dip angle of sixty to seventy degrees (Worrall 1991).

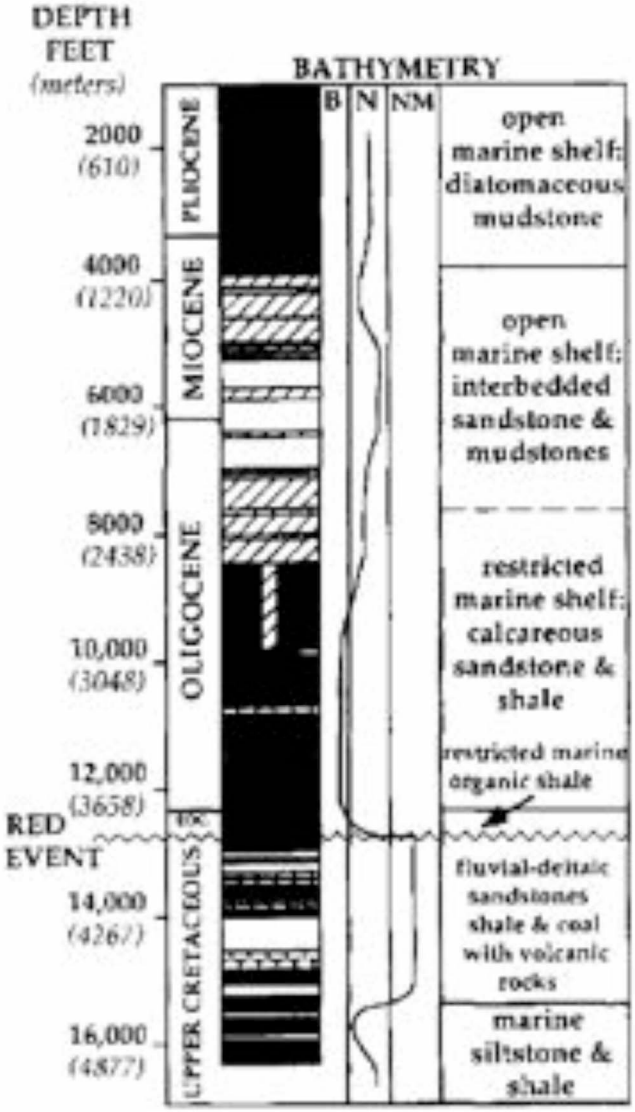

Figure 3. A general representation of the different lithologic division at depth of the COST 1 well (Worral, 1991).

Stratigraphy

Outcrops in Siberia provided the earliest geological exposure information about the stratigraphy of the Navarin Basin. Turner (1985) organized and described the stratigraphy of the Navarin Basin by examining biostratigraphy, lithostratigraphy, and seismic stratigraphy for the COST 1 drilling reports (Turner 1985). The biostratigraphy was comprised of paleontologic and paleoecologic analysis of the sediment of the COST 1 well. The age and depositional environment of the biostratigaphic separations are determined by analyzing microfossils containing marine species. Since the Red Event, three main events can be distinguished (Worrall 1991).

- Calcareous Sandstone and Shale from the late Eocene age to Oligocene age
- Interbedded Sandstone and Siltstone from the late Oligocene age to Miocene age
- Diatomaceous mudstone from the Pliocene age to present (Bour 1994). The organic shale layers from the Oligocene and Pliocene (Figure B) may contain millions of barrels of oil, but they may also contain regions of overpressure (Steffy 1991).

Turner (1985) separated the bio stratigraphic into the following divisions (Turner 1985):

1. Cretaceous interval (12,780 to 16,400 feet) determined by marine and non-marine fossils. The non-marine section (12,780 to 15,300 feet) is of Maastrichtian age and the marine section (15,300 to 16,400 feet) is Maastrichtian or Campanian age.

2. Eocene section from 12,280 feet to 12,780 feet determined by a lack of molluscs, ostracodes, or other micro fossils, and a depositional environment that transitions from upper bathyal to outer neritic.
3. The Oligocene strata from 5,704 to 12,280 feet indicated by abundant dinoflagellate assemblage in a middle neritic environment.
4. A Miocene section (3,180 to 5,704 feet) indicated by molluscan fossils and foraminiferal fauna in a middle neritic marine depositional environment.
5. The Pliocene section (1,536 to 3,180 feet) indicated by palynological and dinoflagellate fossil and a middle neritic marine depositional environment.

Turner (1985) also constructed a lithostratigraphy and seismic stratigraphy of the Navarin Basin by examining the well logs from the COST 1 well report with seismic reflection data (Figure 4). The lithostratigraphy and seismic stratigraphy is divided into eleven lithographic strata and five seismic sequences (Turner 1985).

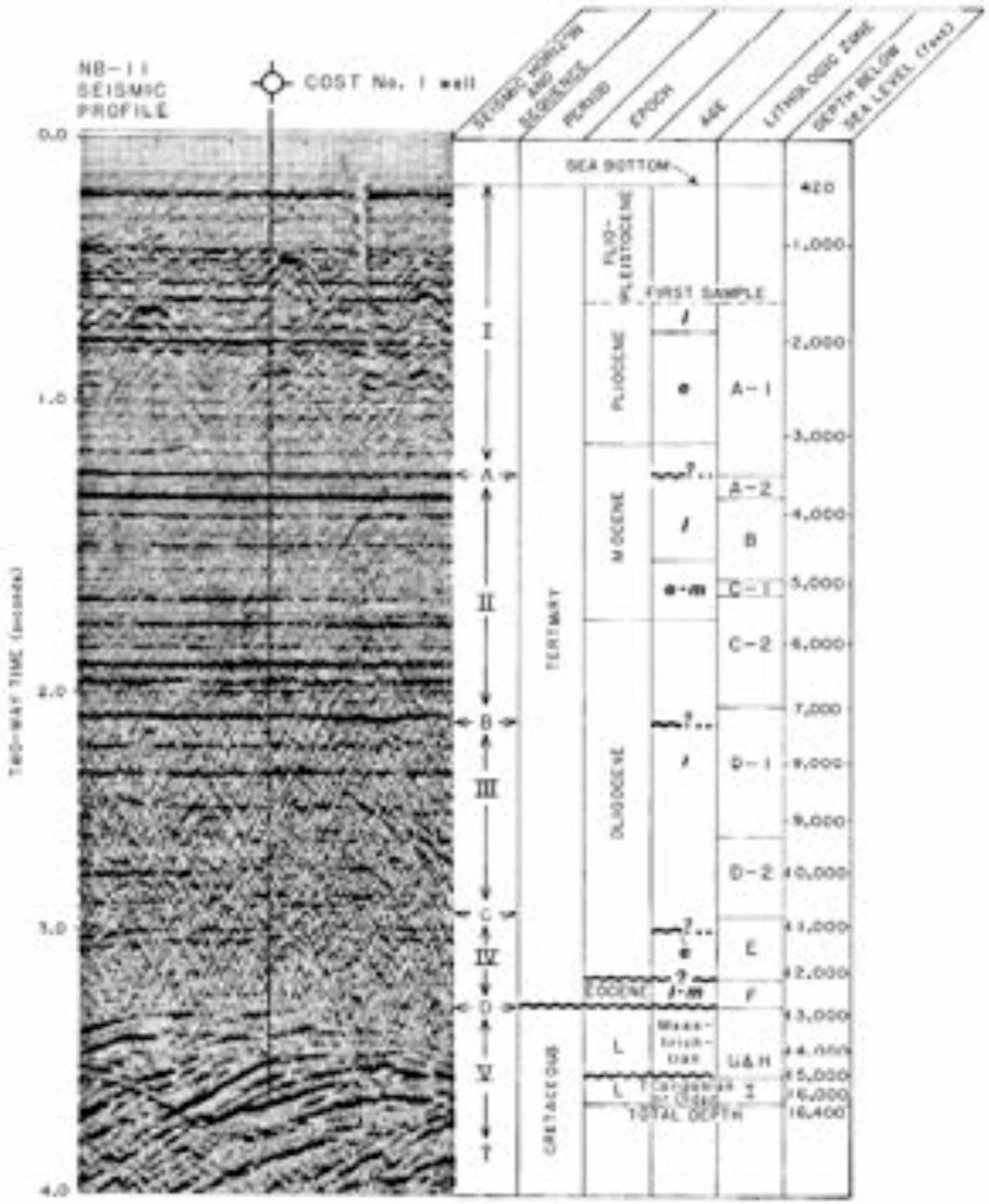

Figure 4. Divisions of the seismic stratigraphy (five sequences) and the lithologic stratigraphy (eleven zones) (Turner, 1985).

The lithostratigraphic zones are identified by Turner (1985):

1. The A-1 zone (Figure 4) from the depth of 420 to 3,500 feet consists of poorly sorted, silty, sandy mudstone from a mid-shelf depositional environment. Porosity and permeability have not been significantly altered by diagenetic processes including compaction and alteration (Turner 1985).
2. The A-2 zone (Figure 4) from a depth of 3,500 feet to 3,800 feet consists of the same poorly sorted silty and sandy mudstone from zone A-1 with increased diagenesis and cementation (Turner 1985).
3. The B zone (Figure 4) from a depth of 3,800 feet to 5,000 feet consists of bioturbated, muddy, fine-grained sandstone with interbedded sandy mudstone in a middle neritic depositional environment (Turner 1985).
4. The C-1 zone from a depth of 5,000 feet to 5,350 feet consists of fine-grained muddy sandstone and siltstone with thinly interbedded mudstone and claystone deposited in a middle neritic environment. The sandstone is cemented by calcite (Figure 4).
5. The C-2 zone from a depth of 5,350 feet to 7,000 feet consists of fine-grained muddy sandstone and siltstone interbedded with claystone and mudstone deposited in a middle to outer neritic environment. The sandstone is poorly sorted and cemented by calcite (Figure 4).
6. The D-1 zone (Figure 4) from a depth of 7,000 feet to 9,200 feet consists of sandy mudstone, claystone, and muddy sandstone deposited in an upper bathyal environment. Smectite clays are predominate (Turner 1985).
7. The D-2 zone from a depth of 9,200 feet to 10,900 feet consists of the same sandy mudstone and muddy sandstone as in zone D-1 deposited in an upper

bathyal environment (Figure 4). Illite clays predominate from diagenetically altered smectite clays (Turner 1985).

8. The E zone from a depth of 10,900 feet to 12,100 feet consists of poorly sorted gray claystone, mudstone, and sandy mudstone with abundant (40% to 70%) clay (Turner 1985).
9. The F zone from a depth of 12,100 feet to 12,900 feet consists of gray claystone and sandy mudstone with abundant organic content. There is micro fossil support for a neritic to middle bathyal depositional environment (Turner 1985).
10. The G and H zone from a depth of 12,900 feet to 15,000 feet consists of sandstone, coal, mudstone, and claystone deposited in a non-marine environment including stream or channel (Turner 1985).
11. The I zone from a depth of 15,000 feet to 16,400 feet consists of claystone, siltstone, mudstone deposited in a marine or marine shelf environment. 80% of the rock is clay, including smectite and illite (Turner 1985).

Seismic stratigraphy for the Navarin Basin was determined using seismic sequence analysis and seismic reflection data to identify five major seismic sequences separated by 4 seismic horizons or irregularities (Turner 1985), namely:

1. Horizon A at a depth of 3,500 feet consists of discontinuous large-amplitude seismic reflection denoting a late Miocene age angular unconformity (Figure 5) caused by intrusion of underlying shale diapirs.
2. Horizon B at a depth of 7,300 feet separates the large-amplitude reflections of seismic sequence 1 with the variable-amplitude reflections of seismic

sequence 2. Horizon B signifies a late Oligocene age angular unconformity (Figure 5) caused by a sea level reduction in the late Oligocene age.

3. Horizon C at a depth of 11,000 feet showed variable-amplitude reflection signifying an angular unconformity caused by a middle Oligocene age movement event in which older Tertiary and Mesozoic rocks subsided (Figure 5).
4. Horizon D at a depth of 12,900 feet separates the large-amplitude reflections of seismic sequence 4 with the variable-amplitude reflections of seismic sequence 5 (Figure 5) showing a late Cretaceous-Early Tertiary unconformity.

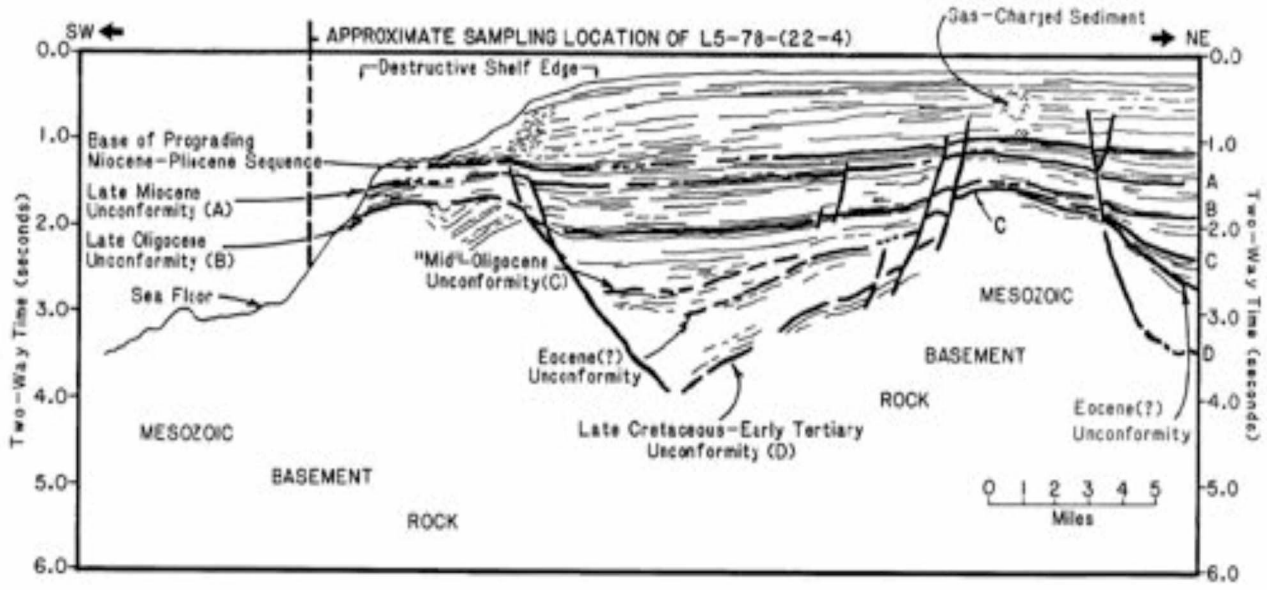

Figure 5. Several unconformities in the tectonic history of the Navarin Basin identified using seismic reflection technology (Worral, 1991).

Tectonic History

The Navarin Basin is part of the larger Bering Sea basin tectonic setting. The Bering Sea basin is bordered by the SE Bering fault to the south, and the NW Bering fault to the northwest (DeMets and Gordon 1990, Atwater and Stock 2010). The main stresses in this setting are the subduction interaction between the Pacific plate and the North American plate as evidenced by the large number of northwest striking faults in the southwest of the Bering basin (Xu, Zvi et al. 2014). Additional plate movement is strike slip displacement along the Aleutian trench and the Bering faults (Figure 6). Northeast striking faults exhibit domino style faulting and right strike slip movement in response to the movement of the pacific and north American plates (Xu, Zvi et al. 2014).

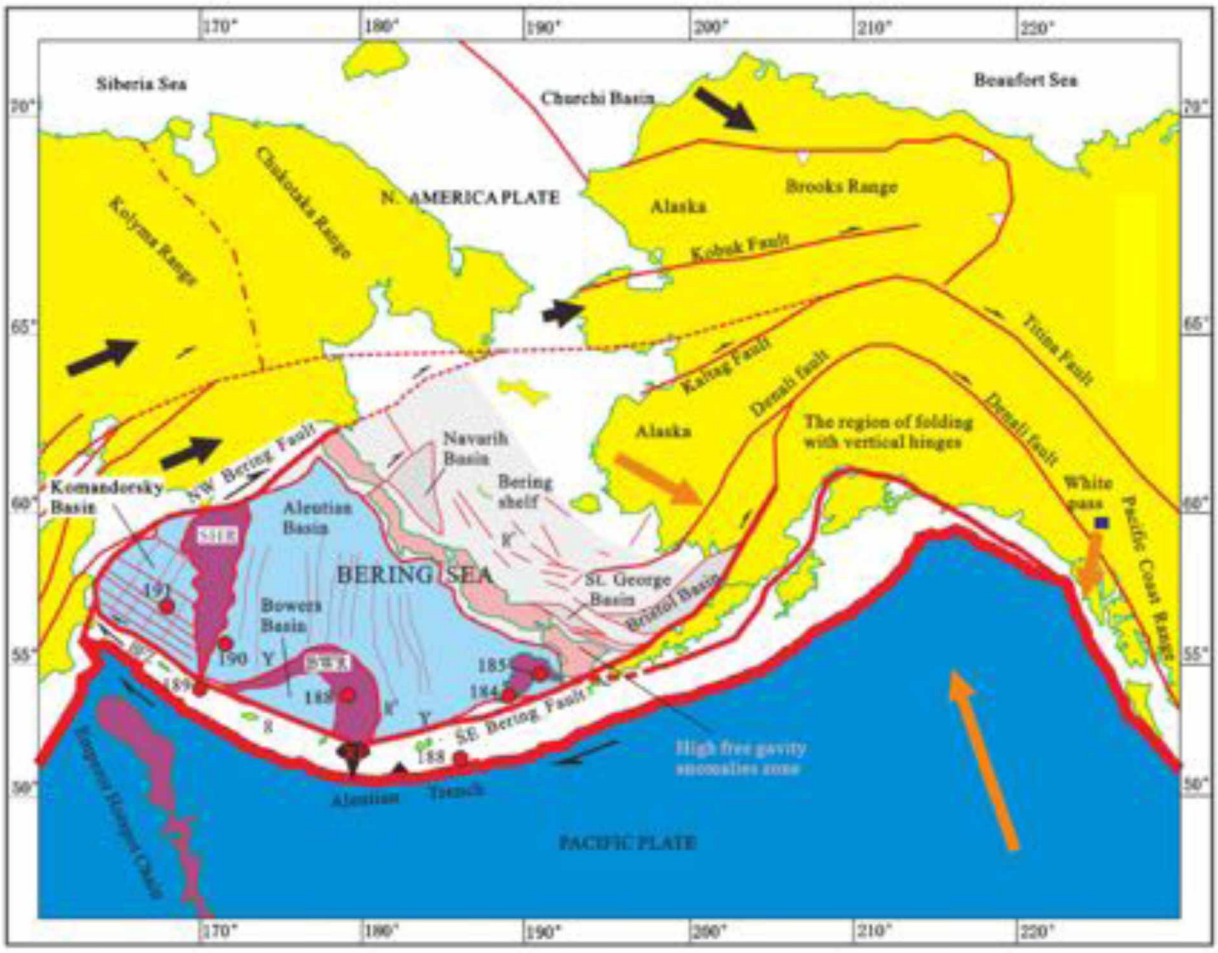

Figure 6. Stresses at the tectonic setting of the Bering sea including strike slip movement and subduction at the Pacific plate. (Xu, et al, 2014). Signs of these stresses are in the strike slip faults in the southwest and the Y faults in the south

The north basin, the deepest part of the Navarin Basin, is without faulting, and is bounded by wrench faults. On the red surface, the Navarin Basin is divided into north and south sub basins by a zone of linear faults on the central ridge, and the north basin is bounded by another series of linear faults. Except for wrench faults, there is a lack of measurable faulting in the Navarin Basin. Worral (1991) found that the tectonic history of Navarin Basin can be reasonable separated into four phases, namely:

1. A short period of en echelon folding and normal faulting in the middle Eocene age leading to the red event in the late Eocene age and an emerging wrench faulting system;
2. A period of marine deposition and basin subsidence from wrench fault deformation in the late Eocene age preceded the en echelon folds and extensile fractures gradually vanishing at different rates over the entire basin leading to almost complete basin subsidence in the late Pliocene age;
3. The third phase is marked by the end of wrench faulting and an inversion of the basin in the late Pliocene age.
4. The fourth phase is marked by active syncline folding throughout the central region of the Navarin Basin up to the present time.

Conclusion

The Navarin Basin is a sedimentary basin located to the west of Alaska in the Bering Sea. The depositional and tectonic history is marked from the Red Event: a period of rapid deposition and erosion in the Early Eocene age. The exploration of the Navarin Basin began with Russian interest in the 1960's when dozens of wells were drilled. Later in the 1980's the exploratory wells examined in this study were drilled by American companies. The Navarin Basin consists primarily of sedimentary lithology such as mudstone and sandstone. Regions of clay and coal are also present in the lithology which may contain petroleum. The Tectonic history is comprised of four main phases, the most recent is active syncline folding throughout the central region.

3. Origins of Overpressure in Sedimentary Basins

Introduction

Pore pressure is the load carried by the liquid inside the pore space of a rock. It is often referred to as hydrostatic pressure or the weight of a column of water as water is the predominant material in the pore space (Bruce and Bowers 2002). Pore pressure, together with vertical effective stress, gives the total overburden stress on a formation (Bruce and Bowers 2002, Figure 7).

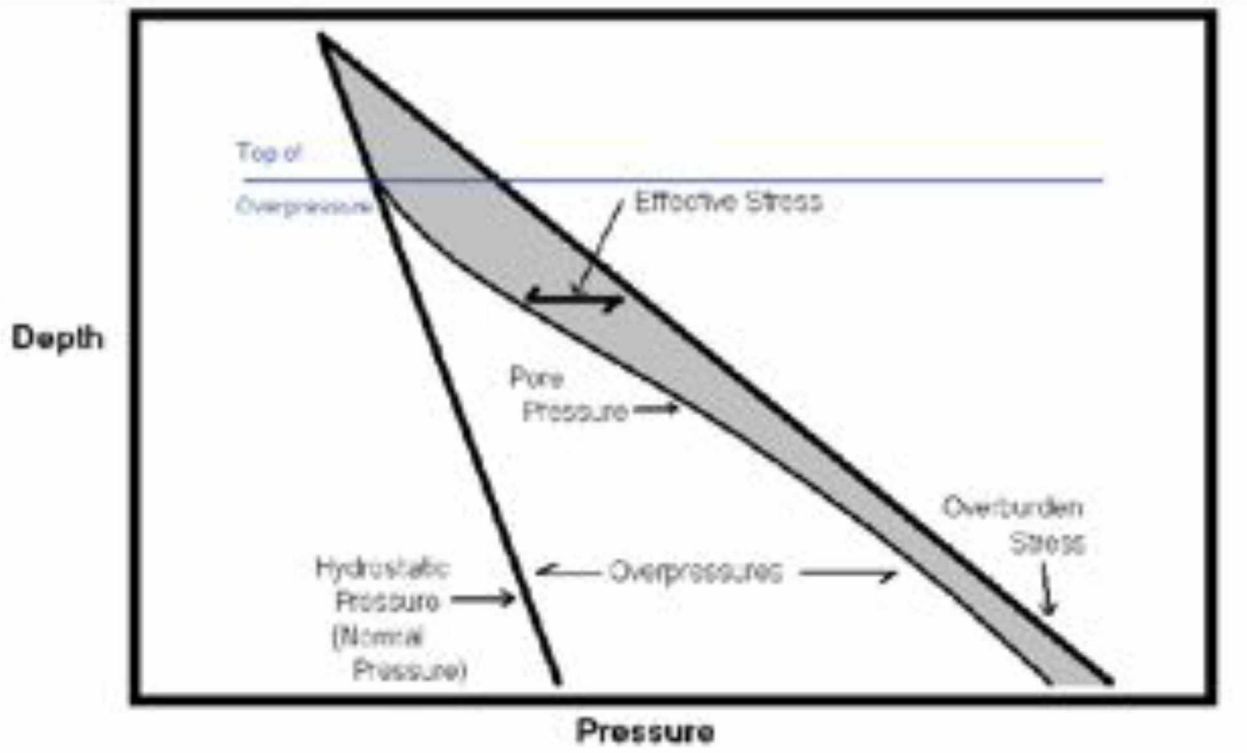

Figure 7. A representation of effective stress as the difference between overburden stress and pore pressure (Bruce and Bowers, 2002).

Pore pressure greater than hydrostatic pressure is termed as overpressure and can be as high as the overburden pressure (Griffin and Bazer 1969, Eaton 1972, Martinez, Schroeder et al. 1991, Elowe and Sherwood 2017).

Disequilibrium Compaction

As rock formations are deposited and buried, overlaying formations impose an overburden stress on the underlying formations (Eaton 1972). The stress loading causes a mechanical compaction where the porosity of the rock is decreased (Bowers 2002). Disequilibrium compaction is an imbalance between an increasing confining stress and the ability of the pore water to leave the formation (Barron, Weakley et al. 1990). A rapid increase in stress requires a rapid increase in fluid expulsion for pore pressure to remain hydrostatic (Chenevert and Sharma 1993). If the pore fluid can't be expelled as fast as the compaction increase, then the pore fluid must support some of the confining stress as overpressure develops (Osborne and Swarbrick 1999, Tingay, Hillis et al. 2009). The excess water in the pore space is identified by the lower density, since the density of water is less than the density of rock (Zhang and Wieseneck 2011). The difference in density between under compacted and normally compacted shale is the basis for the established methods of pore pressure prediction (Eaton 1972, Bour 1994, Bowers 2002, Zhang 2013). Disequilibrium compaction is known as the primary mechanism for overpressure generation in sedimentary basins (Osborne and Swarbrick 1999, Swarbrick 2002, Tingay, Hillis et al. 2009).

Terzahgi developed the relationship between the pore pressure, the weight carried by the rock matrix, and the total overburden stress, which is known as Terzaghi's equation:

$$VES = \sigma_v - P_p$$

Equation 1.

Where VES is the vertical effective stress, or stress carried by the rock matrix; σ_v is the overburden stress, or the entire vertical confining stress; and P_p is the pore pressure, or the stress carried by the material in the pore space (Terzaghi 1943). Compaction in sedimentary basins in Oklahoma was studied to show a negative exponential correlation between porosity and vertical effective stress where disequilibrium compaction had occurred (Athy 1930). Hart (1995) combined Terzaghi's equation with the exponential relationship between porosity and effective stress to predict subsurface pore pressures from porosity data (Hart 1995).

Fluid Expansion Mechanisms

Fluid expansion differs from disequilibrium compaction in that the volume of pore fluid is changing in fluid expansion, whereas in disequilibrium compaction, the volume of the pore space is changing (Mouchet and Mitchell 1989, Neuzil 1995, Tingay, Hillis et al. 2009). Compaction of sedimentary rocks is known as an irreversible process (Magara 1980). Therefore, any additional fluid introduced into the pore space will increase the pore pressure (Mouchet and Mitchell 1989, Osborne and Swarbrick 1997). Fluid expansion can cause an increase in pore pressure through increasing the specific pore volume. Fluid expansion mechanisms can also contribute to overpressure attributed to disequilibrium compaction in deep formations (Mouchet and Mitchell 1989, Osborne and Swarbrick 1997, Figure 8). The increased pore pressure can outpace any increase in overburden pressure and therefore decrease the vertical effective stress (Miller 2002). Different mechanisms of fluid expansion include hydrocarbon generation, clay

diagenesis, vertical transfer, thermal expansion, and coal dewatering (Mouchet and Mitchell 1989, Neuzil 1995, Osborne and Swarbrick 1997, Tingay, Hillis et al. 2009).

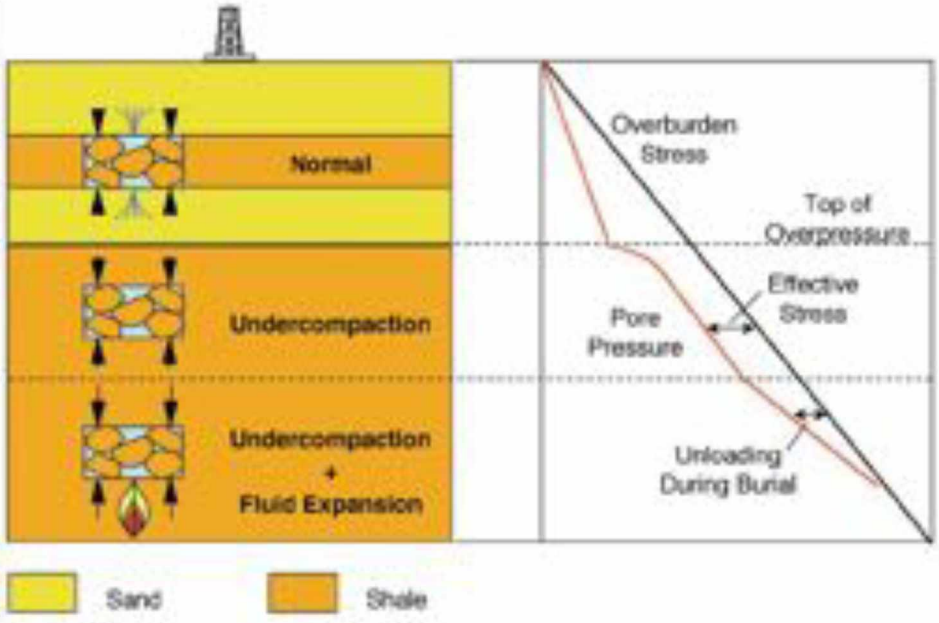

Figure 8. (Bowers, 2002) Fluid expansion can contribute to overpressure attributed to disequilibrium compaction.

Hydrocarbon Migration

Although all fluid expansion mechanism have the ability to increase pore pressure to a point of overpressure, only hydrocarbon migration is considered capable of producing severe amount of overpressure to rival disequilibrium compaction (Osborne and Swarbrick 1997, Tingay, Hillis et al. 2009). Hydrocarbon generation was determined as the leading cause of overpressure in the Rocky Mountain basins (Spencer 1987). When calculated in an extemely isolated system, where pressure could be trapped in the pore space, the over pressure generated from kerogen maturation approached the overburden pressure (Miller 2002). A study of overpressure in the Piceance Basin,

Colorado measured the pore pressure generated by gas from hydrocarbon maturation. These pore-fluid pressures measured as high as near overburden stress (Fall, Eichhubl et al. 2012).

Hydrocarbon maturation causes increased pore pressure when hydrocarbon material (originally a component of the bulk density or rock component) matures and becomes part of the pore volume (Osborne and Swarbrick 1997). This kerogen maturation not only causes a reduction in vertical effective stress, but a decrease in bulk density and an increase in porosity of the target formation (Osborne and Swarbrick 1997, Tingay, Hillis et al. 2009). Kerogen maturation also can contribute to overpressure originally attributed to under compation (Chilingar 2002). The kerogen maturation process can also exacerbate overpressure from undercompaction when the fluid from kerogen maturation alters the composition of the pore fluid (introduces more solutes) and decreases the permeability of the target formation and impedes the escape of excess pore fluid (Chilingar 2002).

Clay diagenesis

The process of dehydration during clay diagenesis can contribute to overpressure by releasing water into the pore volume (Hower, Eslinger et al. 1976, Velde and Vasseur 1992, Lahann 2001, Luo, Wang et al. 2007). Specifically, Smectite transforms into Illite with water as a byproduct (Luo, Wang et al. 2007). The additional water in the confined pore space increases pressure as with other fluid expansion mechanisms (Lahann 2001). The water released by diagenesis also may have a different density and composition than the original pore fluid (Hower, Eslinger et al. 1976). The changing chemistry of the pore fluid may affect the permeability of the host rock to alter or inhibit

the expulsion of water during compaction (Bethke 1986). During rapid burial rates when disequilibrium compaction is the main origin of overpressure, a period of clay diagenesis could further inhibit the balance of pore fluid pressure and contribute to the overpressure (Bethke 1986).

Load transfer

Overpressure has been discovered in unexpected areas when the overpressure laterally or vertically transfers to another area. The rate of transfer depends on the permeability of the surrounding formations (Tingay 2007). Overpressure can transfer to another formation along interconnected pores until it is trapped in a lower permeability area or some hydrostatic equilibrium is achieved (Burley, Mullis et al. 1989). Faults and other tectonic deformations can contribute to conditions permissible to overpressure load transfer (Swarbrick and Osborne 1998). Overpressure originating from the vertical or horizontal transfer of some initiating overpressure is classified as fluid expansion overpressure due to the lack of observable porosity changes differentiating normal pressure and overpressure (Fertl and Chilingar 1977, Traugott 1997).

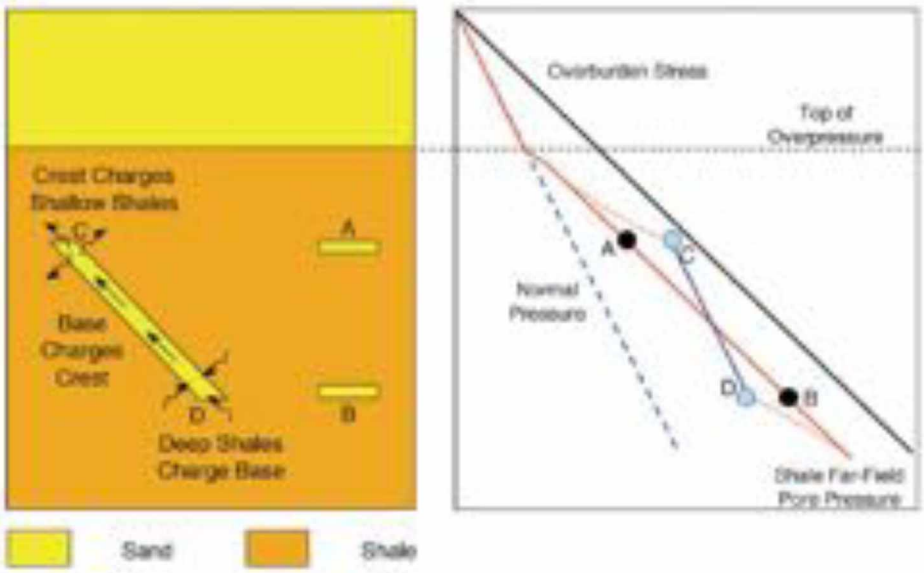

Figure 9. (Bowers, 2002) Example of overpressure from deep shales transferred to shallow shales.

Aquathermal expansion

Aquathermal expansion involves the heating of pore fluid in a sealed, isolated formation so that the pore fluid expands and creates a zone of overpressure when compared to surrounding formations (Barker 1972, Chapman 1980, Bethke 1986, Luo and Vasseur 1992). Certain isolated zones of low permeability were shown to develop different geothermal gradients than surrounding formations (Barker 1972). When the geothermal gradient differed by more than fifteen degrees Celsius per kilometer, then the isolated zone would be under or overpressured in comparison to surrounding formations (Barker 1972). The degree of isolation needed to sustain aquathermal expansion can be found in the most low permeability shale (Chapman 1980). Constructed models controlling for overpressure parameters such as compaction rates, geothermal gradient, and impermeability showed that even with ideal conditions for aquathermal expansion the

contribution to overpressure was likely minimal. Other fluid expansion mechanisms like hydrocarbon maturation and clay diagenesis were more likely to contribute to overpressure to a greater magnitude (Bethke 1986, Luo and Vasseur 1992).

Coal Dewatering

During coalification a large amount of water is released from coal (Law, Hatch et al. 1983). This water may add to the water in the pore space and therefore contribute to overpressure via fluid expansion. As with other fluid expansion mechanisms, coal dewatering depends on the isolation of the coal-bearing formation, the permeability of the target formation, and the lithology and stratigraphy of the target formation (Law, Hatch et al. 1983). There is not very much investigation on the degree of overpressure possible from coal dewatering or where it has been observed. Further study should be undertaken to develop a more complete understanding of fluid expansion overpressure from coal dewatering.

Conclusion

Overpressure is the term for pore pressure that exceeds normal hydrostatic pressure up to pressure as high as overburden pressure (Griffin and Bazer 1969, Eaton 1972, Martinez, Schroeder et al. 1991, Elowe and Sherwood 2017). Different causes of overpressure are described as origins of overpressure, and include the main categories of disequilibrium compaction and fluid expansion. Disequilibrium compaction occurs when the rapid burial of overlying formations exceeds the ability of the pore fluid to escape the rock matrix in deeper formations. The trapped pore fluid causes an increase in pressure as the pore space is decreased. Fluid expansion overpressure occurs when

there is a change to the pore fluid composition or volume that increases the pressure inside the pore space. Specific fluid expansion mechanisms include hydrocarbon migration, clay diagenesis, load transfer, aquathermal expansion, and coal dewatering. The following chapter will attempt to identify the origin of overpressure in the Navarin Basin.

4. Overpressures in the Navarin Basin

Introduction

To better determine the origin of overpressure in the Navarin Basin, the entire basin is examined as a unit. The pore pressure measurements taken from the mud log information is mapped for the entire basin to look for patterns or characteristics of overpressure. This pore pressure mapping is done at several depths to create an overall understanding of pressure regime in the Navarin Basin. Burial rate and compaction information is determined from stratigraphic and lithographic logs and combined with geologic ages. The Burial rate is then characterized over the entire basin to help determine an origin of overpressure. Tectonic information is revisited and characterized to include or rule out the possibility of overpressure generation from tectonic origins in this basin.

Pore Pressure Distribution

Mud log information is used to obtain pore pressure measurements at different depths of the exploratory wells. Matlab® was then used to show the change in pore pressure over the area of the basin. Figures 10, 11, and 12 show the pore pressure gradients over the Navarin Basin at depths of 4000, 6000, and 8000 feet, respectively. These depths were chosen as they represent the range of available well log data shared over the entire basin although some individual wells may contain a greater range of information.

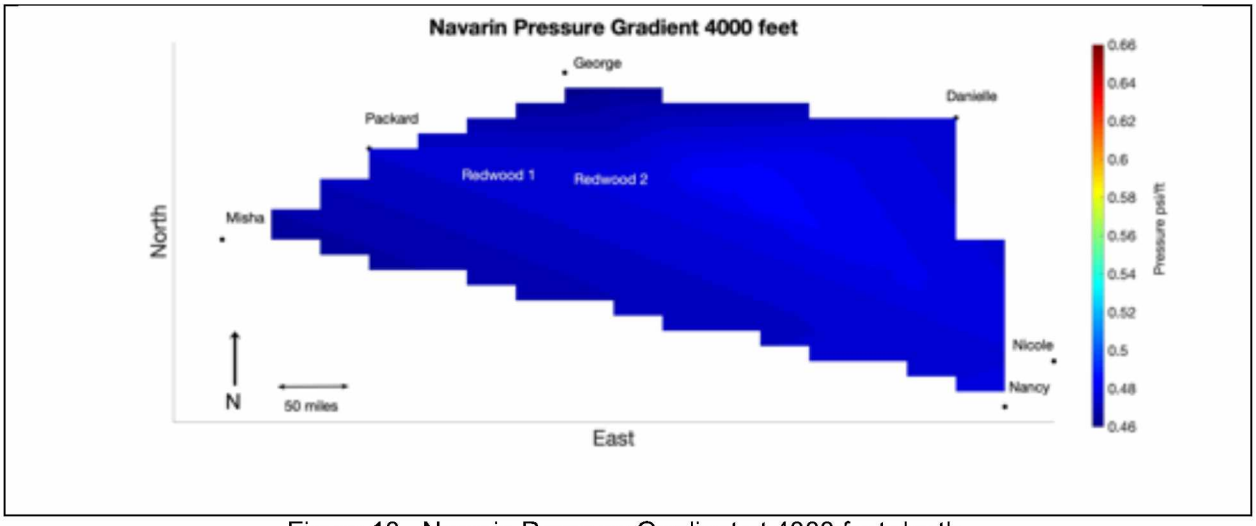

Figure 10. Navarin Pressure Gradient at 4000 feet depth.

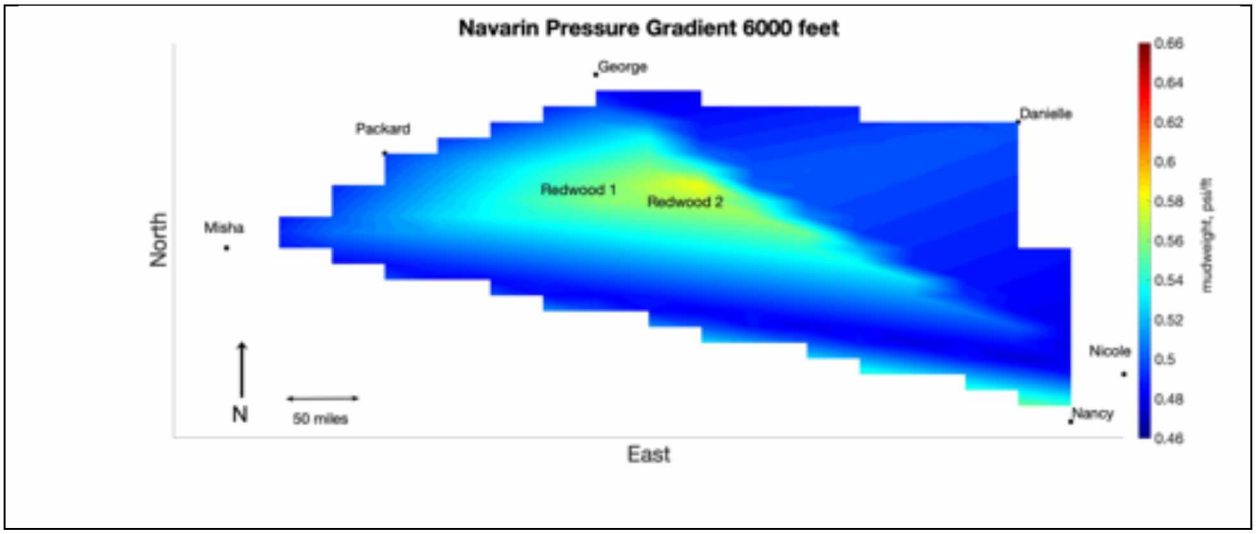

Figure 11. Navarin Pressure Gradient at 6000 feet depth.

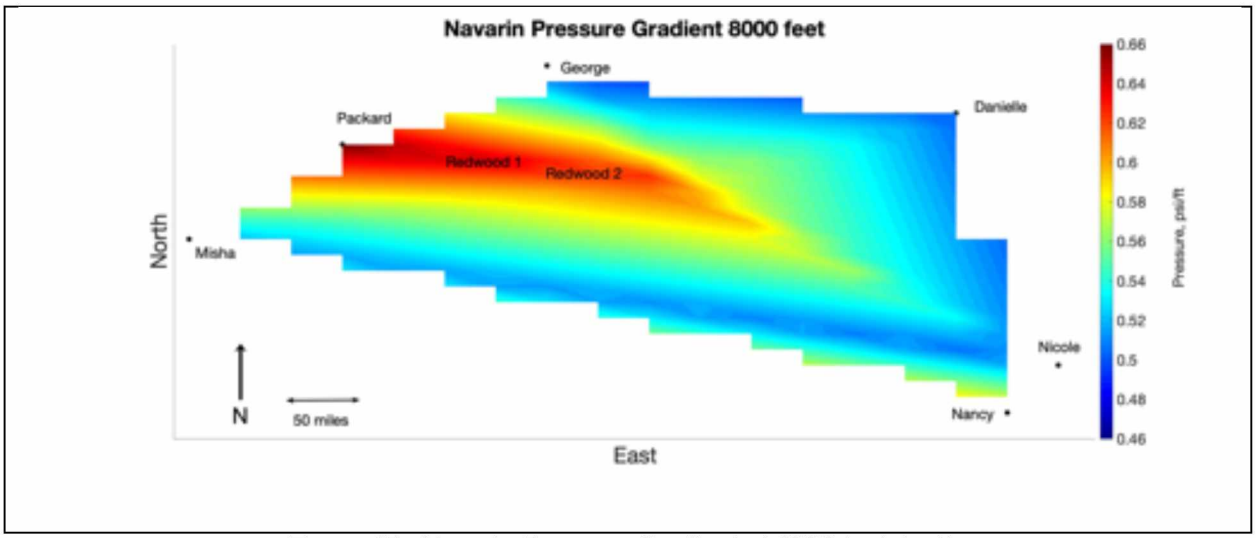

Figure 12. Navarin Pressure Gradient at 8000 feet depth.

The pore pressure gradient information at general depths gives an overall idea especially in Figure 12 that the central portion of the basin contains a greater pore pressure gradient than the surrounding wells. This area includes the individual wells Packard, Redwood 1, and Redwood 2 which lie consecutively from the west to center of the basin. To further develop this central pressure trend, a target formation is identified by examining lithographic and stratigraphic data from the Navarin Basin exploratory wells. The severe overpressure is observed around 8000 feet deep in the Redwood 1 and Redwood 2 wells. This depth corresponds to the mostly shale Eocene formation seen at this depth in these wells. Figure 13 shows an example of stratigraphic data constructed to help identify the correct target formation from well Redwood 1. Lithology and depositional environment information was compiled from drilling data obtained from the BOEM.

General Stratigraphy, Lithology, and Depositional Environment for Well 599 (Redwood 1)			
Interval (feet)	Age	Lithology	Environment
880-1360	Pleistocene age	Mudstone	Middle to outer neritic
1360-2470	Pliocene age	Sandy mudstone	Middle to outer neritic
2470-4720	Miocene age	Sandy mudstone	Middle to outer neritic
4720-5650	Oligocene age	Sandy mudstone	Outer neritic
5650-9100	Eocene age	Shale	Outer neritic
9100-11000	Indeterminate age	Sandy mudstone/Shale	Non marine
11000-11536	Late Cretaceous age	Sandy mudstone/Shale	Marine

Figure 13. Redwood 1 Target Formation stratigraphy (Core Laboratories 1987).

Wells Redwood 1, Redwood 2, and Packard share the same lithology and stratigraphy at around 8000 feet depth where the overpressure was observed. This Eocene age shale formation is then identified as the target formation. Further characterization of the target formation is completed by mapping the pore pressures measured at 10 feet within the Eocene age target formation. Figure 14 shows the same general trend of high pressure within the central portion of the Navarin Basin.

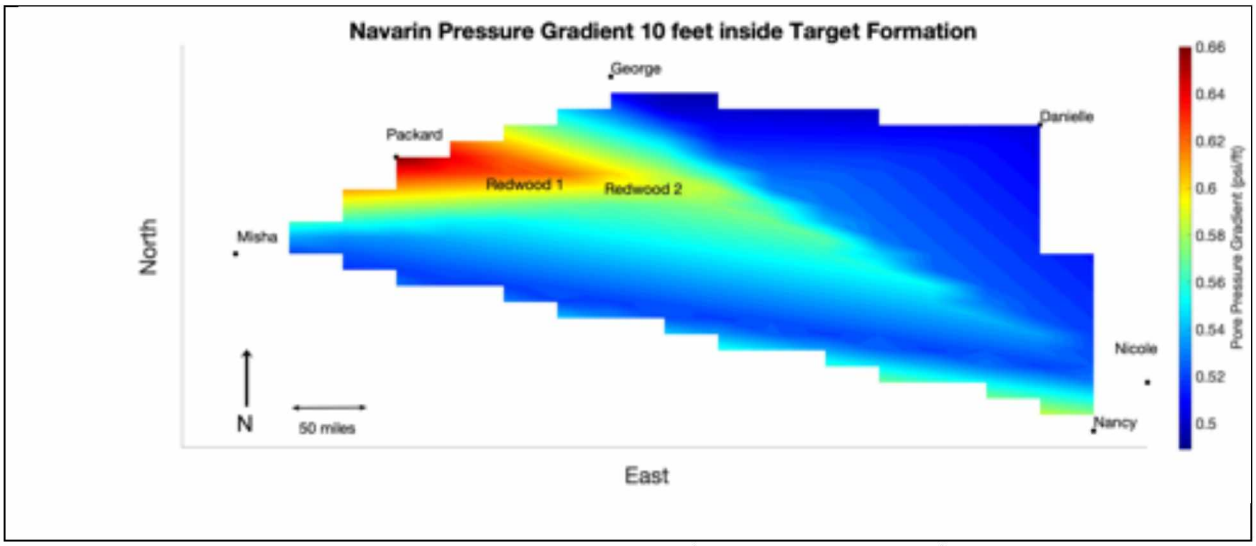

Figure 14. Pore pressure gradient at 10 feet inside the target formation

Another characterization of the pressure is made by mapping the depth to the target formation over the entire basin. Figure 15 shows a general trend that the target formation is deeper in the center of the formation, although at more of a northeastern position than the observed overpressure. This is somewhat misleading as the thickness of the target formation is greater in the center even though the target formation begins at a shallower depth.

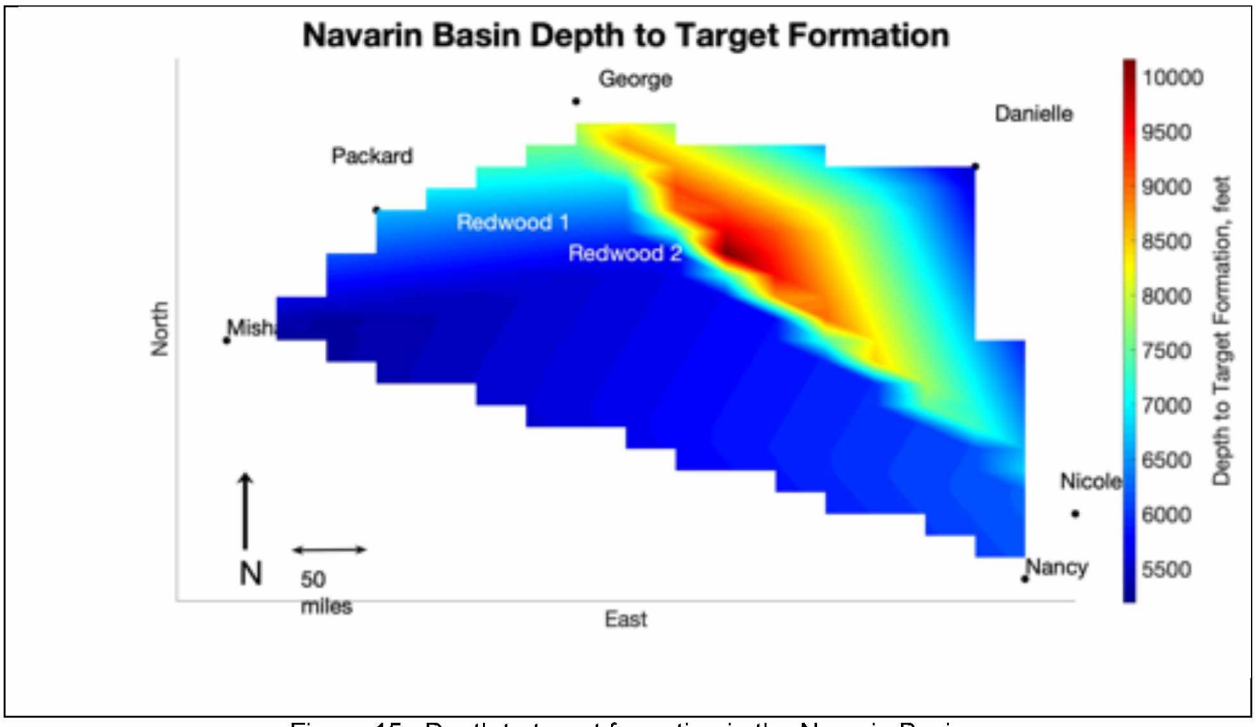

Figure 15. Depth to target formation in the Navarin Basin

Burial Rate

The previous pressure gradient maps provide one method to characterize the overpressure origins in the Navarin Basin. Another aspect of compaction that can help characterize the overpressure origins is the burial rate or compaction rate. Any clear evidence of rapid burial suggests disequilibrium compaction overpressure generation as

a rapid burial would prevent the escape of pore fluid. To determine the depositional rate, the stratigraphic divisions are determined for each well from lithographic and stratigraphic log information. Then the ages of the formations are determined from the same stratigraphic logs and combined with the formation thickness to get a depositional rate of how many feet were deposited every million years. Table 1 shows the calculated depositional rates for the formations of the Redwood 1 well.

Lithology and Depositional Rate for Well 599 (Redwood)				
top of formation (ft)	thickness (ft)	age (Ma)	deposition age interval (Ma)	deposition rate (ft/Ma)
880	480	0	2	268
1360	1110	2	3	347
2470	2250	5	19	118
4720	930	24	10	93
5650	3450	34	21	164
9100	1900	55	N/A	N/A
11000	536	65	34	16
11536	N/A	99	N/A	N/A

Table 1. Depositional rate for formation in the Redwood 1 well.

From the table it is shown that the deposition rate of the target formation was much less that the overlying formations. Some of the overlying formations were deposited over 20 times more quickly than the target formation. This same trend was observed in the other wells of the Navarin Basin, especially Redwood 2 and Packard. This compaction

rate trend suggests an overpressure mechanism of disequilibrium compaction since the rapid burial rate would prevent pore fluid from escaping the pore space and overpressure would occur.

Overpressure Pertaining to Tectonics

The Tectonic aspects of the Navarin Basin are revisited with the knowledge of the overpressure trend in the center of the Basin. After examining the overpressured horizons of this area, the relevant tectonic characteristic was identified as an active syncline folding trend almost exactly where the overpressure was measured. This syncline folding further supports the origin of overpressure as disequilibrium compaction as syncline folding may aid and accelerate the burial process. A syncline fold usually is deeper in the center and the target formation is of greater thickness in the center of the basin. As a syncline fold forms, more deposits accumulate at the center of the fold and it becomes thicker and deeper than the outside edges.

Conclusion

The pore pressure for the Navarin Basin was mapped at several depths to create an overall pressure description of the pressure over the entire basin. This pressure mapping showed overpressure in the central region of the basin at a depth around 8,000 feet. After identifying the overpressure general depth, an inspection of the stratigraphy and lithology showed a shale formation from the Eocene age at this depth among the wells. Burial rate and compaction information were then calculated from stratigraphic and lithographic logs and the geologic ages of the target formations. The Burial rate showed a trend of higher rates in the young, overlying formations and lower

rates in the older, deeper formations. This rapid burial of overlying formations suggests the overpressure origin as disequilibrium compaction, since a rapid burial rate is a main characteristic of under compaction.

5. Examining Origin of Overpressure in the Navarin Basin

Introduction

Vertical Effective Stress Plots

A common method for distinguishing disequilibrium compaction from fluid expansion mechanisms is by studying plots of vertical effective stress against sonic velocity (Pennebaker 1968, Magara 1980, Bowers 1994, Serebryakov, Chilingar et al. 1995, van Ruth, Hillis et al. 2004, Tingay 2013). For formations undergoing disequilibrium compaction, the porosity will decrease with depth in response to vertical overburden stress (Tingay, Hillis et al. 2009). Sonic velocity data is easily obtained so it can serve as a proxy to often inaccurate data (Pennebaker 1968). Normal mechanical loading behavior in the target formation is represented by a positive correlation with increasing sonic velocity and increasing vertical effective stress (Tingay 2013). In the case of disequilibrium compaction, vertical effective stress decreases while sonic velocity increase with a lower rate than normal compaction. Therefore, when vertical effective stress is plotted against sonic velocity, any formations experiencing disequilibrium compaction will be observed as a roll back on the normal compaction trend or loading curve (van Ruth, Hillis et al. 2004, Figure 16).

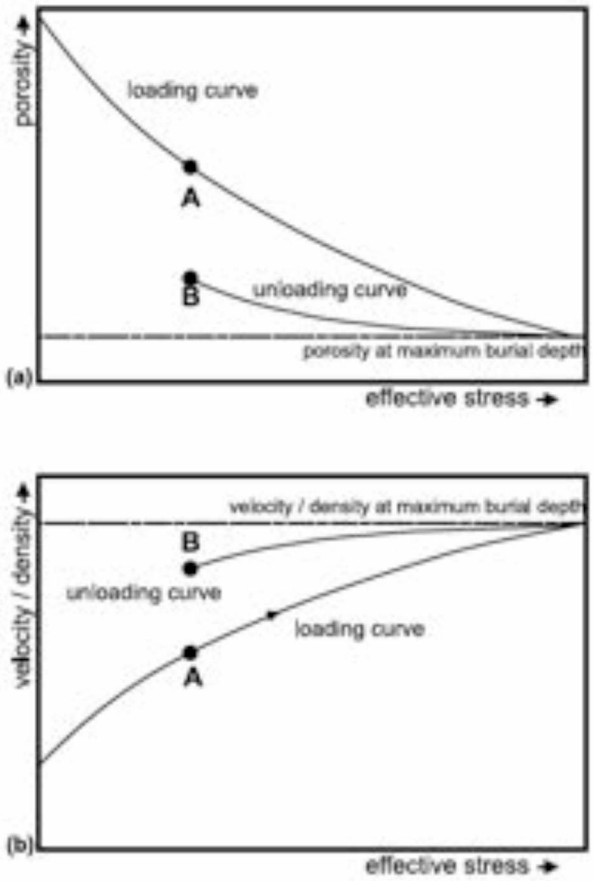

Figure 16. Examples of velocity and porosity vs. effective stress for loading and unloading curves (van Ruth, 2004).

However, liquid expansion mechanisms will not follow the normal loading curve; they will follow a new unloading curve on the vertical effective stress vs. sonic velocity plot (van Ruth, Hillis et al. 2004, Figure 16). Since compaction is an irreversible process, fluid expansion mechanisms are not evident through porosity changes, so the sonic velocity will not significantly change in the vertical effective stress vs. sonic velocity plot (Tingay, Hillis et al. 2009). Additionally, the fluid expansion mechanisms may not match the pace of the normal overburden loading rate, so the vertical effective stress may decrease when the pore pressure increases more quickly than the overburden pressure (Pennebaker 1968, Magara 1980, Bowers 2001, Tingay 2013). Therefore, the origin of

overpressure in the Navarin Basin can be partially characterized by plotting the vertical effective stress against the sonic velocity (Figure 17). Figure 17 shows this relationship between vertical effective stress and sonic velocity as a formation is compacted. As discussed previously, this will ideally help to distinguish disequilibrium compaction from fluid expansion mechanisms, or to determine if there are any signs of additional overpressure generation mechanisms in addition to the more common disequilibrium compaction.

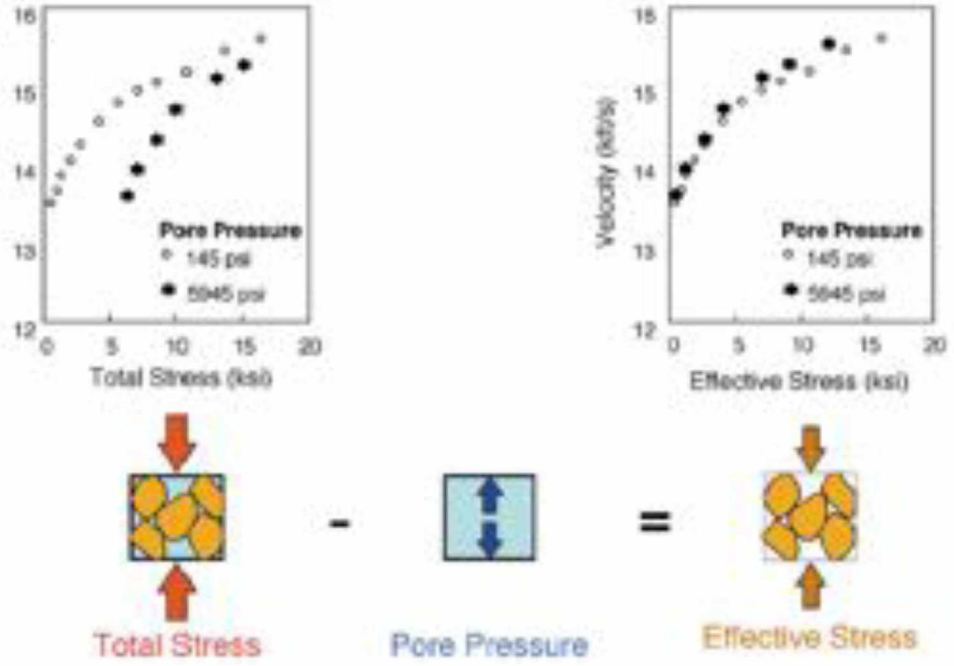

Figure 17. Examples of effective stress and total stress plots for overpressured formations. The sonic velocity and vertical effective stress increase as the formation is buried. Under increasing effective stress, the sediments compact and their sonic velocity approaches limits set by the grain properties. The effective stress and sonic velocity increase similarly under different pore pressures. The total stress and and sonic velocity increase at similar trends, but at different intervals with increasing pore presures (Bowers, 2001).

Bulk Density Velocity Crossplots

In addition to vertical effective stress – velocity plots, crossplots of density against velocity can give information about the origins of overpressure (Lahann 2001, Katahara 2006). During compaction, transport properties such as sonic velocity experience more elastic deformation than bulk properties (density, porosity) which are more inelastic under compaction. Elastic deformation is reversible, so a sonic velocity reversal with a change in density would suggest an elastic change or unloading during compaction (Bowers 2001). Crossplots of density against velocity can give additional density information not readily available from a vertical effective stress – velocity plot (Katahara 2003, Katahara 2006, Tingay 2013). As shown in Figure 18, different fluid expansion mechanisms may be differentiated by density and velocity/porosity response on the crossplots (Lahann 2001, Bowers 2002, Tingay 2013).

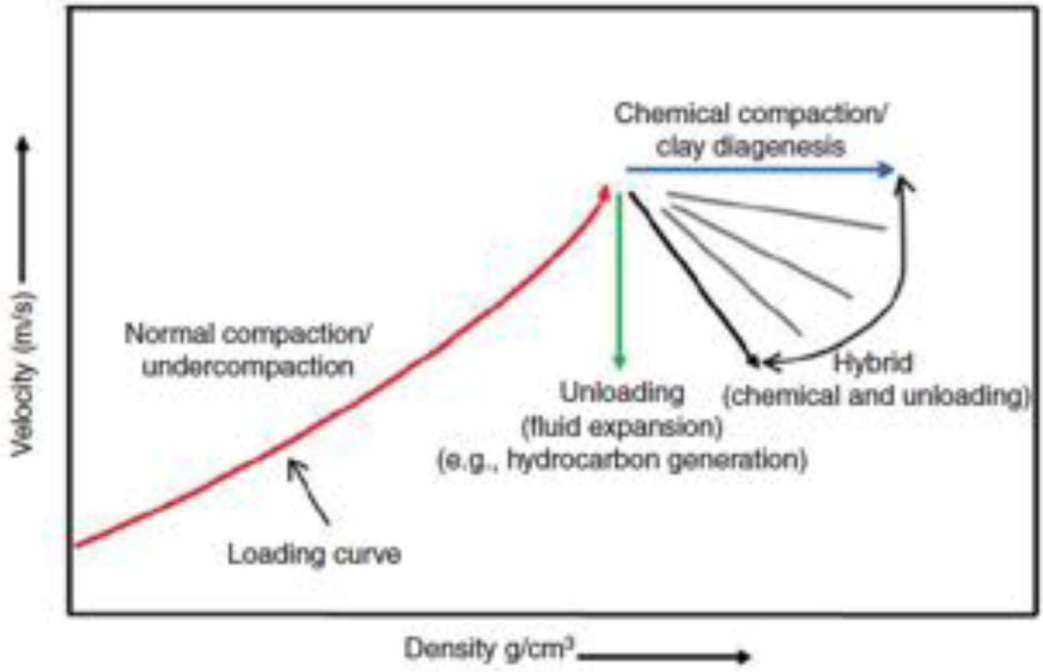

Figure 18. Density velocity crossplots can distinguish different overpressure mechanisms (Satti et al, 2015).

As with vertical effective stress – velocity plots, density velocity crossplots exhibit a loading curve for sediments undergoing normal compaction (Hoesni 2004). This is explained by density and porosity increasing under normal mechanical compaction: as overburden stress increases with burial, rocks become compacted by losing the pore space. As a result, the density will increase and the porosity will decrease (Katahara 2003, Hoesni 2004). Disequilibrium compacted sediments will remain on the loading curve because overpressure from undercompaction slows or resists the changes in porosity and density from compaction while still maintaining the correlation between them (Katahara 2003, Katahara 2006). Fluid expansion overpressure alternatively shows deviation from the loading curve on density velocity crossplots (Satti, Ghosh et al. 2015). Fluid expansion mechanisms are not as related to mechanical compaction as

the disequilibrium compaction mechanism (Hoesni 2004). Instead, additional pore fluid is introduced into a confined, sealed pore space, which is visualized by a decrease in velocity (an increase in porosity) and a small decrease in density on the density velocity crossplot (Bowers 2002, Katahara 2003).

A novel benefit of crossplot analysis is the additional ability to distinguish between kerogen maturation/fluid expansion mechanisms and clay diagenesis/chemical compaction mechanisms (Goulty and Ramdhan 2011, Satti, Ghosh et al. 2015). Clay diagenesis shows an increased density in the target formation, which shows a deviation to the right of the loading curve on a density velocity crossplot (Hoesni 2004). Alternatively, kerogen maturation and fluid expansion exhibit a decreased density in the target formation; therefore, the deviation from the loading curve shows a downward path on the density velocity crossplot (Goulty and Ramdhan 2011, Satti, Ghosh et al. 2015). Any combination of fluid expansion and chemical compaction would exhibit a downward, right deviation from the loading curve (Katahara 2003, Hoesni 2004, Katahara 2006).

Methodology

The methods utilized for the ultimate goal of constructing and interpreting vertical effective stress vs. sonic velocity plots include:

1. Obtaining well log data
2. Discriminating shale formations
3. Calculating Overburden pressure
4. Constructing plots for each well

Obtaining Well Log Data

Well log information was obtained by contacting the Alaska Bureau of Ocean Energy Management (BOEM) and requesting the well logs for the eight exploratory wells in the Navarin Basin (Figure 19).

Table 1. COST and exploratory well characteristics.

Well Name and Operator	Location (degs.) N. Lat.	Location (degs.) W. Long.	Water Depth (feet) Below Mean Sea Level	Total Depth (feet) Below Kb	Kb Elev. (feet) Above Sea Level	Corrected Geothermal Gradient (°F/100 feet)
ARCO COST No. 1	60.18	176.27	432	16,400	85	1.78
AMOCO George No. 1	60.85	177.93	480	9,085	86	1.76*
ARCO Packard No. 1	60.37	178.27	541	13,741	86	1.36
EXXON Redwood No. 1	60.33	177.25	483	11,536	86	2.05
EXXON Redwood No. 2	60.40	177.12	481	11,570	86	2.05**
AMOCO Nancy No. 1	59.28	175.42	452	8,708	86	2.14
AMOCO Misha No. 1	59.82	178.48	473	7,962	86	1.25
AMOCO Danielle No. 1	60.78	176.48	393	10,045	86	2.24
AMOCO Nicole No. 1	59.58	175.42	443	11,030	85	2.15

*Estimated from geothermal map.
**Estimated from Redwood No. 1 well.

Figure 19. Navarin Basin exploratory well characteristics

The well logs were digitized using computer to obtain data for caliper, density, resistivity, sonic velocity, and gamma ray. Scanned copies of well logs from the eight exploratory Navarin Basin wells were obtained through contacting the BOEM. Each scanned well log was imported to a photo editing software and trimmed to portions

manageable for web digitizing applications. For example, bulk density logs were split into portions of one thousand feet depths and the bulk density measurement was recorded at 3 to 5 foot intervals. The data was then compiled in Microsoft Excel and indexed to provide bulk density data for the entire well depth. These steps were repeated for resistivity, sonic velocity, and gamma ray well logs.

Shale discrimination scheme

In most analysis, evaluations yield better results if performed on one rock type. In the case of overpressure origin identification, it's important to remove the impact of lithology from the data. Therefore, since shales undergo mechanical compaction, shale (or shale-rich) strata were selected as a mechanical representative of the surrounding formations. In order to utilize crossplots to help identify possible zones of overpressure, the regions of interest need to be narrowed to those containing shale (Chenevert and Sharma 1993). Shale regions are identified using gamma ray data where a V_{shale} value is greater than 0.8 (Gardner, Gardner et al. 1974). V_{shale} is calculated using Equation 2.

$$V_{sh} = I_{GR} = \frac{GR_{\log} - GR_{\min}}{GR_{\max} - GR_{\min}}$$

Equation 2.

Figure 20 shows the gamma ray data with depth for well 560 George. Equation 2 is used to calculate the V_{shale} for each formation according to the stratigraphy and lithology of the well from available geology reports. Every formation has a different minimum and

maximum gamma ray value used to calculate the V_{shale}. After V_{shale} has been calculated for every depth of the well, the data is sorted so that V_{shale} values greater than 80% are organized as shale formations.

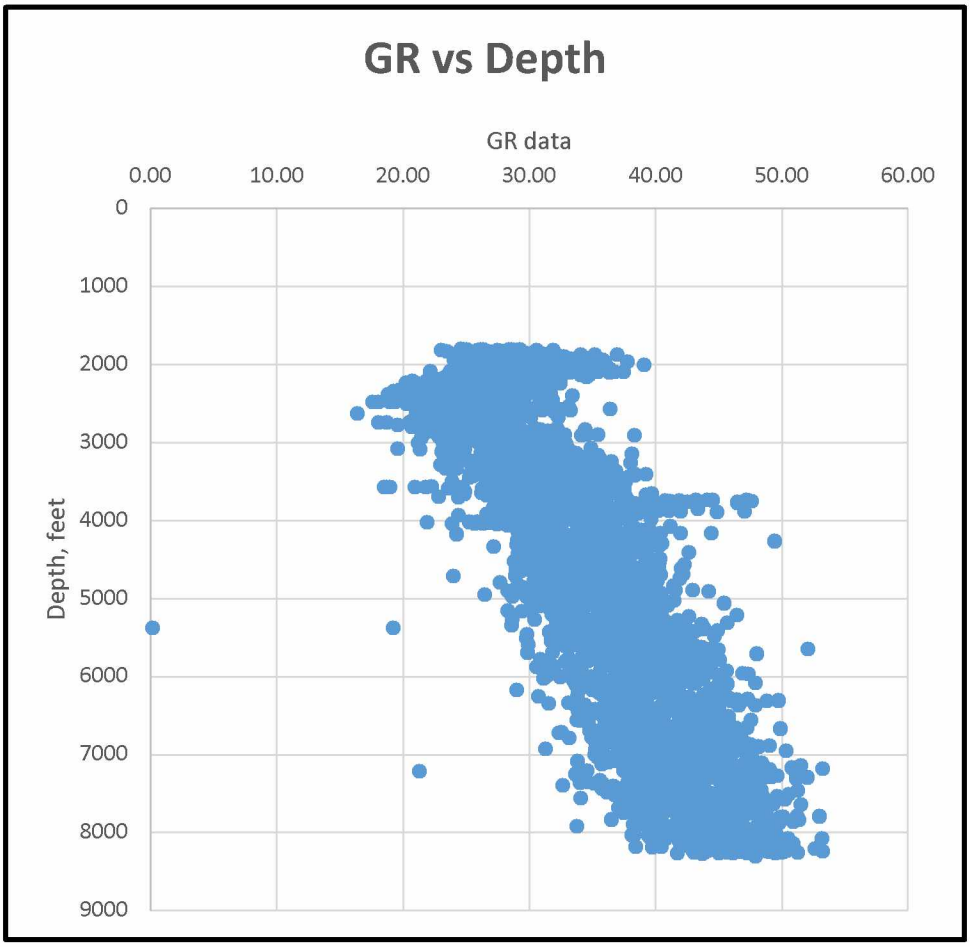

Figure 20. GR data plotted with depth to determine V_{shale}.

Overburden calculation

The density values derived from well log digitization for each depth value was used to calculate overburden pressure by using Equation 3. Specifically, a bulk density value for each depth is multiplied by the depth interval and gravitational acceleration to obtain

the overburden stress for a given interval (Lane and Macpherson 1976). The overburden stress accumulates or is integrated where overlying stress is combined as depth increases (Holbrook, Maggiori et al. 1995). The overburden for the Navarin Basin averaged around the expected value of 1.0 to 1.2 psi/ft. The overburden stress throughout the Navarin Basin is consistent with depth and follows a trend of increasing linearly with depth as show in Figure 21.

$$\sigma_v = \int \rho g dh$$

Equation 3.

Figure 21 shows the calculated overburden stress with depth for well 586 (Packard).

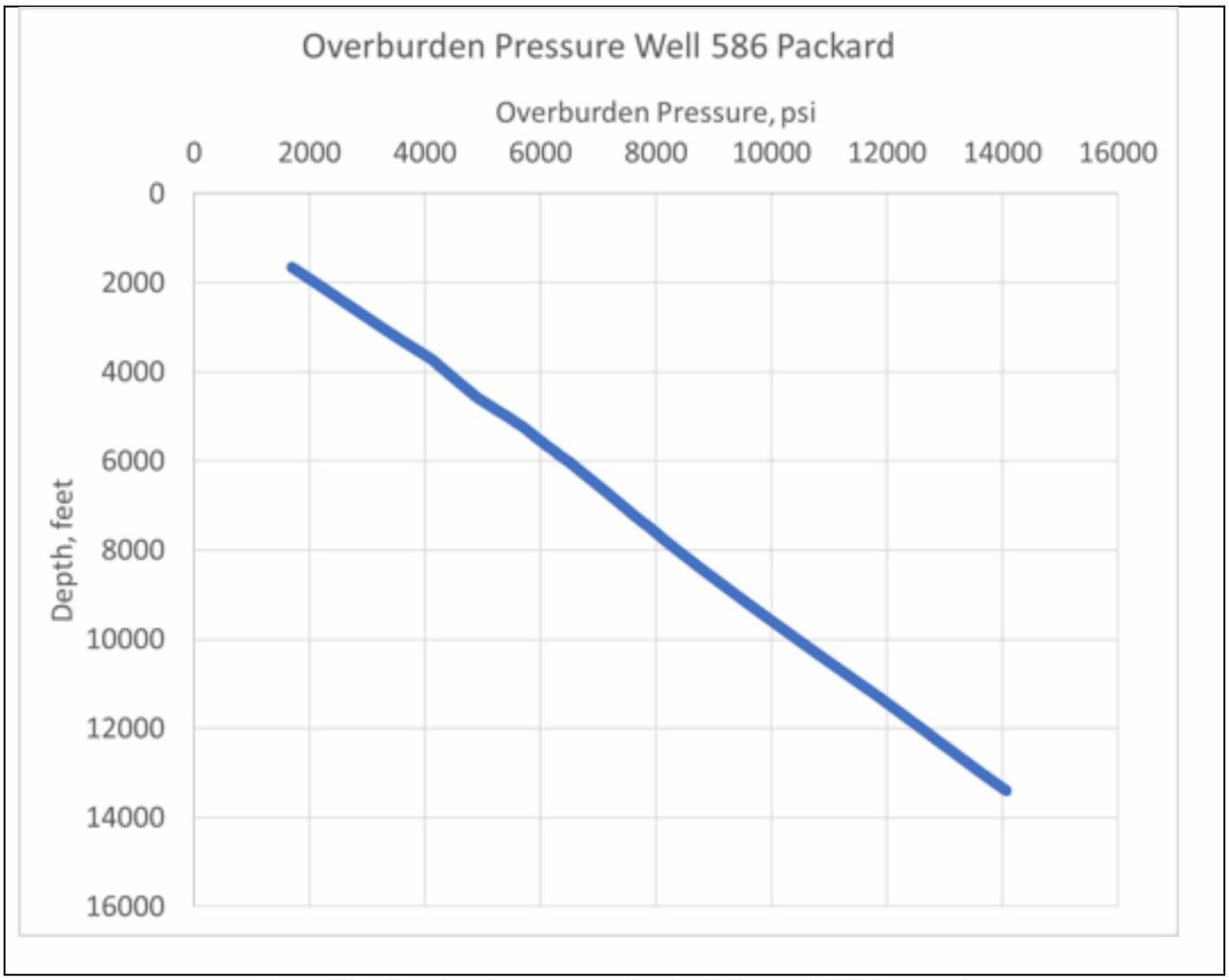

Figure 21. Overburden stress with depth for well 586 Packard.

Results and Discussion

Effective stress/sonic velocity plot Analysis

The vertical effective stress velocity plot for well 560 George shows a positive correlation with increasing vertical stress and increasing velocity (Figure 22). A power curve trend is fit to the data for all wells to reflect the asymptotic characteristics of the sonic velocity data; i.e. sonic velocity reaches a maximum value with increasing vertical effective stress. The purpose of plotting the vertical effective stress against the sonic velocity is to characterize and identify any unloading or reverse correlation between sonic velocity and vertical effective stress. The spread of the data may indicate some unloading; however, when the data is color coded for depth and pore pressure (Figure 23, Figure 24) it is clear that positive correlation between vertical effective stress and velocity that continues with respect to pressure increasing and the data spread is indicative of variation in the well log information. This relationship is indicative of disequilibrium compaction. There is a lack of indications for other overpressure mechanisms such as fluid expansion that would exhibit a backward or reverse correlation in the vertical effective stress - velocity plot.

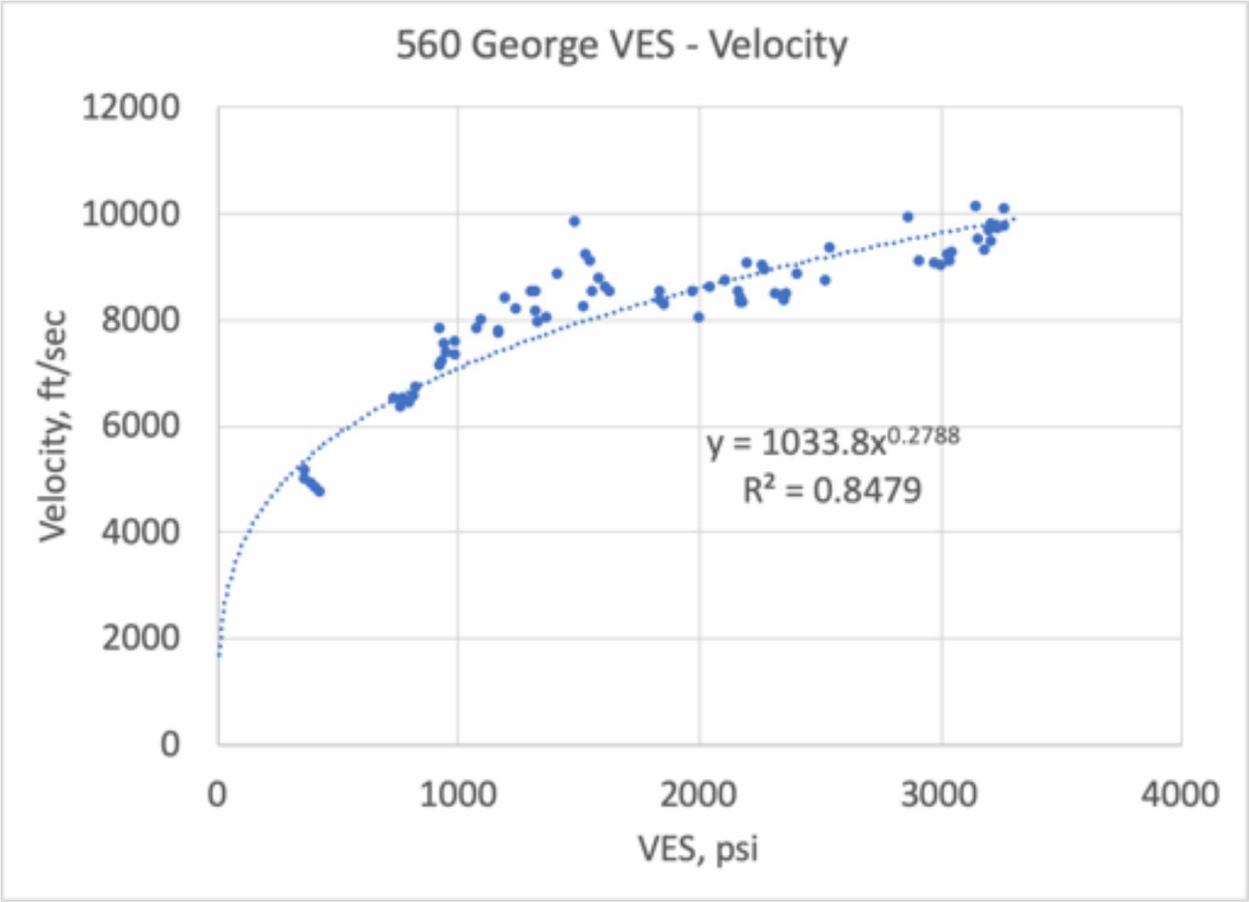

Figure 22. Vertical effective stress – velocity plot with loading curve for well 560 George.

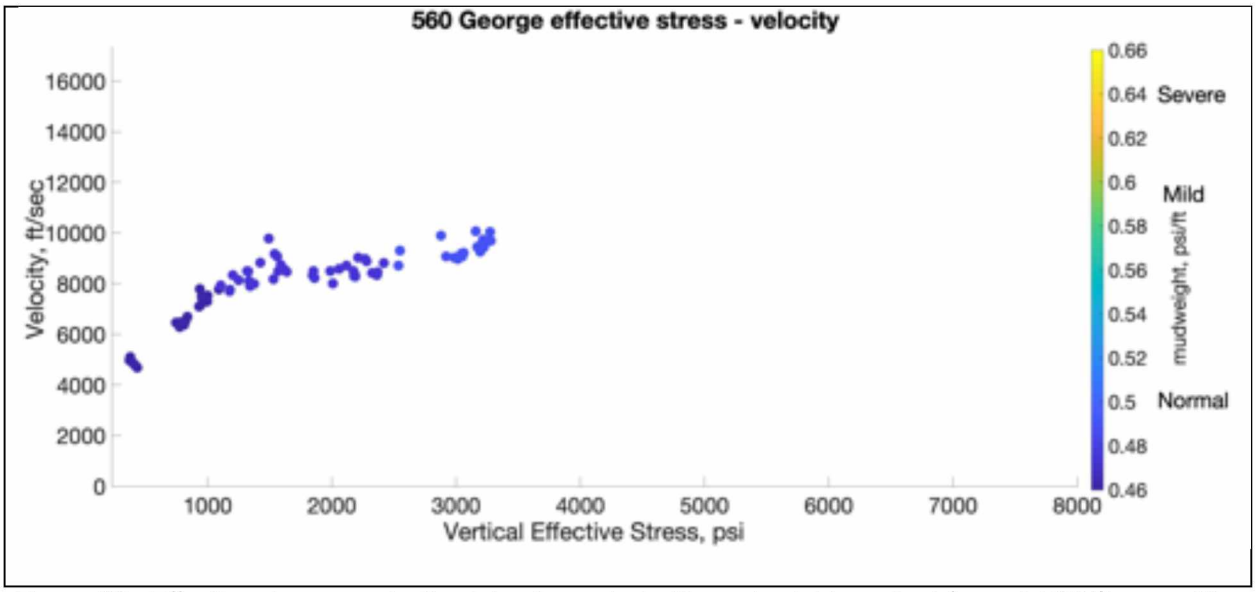

Figure 23. Effective stress – velocity plot color coded with mudweight gradient for well 560 George. The ranges for normal pressure as well as mild and sever overpressure are also on the color scheme.

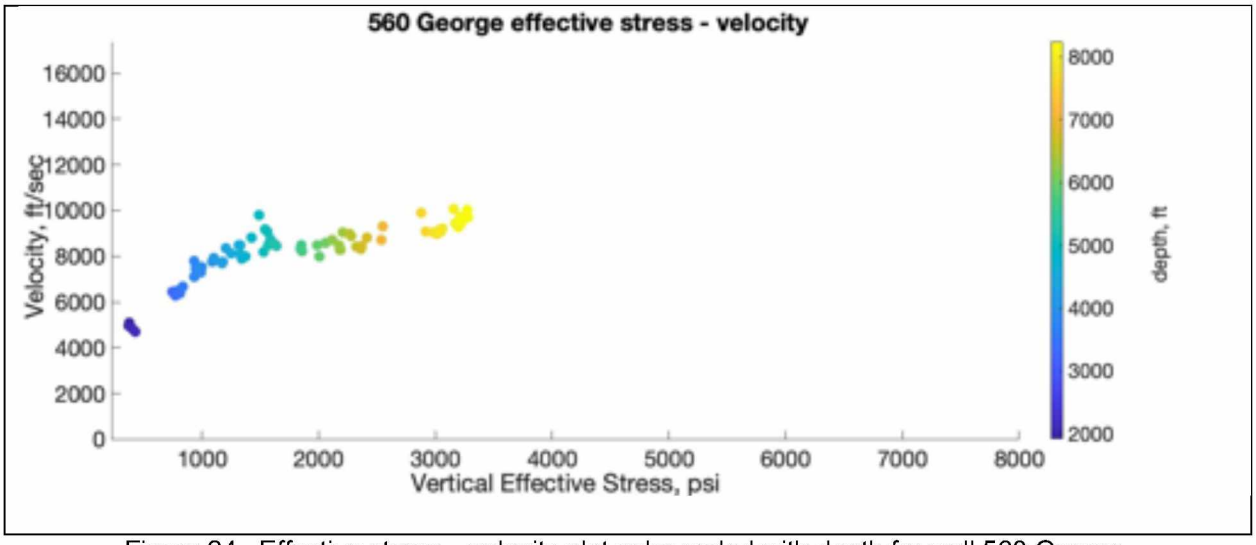

Figure 24. Effective stress – velocity plot color coded with depth for well 560 George.

The vertical effective stress velocity plot for well 583 Redwood 2 shows a positive correlation between velocity and vertical effective stress (Figure 25). This positive correlation may be indicative of disequilibrium compaction where the porosity decreases as vertical stress increases. Furthermore, (Figure 26, Figure 27) show that the positive

correlation between velocity and effective stress continues with respect to mudweight gradient and depth. There is no clear indication of higher pressure at a lower effective stress which would suggest the possibility of a fluid expansion mechanism of overpressure generation.

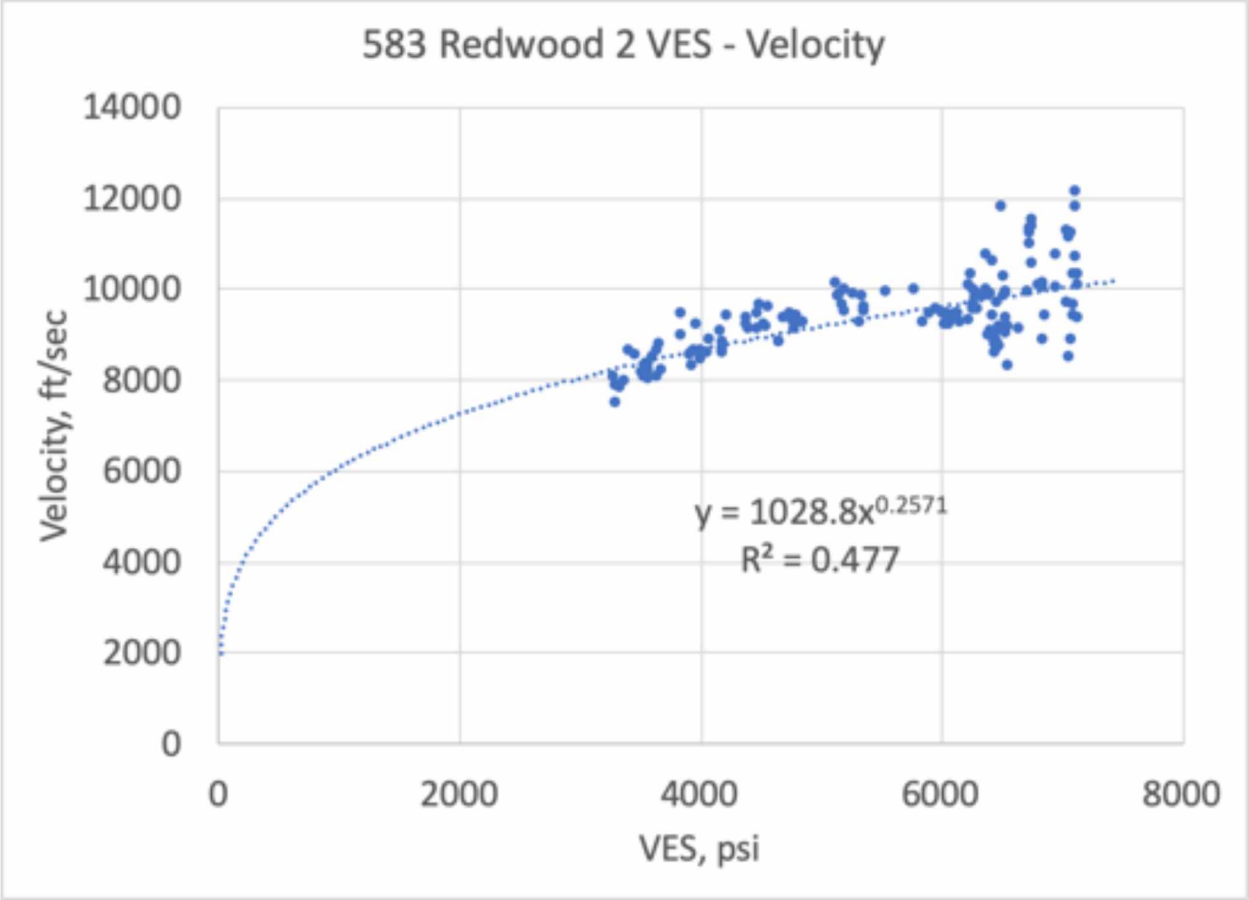

Figure 25. Effective stress – velocity plot with loading curve for well 583 Redwood 2.

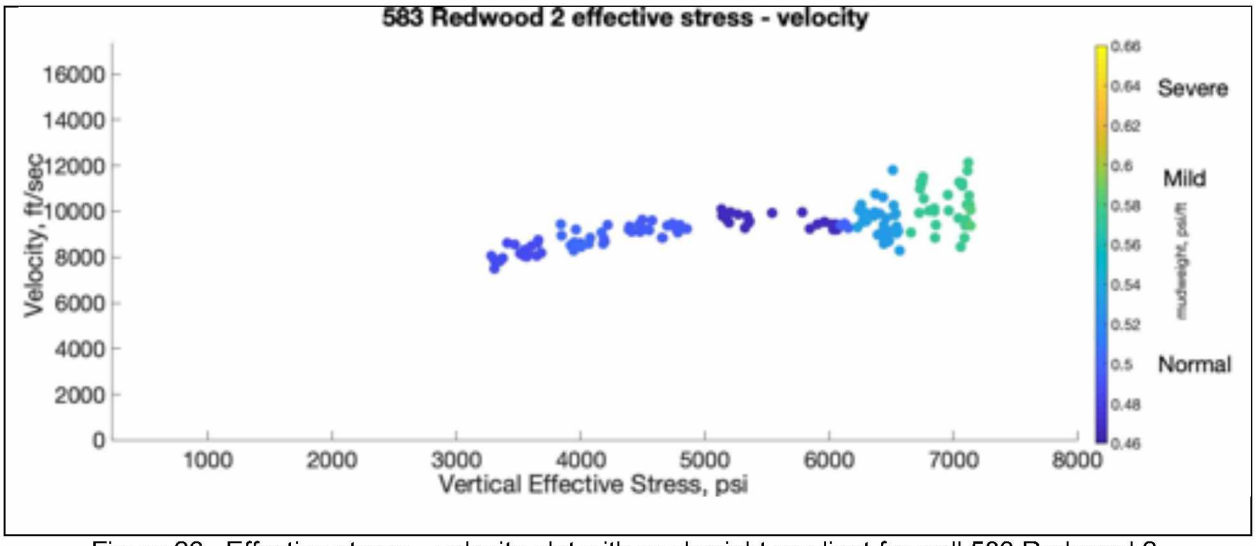

Figure 26. Effective stress – velocity plot with mudweight gradient for well 583 Redwood 2.

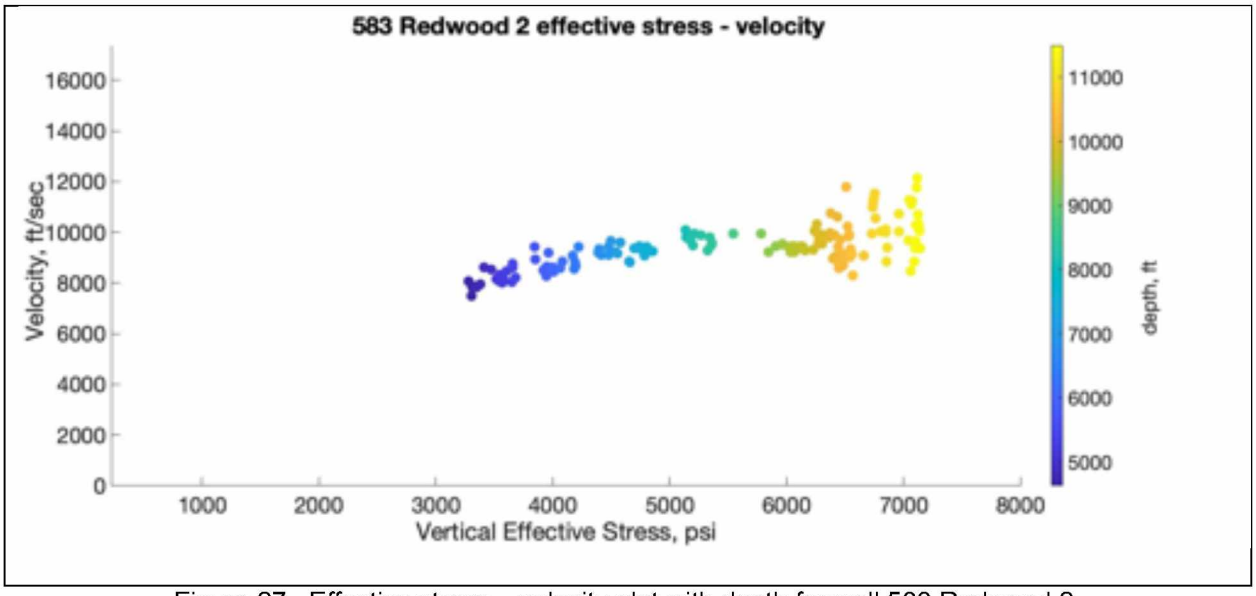

Figure 27. Effective stress – velocity plot with depth for well 583 Redwood 2.

The vertical effective stress velocity plot for well 586 Packard shows a positive correlation between velocity and vertical effective stress (Figure 28, Figure 30). The positive relationship is not as clear of defined as in other wells such as George and

Redwood 1; however, the general positive correlation is still indicative of disequilibrium compaction where the porosity decreases as vertical stress increases. Additionally, Figure 29 shows that the positive correlation between velocity and effective stress continues with respect to mudweight gradient, or that there is not a reverse trend in the velocity and effective stress data showing overpressure generating outside of the compaction trend. So, there is not enough indication of a reverse trend to suggest the possibility of a fluid expansion mechanism of overpressure generation.

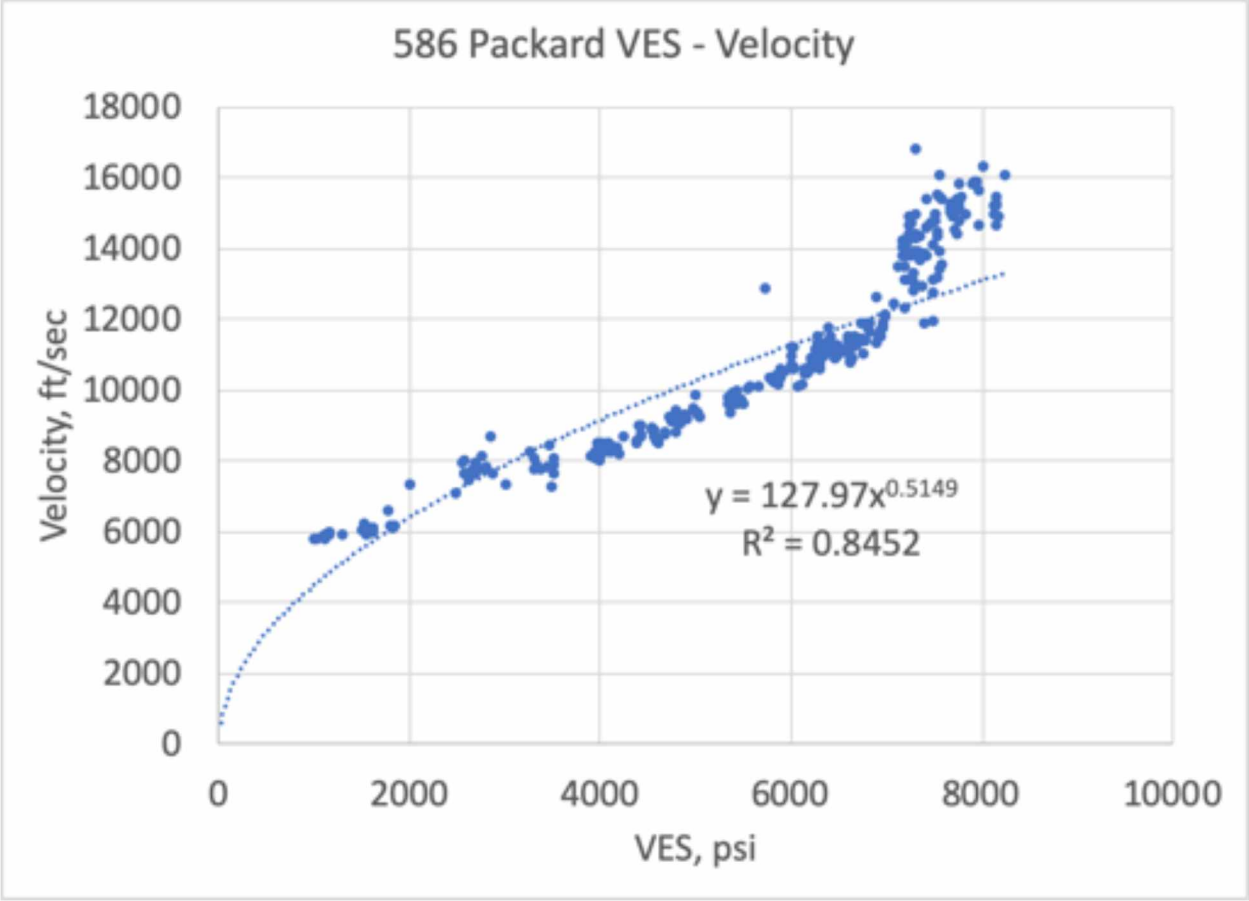

Figure 28. Effective stress – velocity plot with loading curve for well 586 Packard.

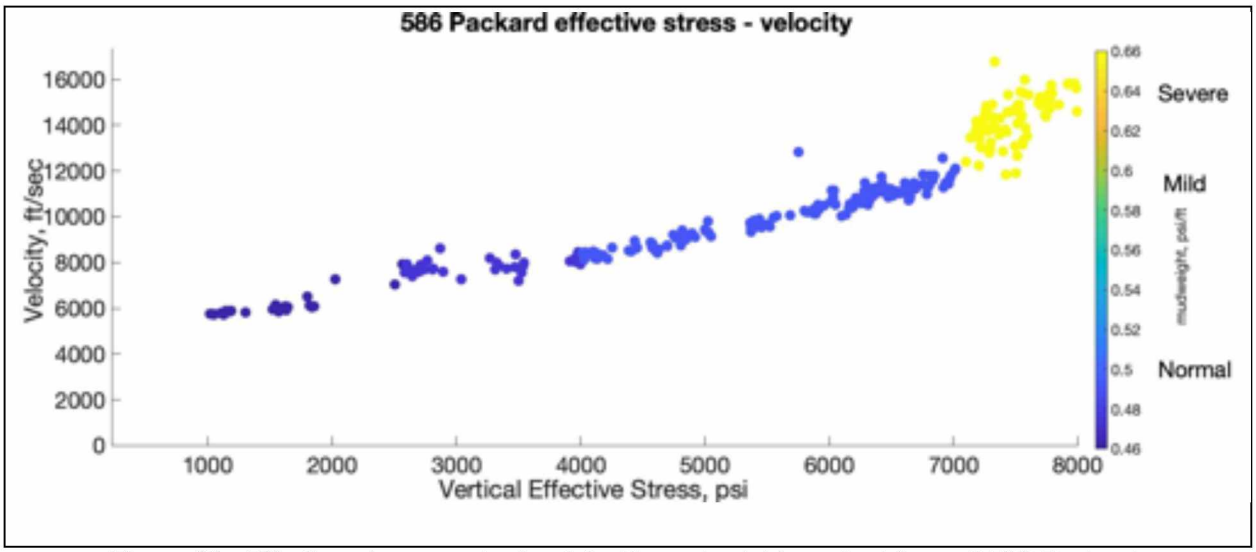

Figure 29. Effective stress – velocity plot with mudweight gradient for well 586 Packard.

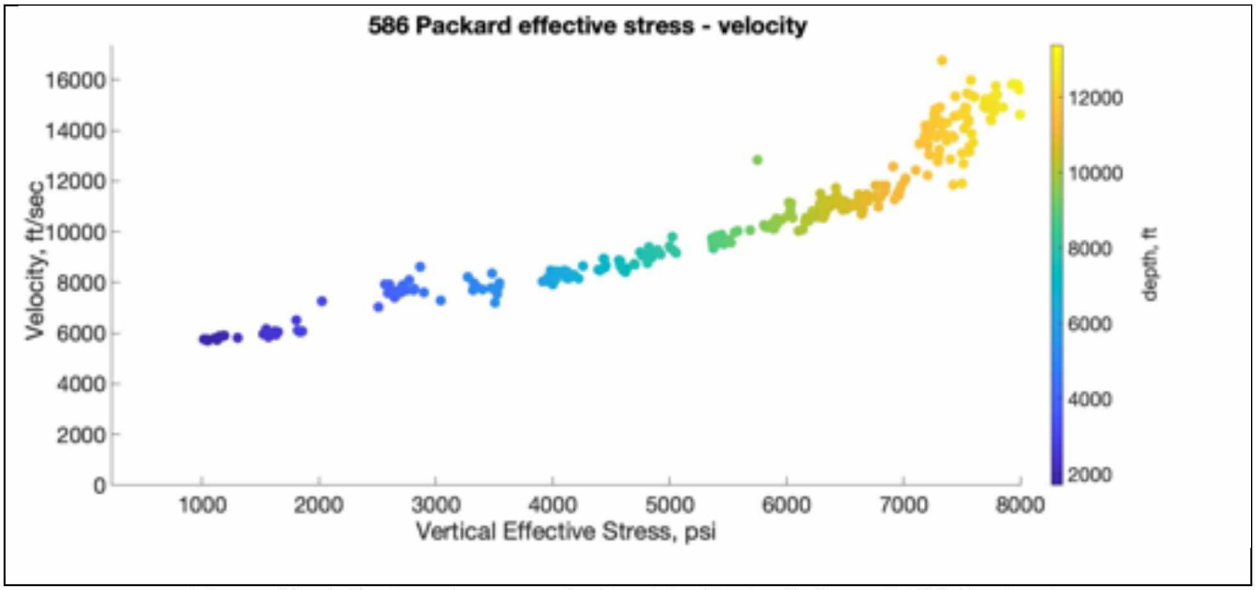

Figure 30. Effective stress – velocity plot with depth for well 586 Packard.

The vertical effective stress velocity plot for well 599 Redwood 1 shows a positive correlation between velocity and vertical effective stress (Figure 31, Figure 33). The positive relationship might show a signature of a reversal, but Figure 32 shows that the points with a high velocity value are still in line with a compaction trend where the

effective stress and velocity increase with pressure. The higher velocity point can therefore be attributed to unexpected values that are still indicative of disequilibrium compaction and not fluid expansion mechanisms of overpressure.

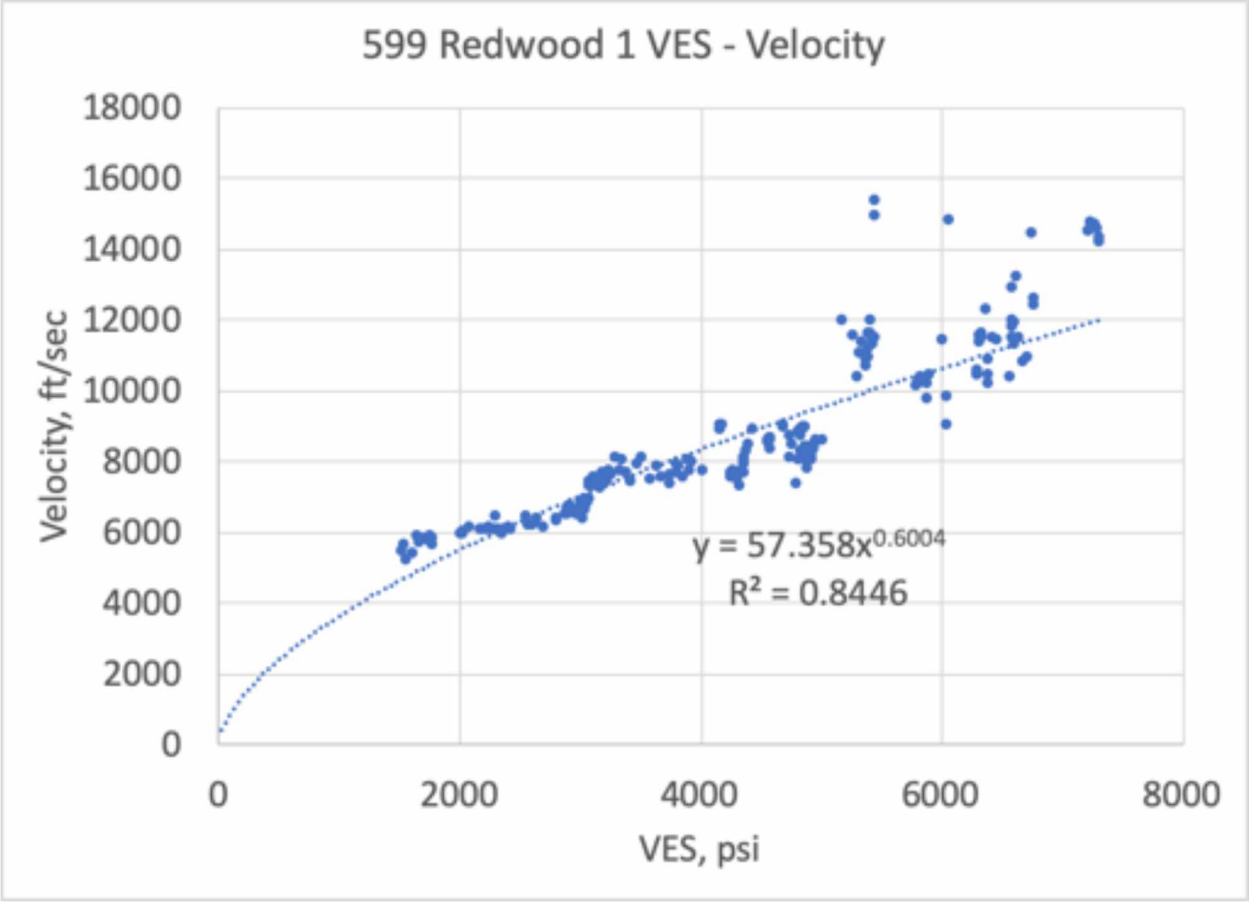

Figure 31. Effective stress – velocity plot with loading curve for well 599 Redwood 1.

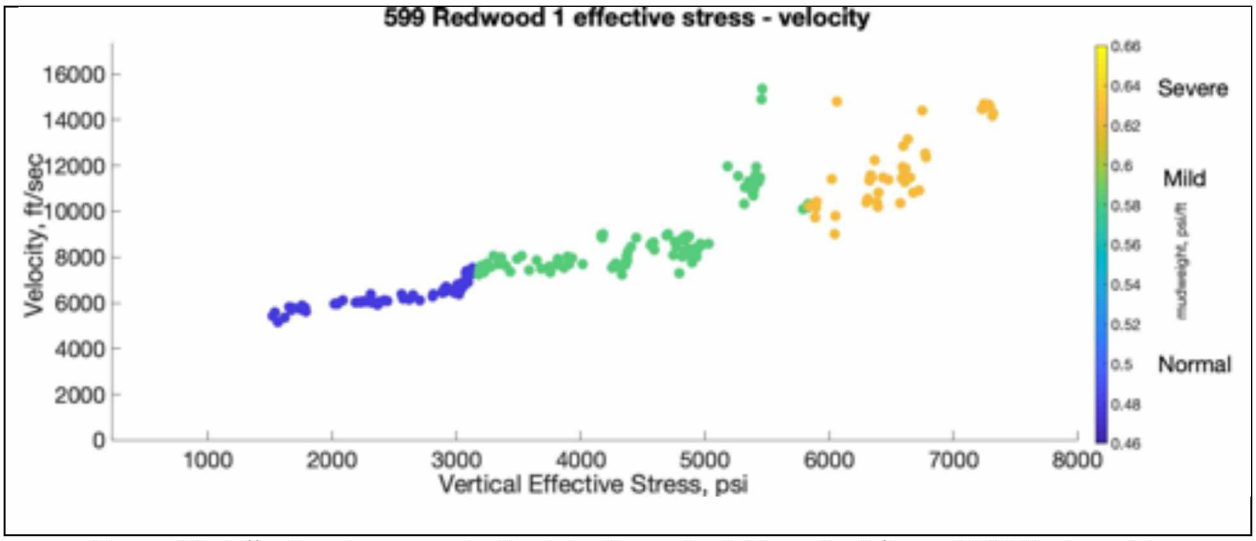

Figure 32. Effective stress – velocity plot with mudweight gradient for well 599 Redwood 1.

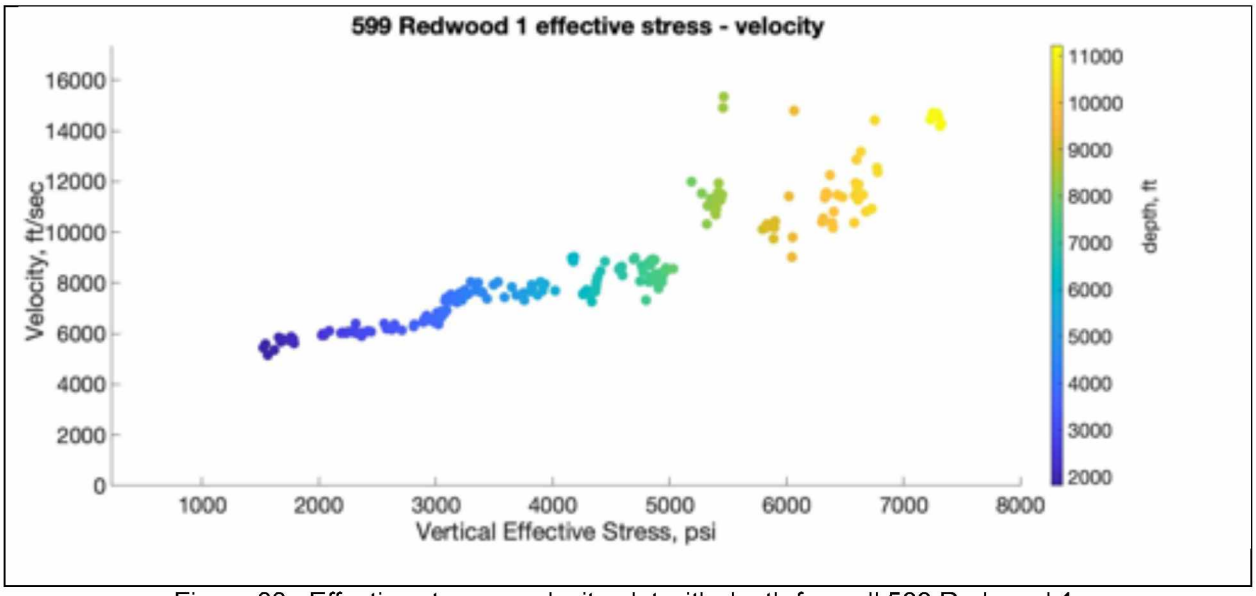

Figure 33. Effective stress – velocity plot with depth for well 599 Redwood 1.

Well 639 Danielle also shows a positive trend between vertical effective stress and velocity (Figure 34). Some data points exhibit great or lessor values for vertical effective stress or sonic velocity than the general trend. Figure 35 clarifies that with

increasing mudweight, the positive trend between velocity and vertical effective stress is maintained. Although Figure 34 shows a variation in sonic velocity at increasing vertical effective stress, Figure 36 shows that this variation occurs with depth due to expected variation in the well log data and not due to unloading. The trend supports overpressure generation by disequilibrium compaction as the positive trend between velocity and effective stress indicates the decreasing porosity with increasing vertical stress seen in compaction. The lack of reversal of effective stress with increasing pressure is also a lack of support for overpressure generation from other mechanisms like fluid expansion.

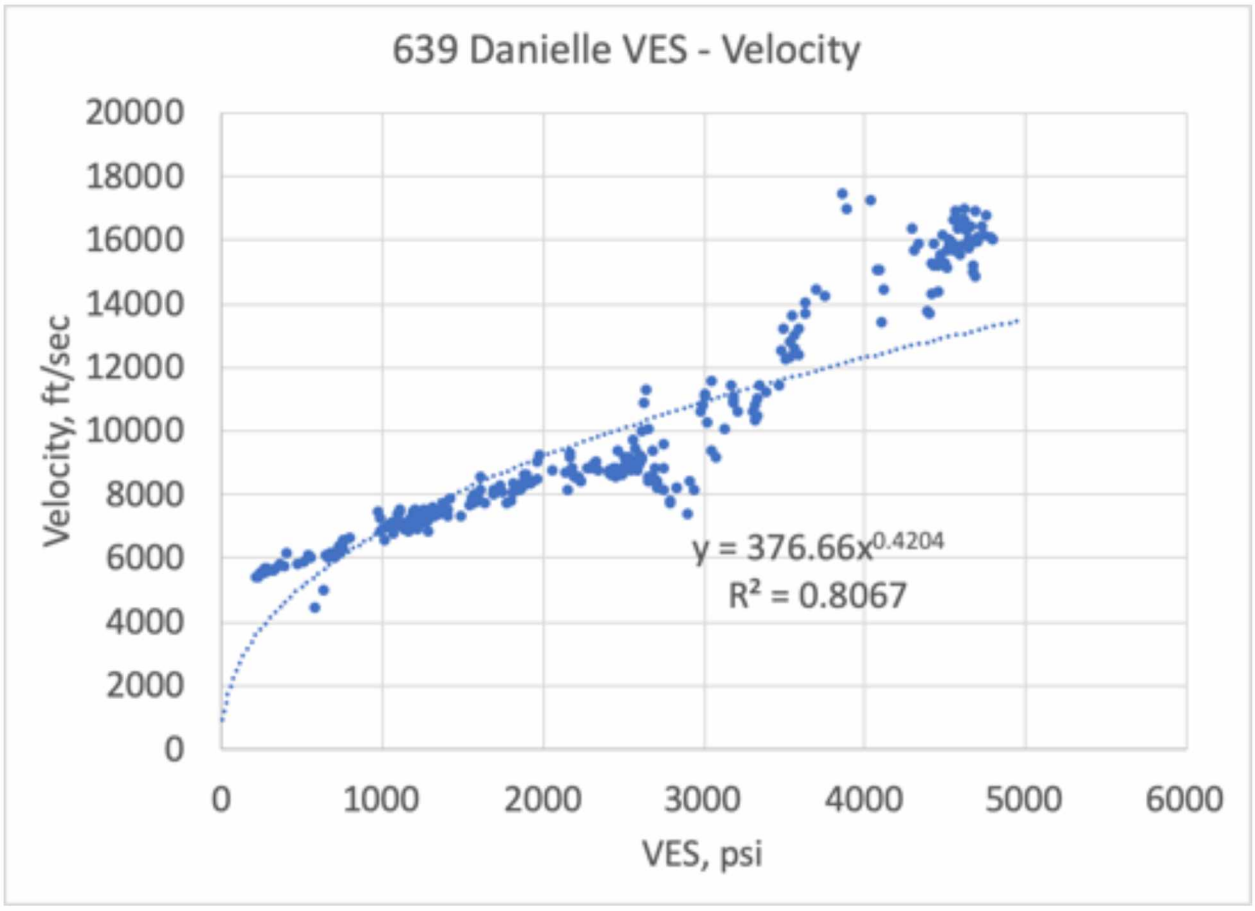

Figure 34. Effective stress – velocity plot with loading curve for well 639 Danielle.

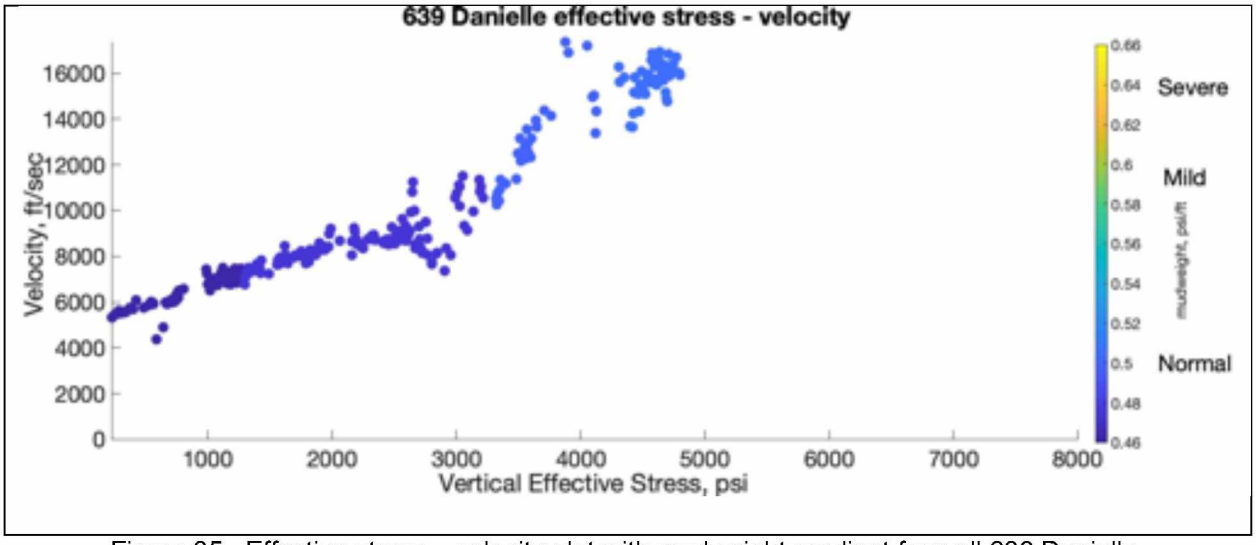

Figure 35. Effective stress – velocity plot with mudweight gradient for well 639 Danielle.

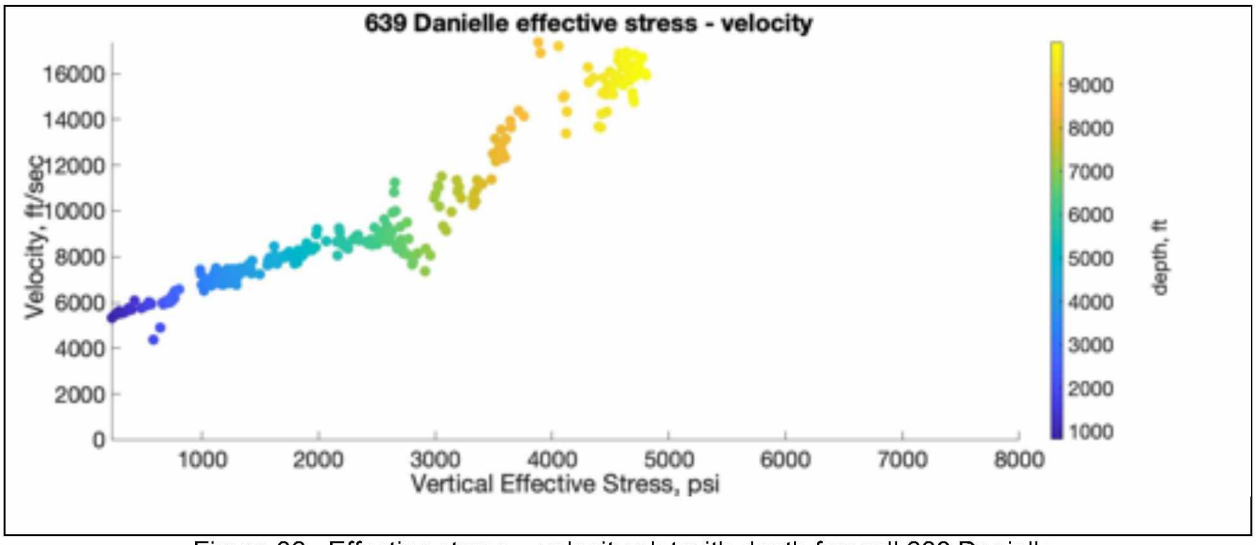

Figure 36. Effective stress – velocity plot with depth for well 639 Danielle.

Well 673 Misha velocity and vertical effective stress data shows a positive correlation (Figure 37, Figure 38, Figure 39). There is a slight deviation for a completely positive linear correlation with some data above or below the normal compaction trend. However, the trend is confirmed as normal as the data shows a positive trend when organized according to mudweight gradient (Figure 38). The lack of any reversal in the compaction trend (or any constant velocity or decreasing effective stress as mudweight increases) rules out the mechanism of overpressure due to fluid expansion. The general positive correlation between increasing velocity and increasing effective stress supports the mechanism of compaction contributing to any overpressure.

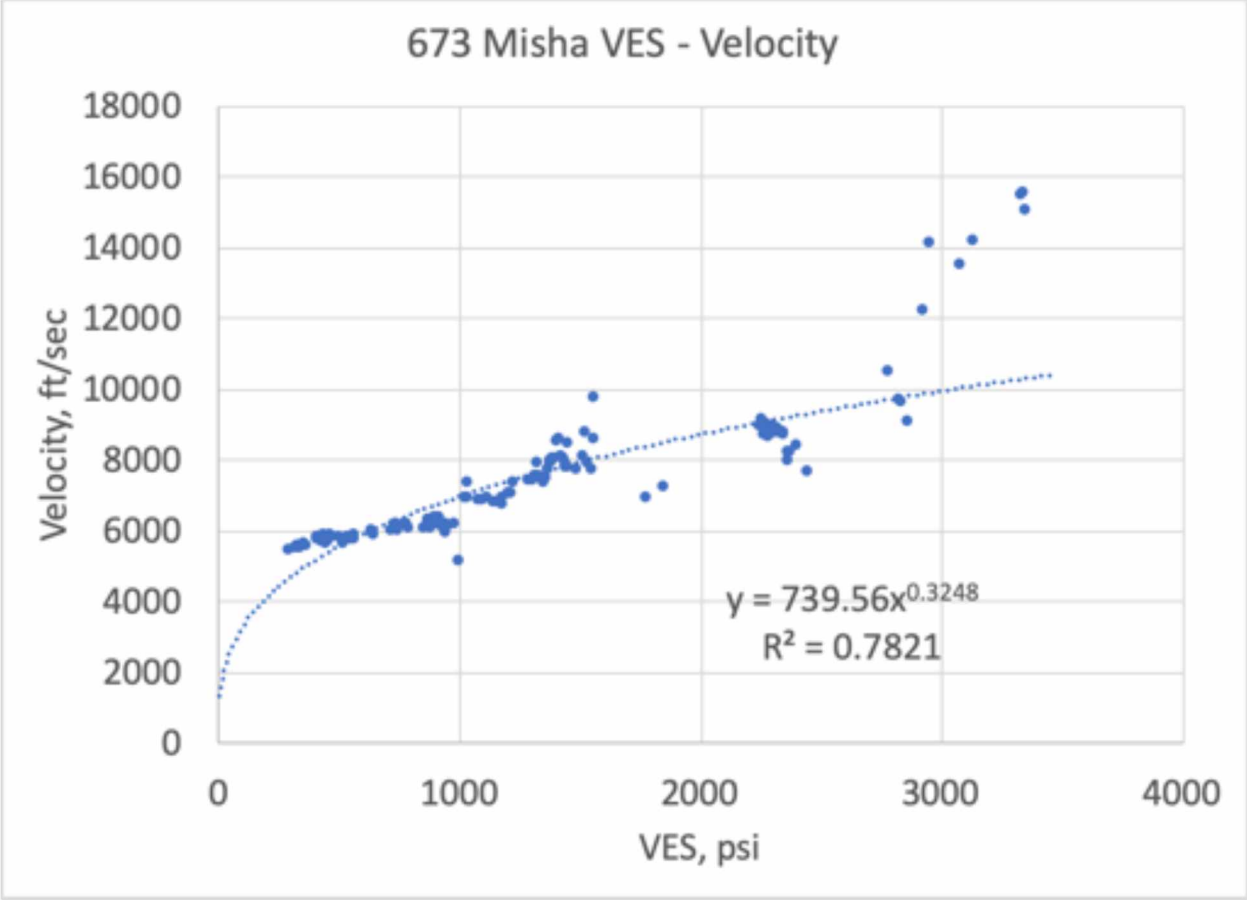

Figure 37. Effective stress – velocity plot with loading curve for well 673 Misha.

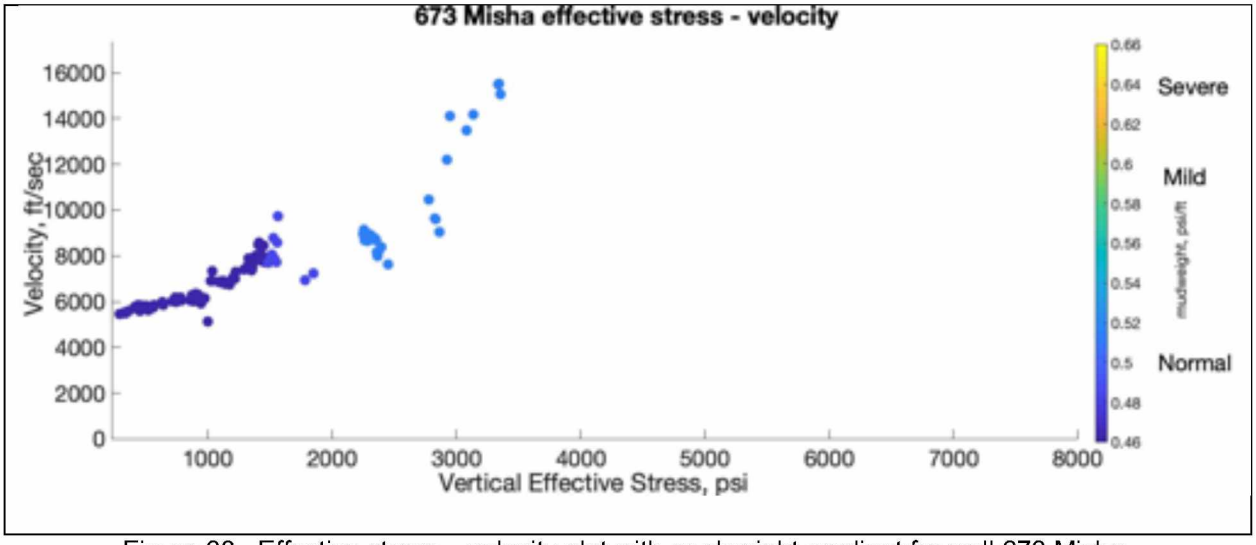

Figure 38. Effective stress – velocity plot with mudweight gradient for well 673 Misha.

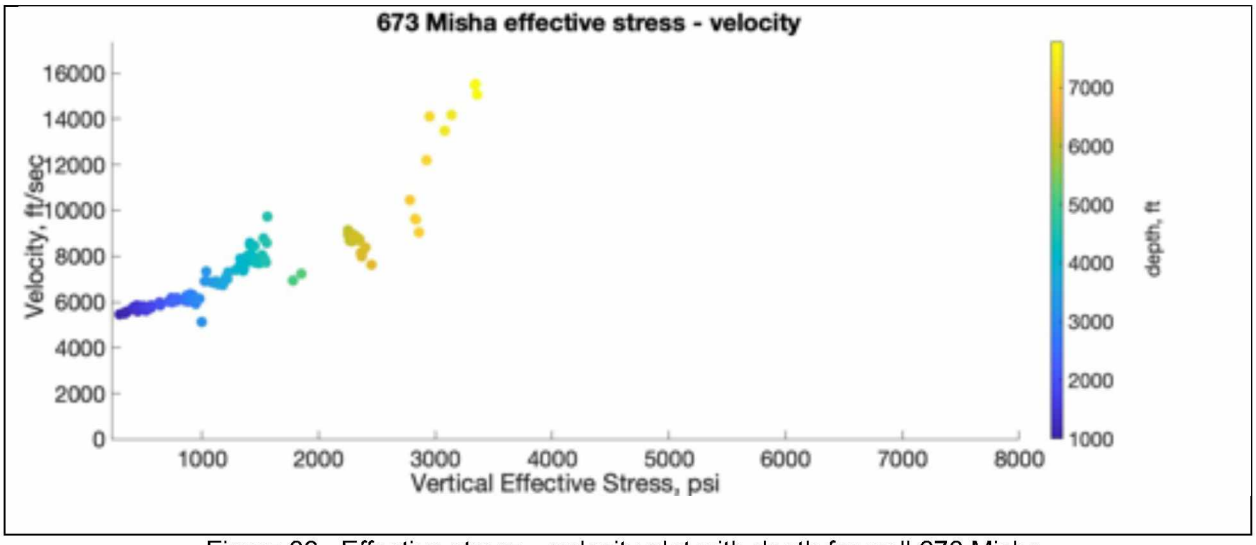

Figure 39. Effective stress – velocity plot with depth for well 673 Misha.

The vertical effective stress velocity plot for the well log data from well 707 Nicole shows a positive correlation of increasing velocity and increasing effective stress (Figure 40, Figure 41, Figure 42). Any deviations from the normal compaction trend are explained by graphing the mudweight gradient and observing that the mudweight also increases as the velocity and effective stress increase (Figure 41). The absence of any effective stress reversals or velocity freezing rules out fluid expansion mechanisms for consideration of overpressure generation. Disequilibrium compaction overpressure generation is identified with the increasing velocity, and effective stress correlation suggesting a normal compaction trend.

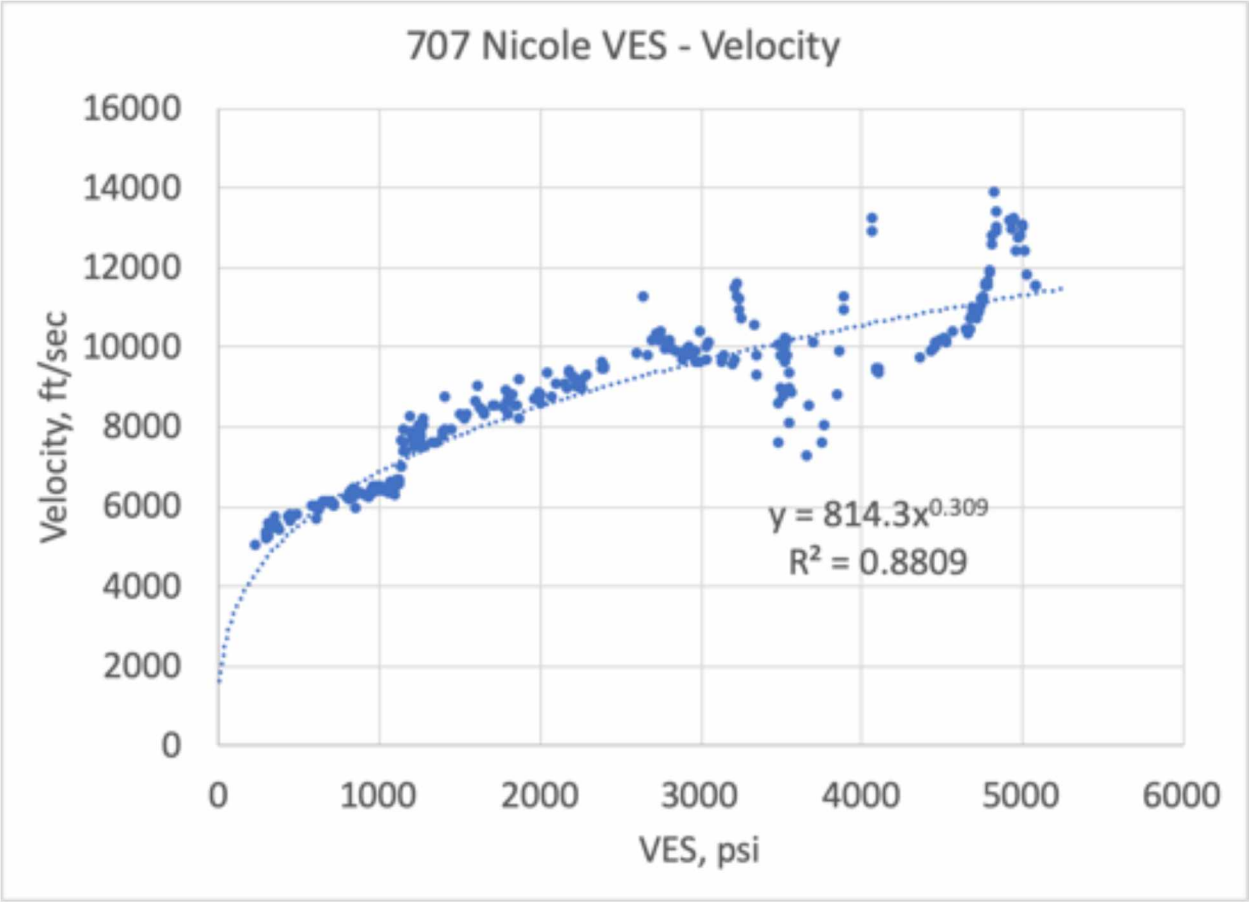

Figure 40. Effective stress – velocity plot with loading curve for well 707 Nicole.

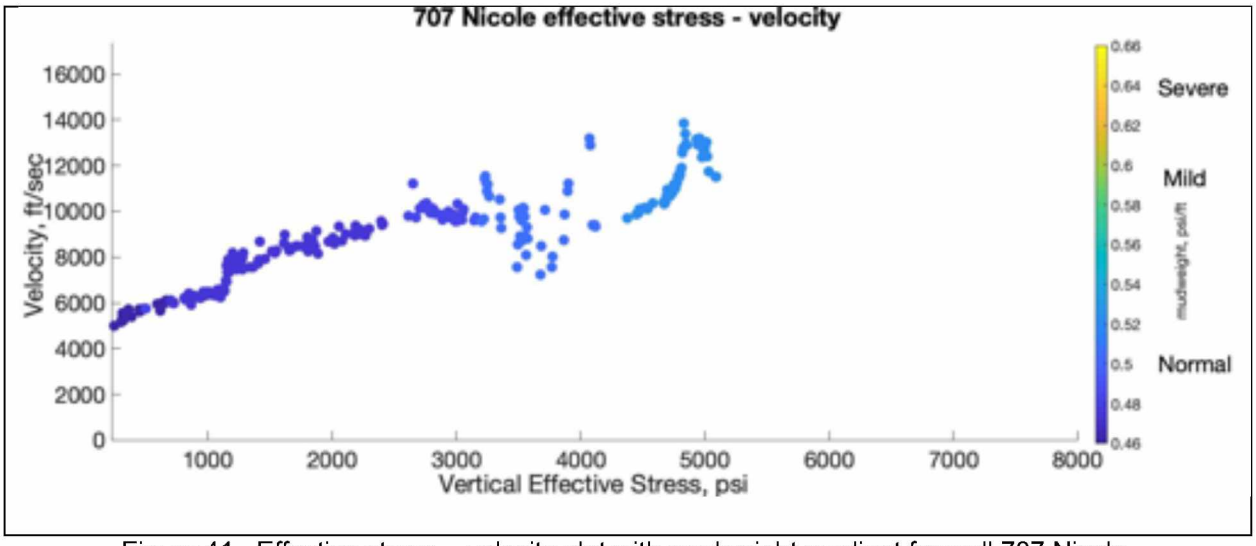

Figure 41. Effective stress – velocity plot with mudweight gradient for well 707 Nicole.

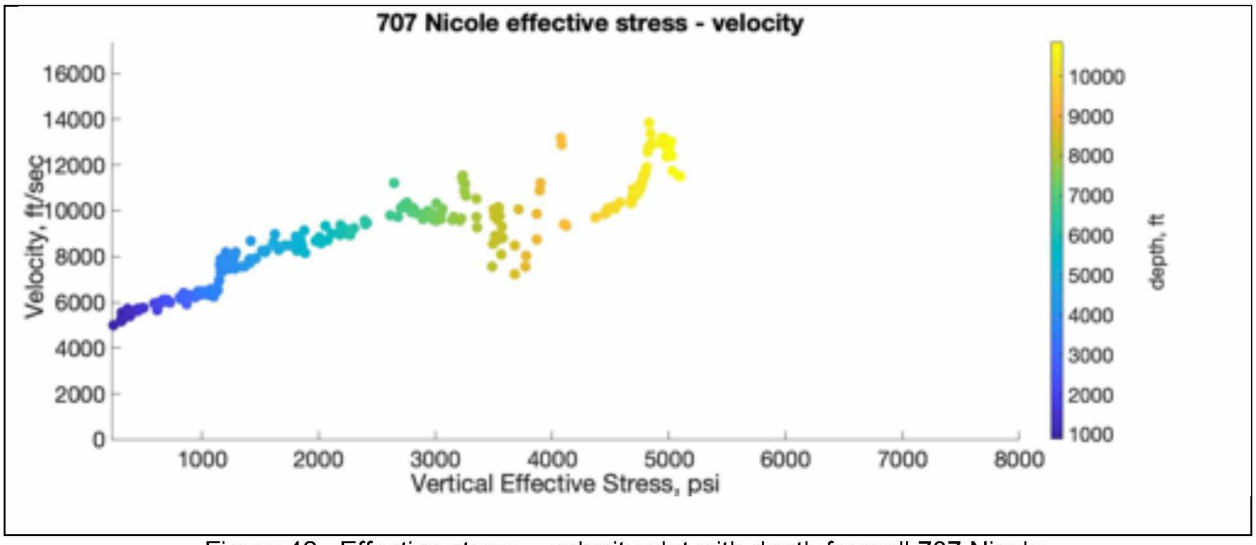

Figure 42. Effective stress – velocity plot with depth for well 707 Nicole.

Plotting the vertical effective stress and velocity data for well 719 Nancy shows a clear correlation where velocity and effective stress increase together at an exponential rate

(Figure 43, Figure 45). Also plotting the vertical effective stress and velocity organized by mudweight shows that the positive correlation is maintained as formation pressure increases (Figure 44). The strong positive correlation shows a normal compaction trend which is the primary overpressure mechanism from disequilibrium compaction. The lack of any reversal of effective stress or rollback from the effective stress velocity plot rules out that fluid expansion plays a role in overpressure generation in well 719 Nancy.

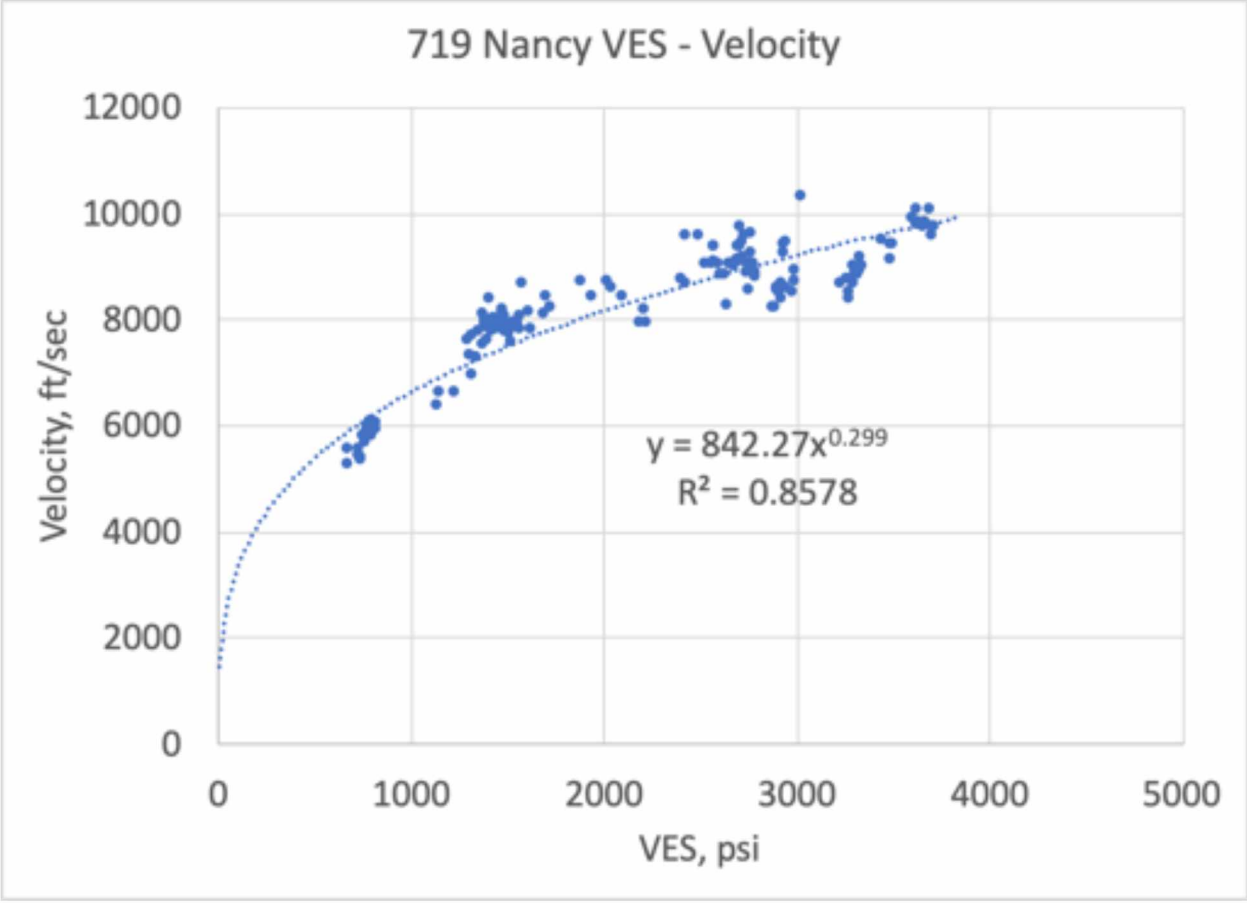

Figure 43. Effective stress – velocity plot with loading curve for well 719 Nancy.

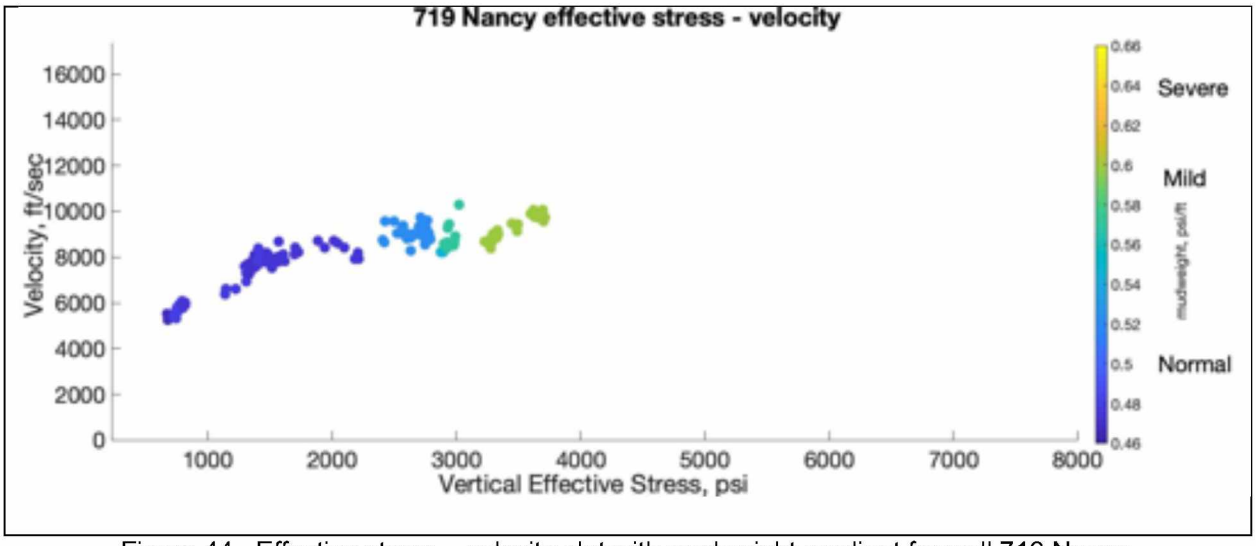

Figure 44. Effective stress – velocity plot with mudweight gradient for well 719 Nancy.

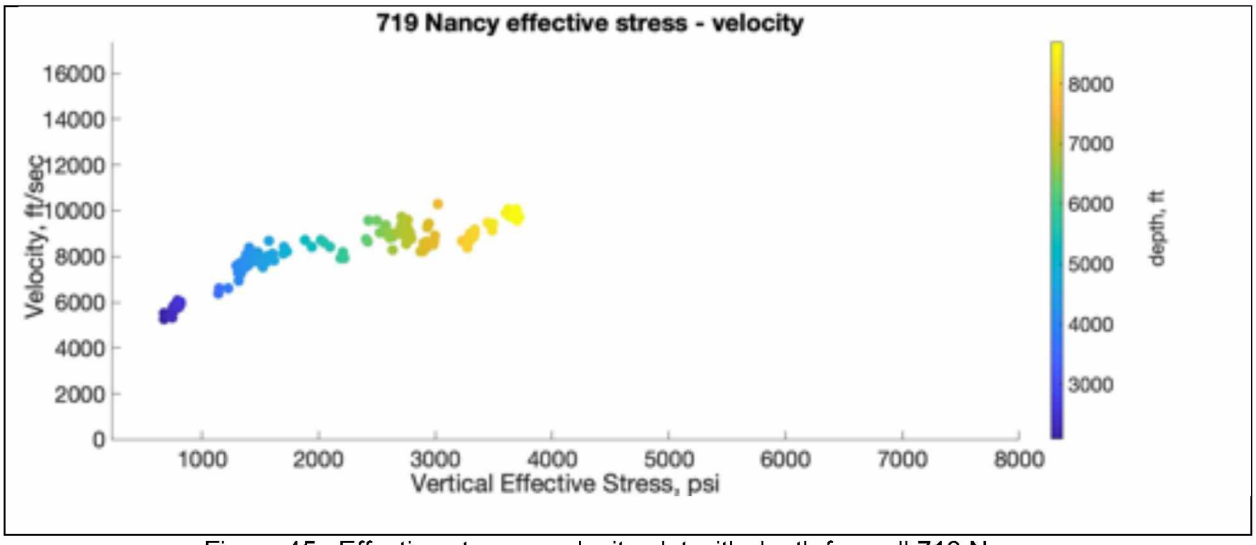

Figure 45. Effective stress – velocity plot with depth for well 719 Nancy.

Crossplot Analysis

Several correlations have been proposed in the literature to determine bulk density information from sonic velocity data, and vice versa (Ludwig 1970, Gardner, Gardner et al. 1974, Christensen and Mooney 1995, Godfrey, Beaudoin et al. 1997, Bowers 2001, Dutta 2002, Brocher 2005). As shown in Equation 4, Ludwig (1970) proposed a correlation to obtain sonic velocity data from bulk density data using a polynomial model (Ludwig 1970).

$$V_p = 1.6612\rho - 0.4721\rho^2 + 0.0671\rho^3 - 0.0043\rho^4 + 0.00106\rho^5$$

Equation 4.

Gardener (1974), developed a relationship between bulk density and sonic velocity based on an exponential correlation (Gardner, Gardner et al. 1974).

$$\rho = 1.74V_p^{0.25}$$

Equation 5.

Christensen and Mooney (1995) observed that bulk density and sonic velocity are linearly related with the corresponding linear equation (Christensen and Mooney 1995).

$$\rho = 0.3601V_p + 0.541$$

Equation 6.

Godfrey (1997) also observed a linear relationship between bulk density and sonic velocity with different slope and intercept values (Godfrey, Beaudoin et al. 1997).

$$\rho = 0.0761V_p + 2.4372$$

Equation 7.

Bowers (2001) developed bounds for bulk density and sonic velocity data by determining a nonlinear power relationship between density and velocity (Bowers 2001).

$$V_p = 4790 + 2953(\rho - 1.3)^{3.57}$$

Equation 8.

Dutta (2001) correlated bulk density and sonic velocity for Smectitic and Illitic clay formations, creating bounds for clay formations (Dutta 2001).

$$\rho = 0.1886V_p + 1.8655$$

Equation 9.

$$\rho = 0.1964V_p + 1.586$$

Equation 10.

Brocher 2005 observed another density and sonic velocity correlation where bulk density can be obtained from a polynomial manipulation of sonic velocity data from existing correlations (Brocher 2005).

$$\rho = 39.128V_p - 63.064V_p^2 + 37.083V_p^3 - 9.1819V_p^4 + 0.8228V_p^5$$

Equation 11.

Figure 46 shows the sonic velocity – bulk density equations listed above represented graphically as well as all velocity and density data for the Navarin Basin exploratory wells.

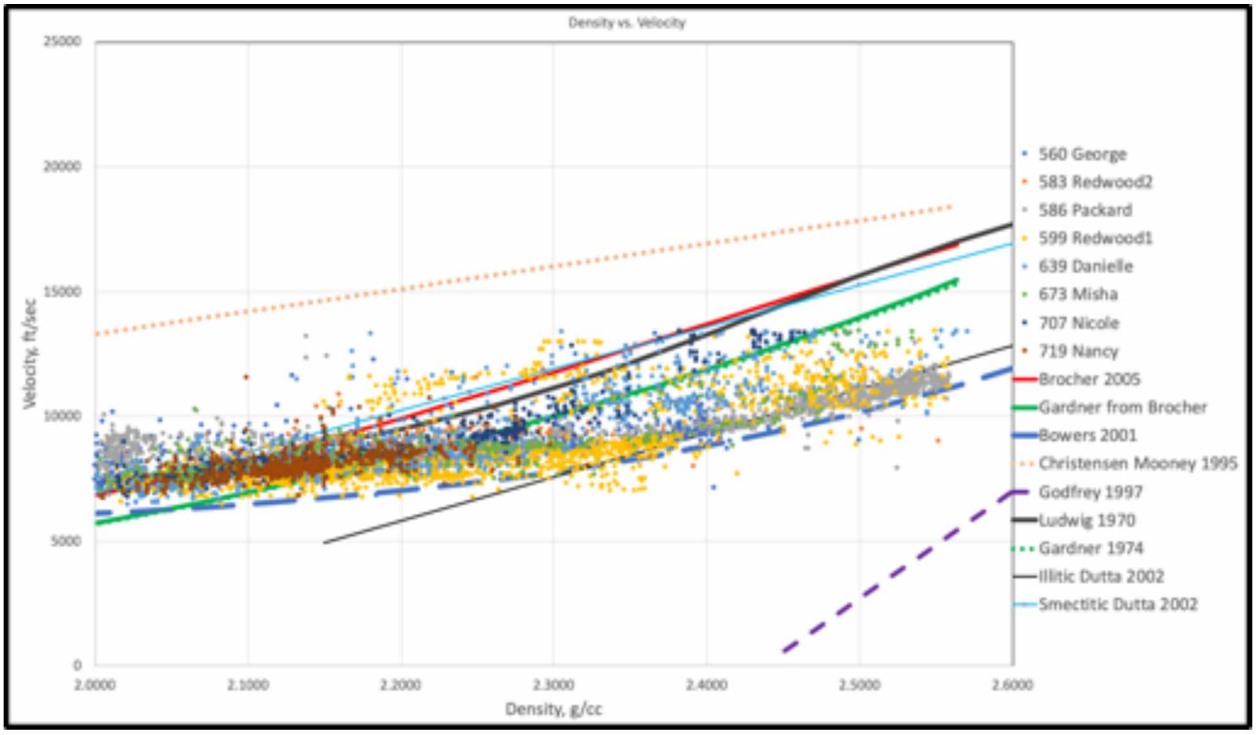

Figure 46. Determining upper and lower bounds for density velocity crossplots.

The velocity and bulk density well log data for the eight exploratory wells were plotted together with the velocity bulk density correlations to determine if the data fit within the bounds of the bulk density and velocity models (Figure 46). The data fit well within an upper bound determined by the Ludwig correlation (Equation 4) and a lower bound set

by the Bowers correlation (Equation 8). Since the density velocity correlations were developed based on field measurements from sonic velocity and bulk density or models developed from field observations, it can be determined that the data derived from the well log information for the eight exploratory wells in the Navarin Basin is realistic and not erroneous data. Figure 47 shows the aggregate Navarin Basin well velocity and density data with only the Ludwig and Bowers bounds illustrating the fit of the vast majority of the data within the determined bounds.

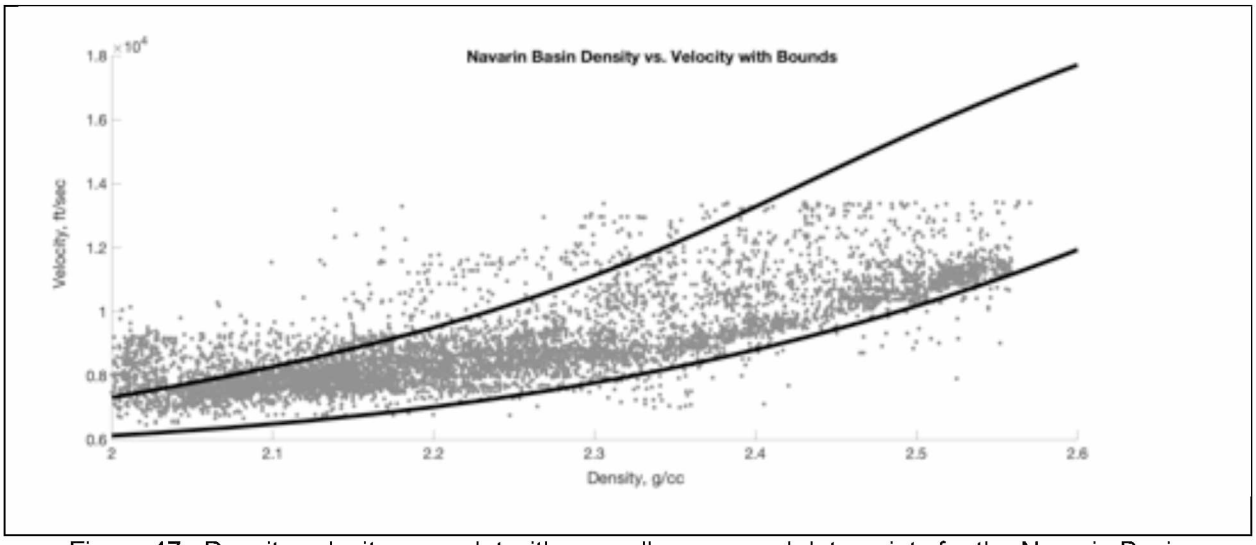

Figure 47. Density velocity crossplot with normally pressured data points for the Navarin Basin exploratory wells.

Mudweight data available for well 583 Redwood 2 showed a gradient of 0.6 psi/ft or enough pressure to be considered mild overpressure. Density velocity crossplots showed reversal or rollback along the normal compaction trend (Figure 48, Figure 49). The density and velocity data followed a normal trend where density and velocity increase under normal compactions conditions. In other words, the porosity of the

formations decreases and the density increases as the formations are buried and compacted. The density velocity crossplot shows that at some depth around 10,000 feet, there is a reversal where the density and velocity are not increasing probably due to an inability of water to escape the decreasing pore space (Figure 48). The density velocity crossplot organized by mudweight also shows the slow or reversal of the compaction trend when the pressure approaches mild overpressure (Figure 49). Density resistivity crossplots show the same general trends, but not as reliable or clean as the density velocity crossplots (Figure 50, Figure 51). These behaviors suggest that the mechanism of overpressure is disequilibrium compaction. The absence of continued increases in velocity density with higher pressures rules out fluid expansion overpressure mechanisms.

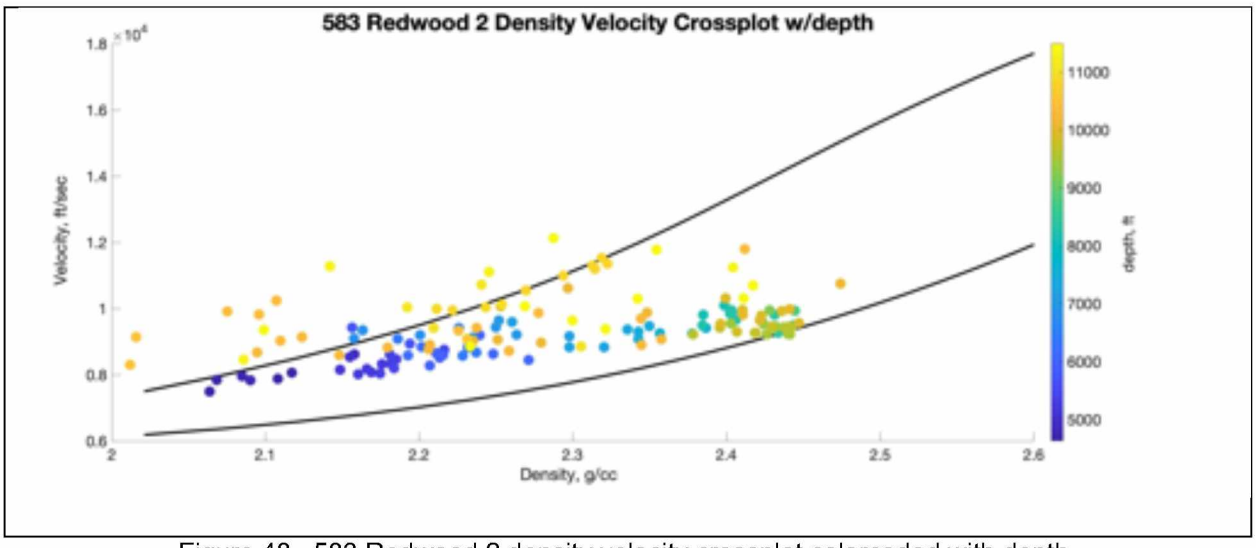

Figure 48. 583 Redwood 2 density velocity crossplot colorcoded with depth.

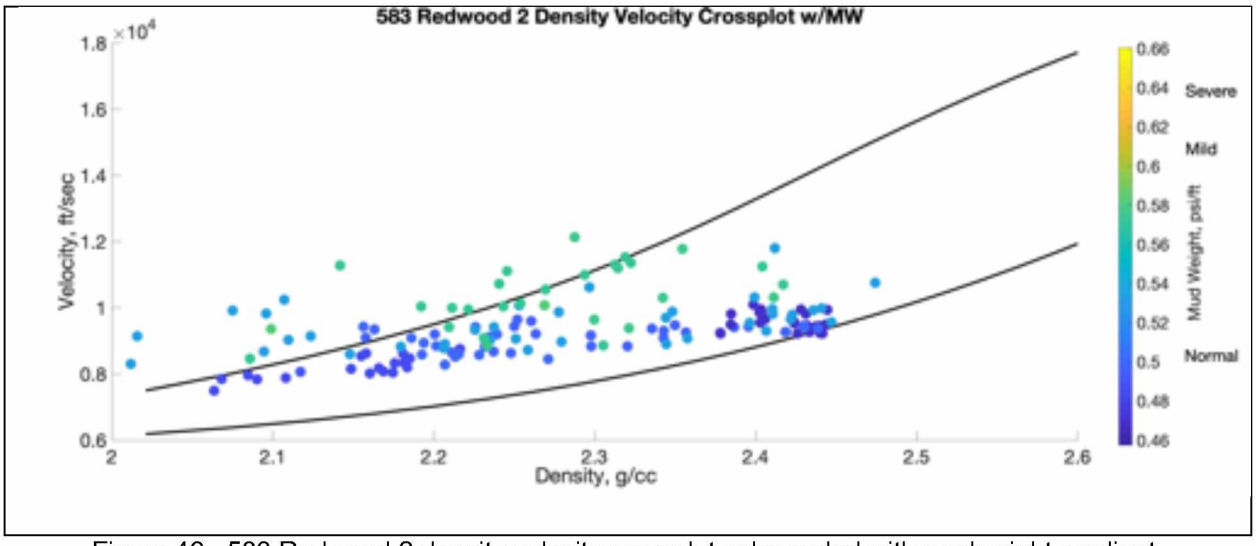

Figure 49. 583 Redwood 2 density velocity crossplot color coded with mudweight gradient.

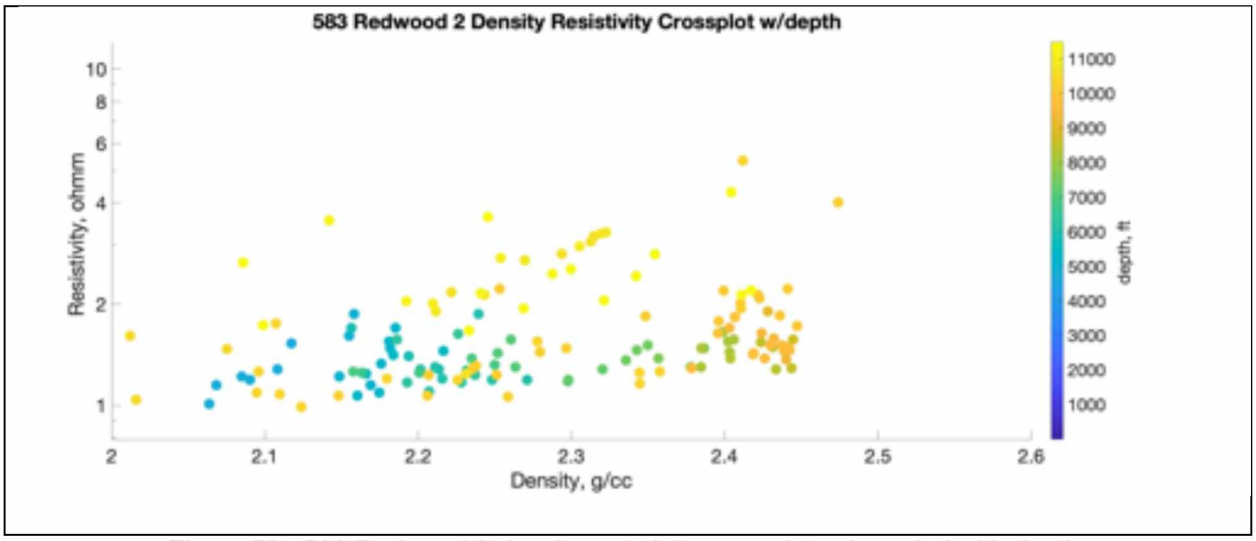

Figure 50. 583 Redwood 2 density resistivity crossplot colorcoded with depth.

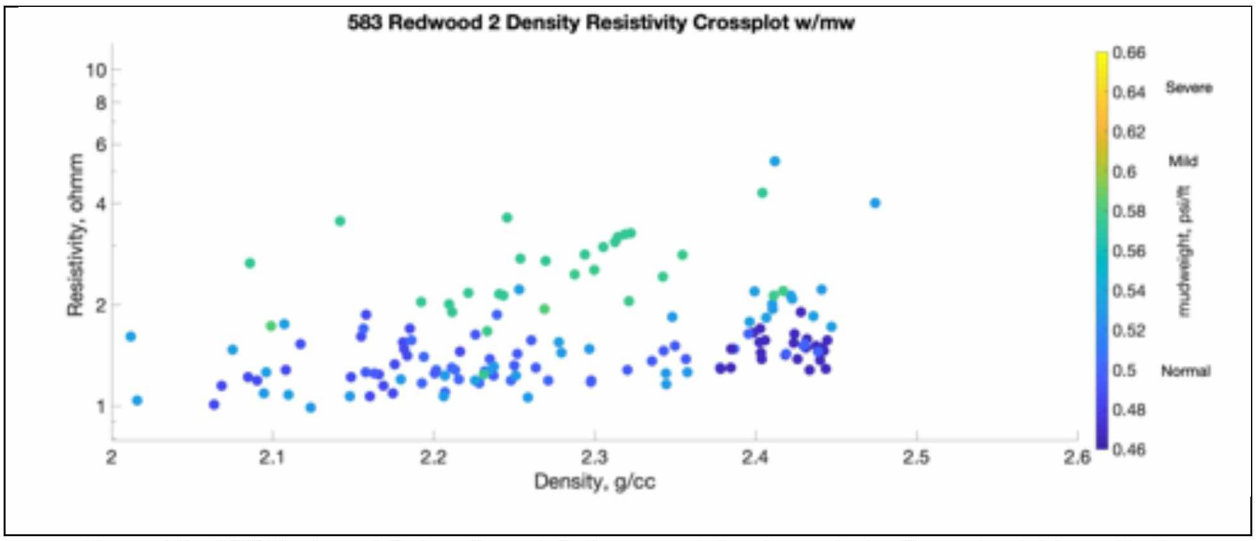

Figure 51. 583 Redwood 2 density resistivity crossplot color coded with mudweight gradient.

Mudweight data shows severe overpressure at depths greater than 10,000 feet for well 586 Packard. Density velocity crossplots show the overpressure zone as a reversal of the normal compaction trend, which is support for disequilibrium compaction overpressure generation (Figure 52, Figure 53). Additionally, the average overpressure zone lies very close to the upper bound for the density velocity data (Figure 52, Figure 53). Fluid expansion mechanisms of overpressure are supported with lower than compaction velocity and/or greater than compaction trend density data on the crossplot (Figure 18). Since the overpressure zone plots as normal to higher velocity and lower density, it does not support fluid expansion overpressure generation. Density resistivity crossplots support this reasoning, but not as clearly or organized as the density velocity crossplots (Figure 54, Figure 55).

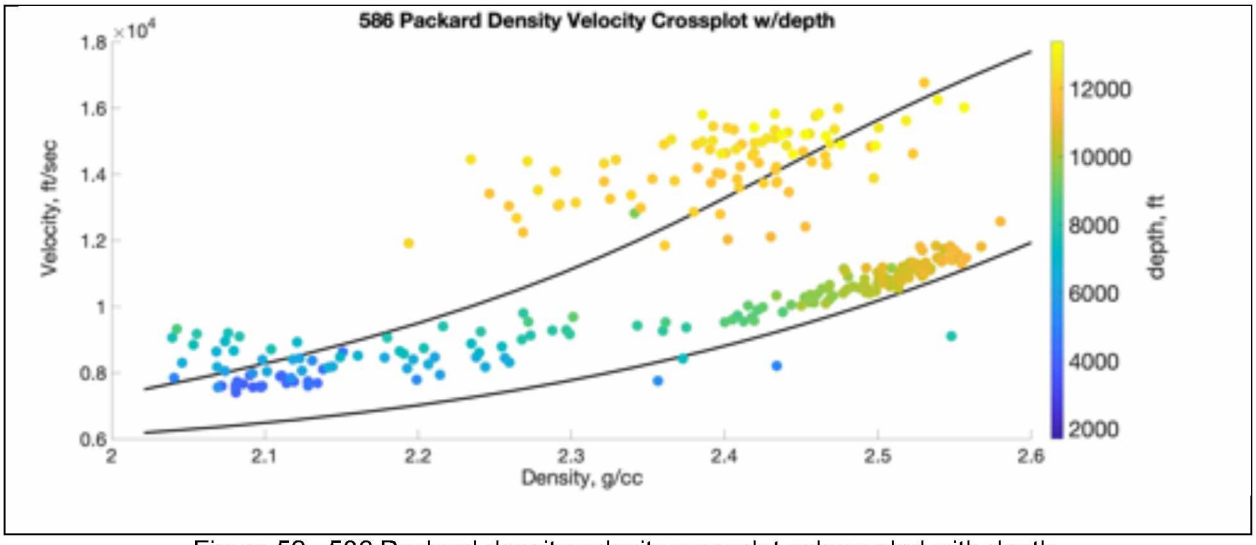

Figure 52. 586 Packard density velocity crossplot color coded with depth.

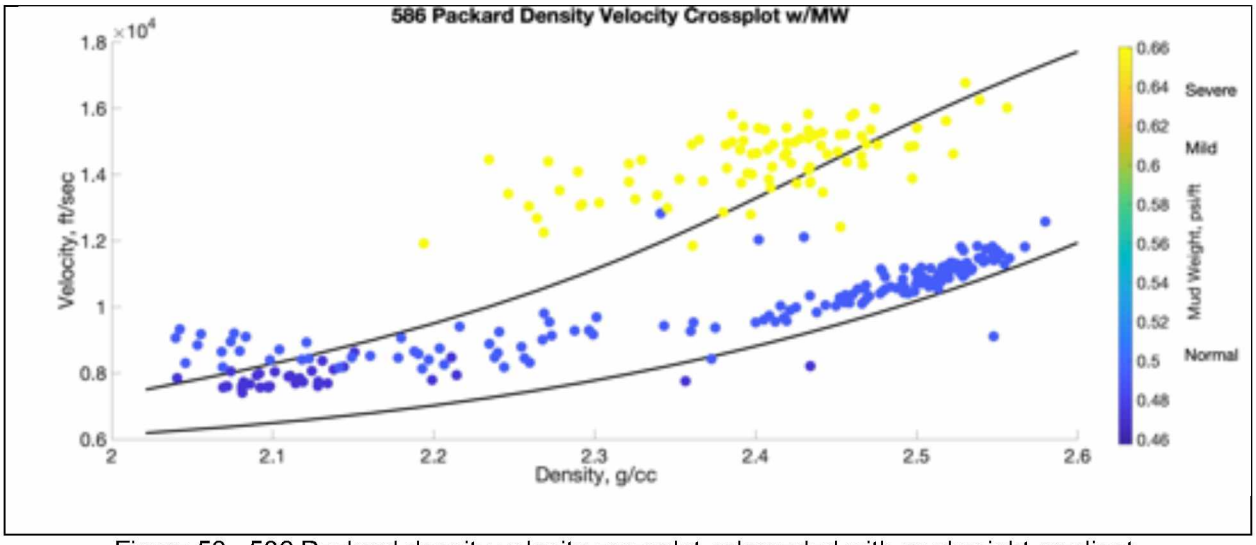

Figure 53. 586 Packard density velocity crossplot colorcoded with mudweight gradient.

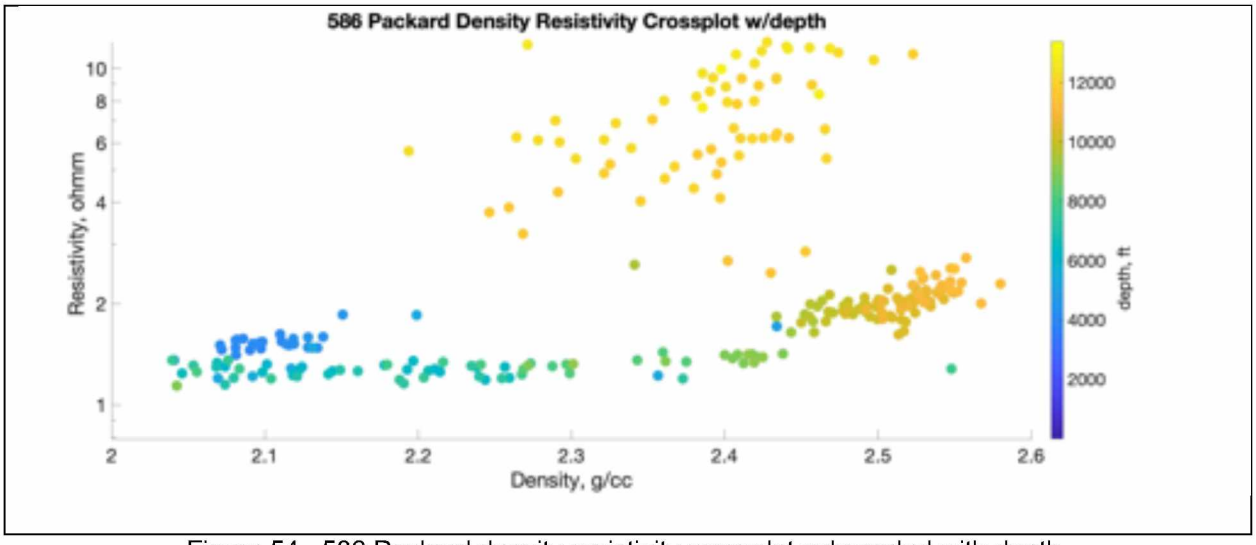

Figure 54. 586 Packard density resistivity crossplot colorcoded with depth.

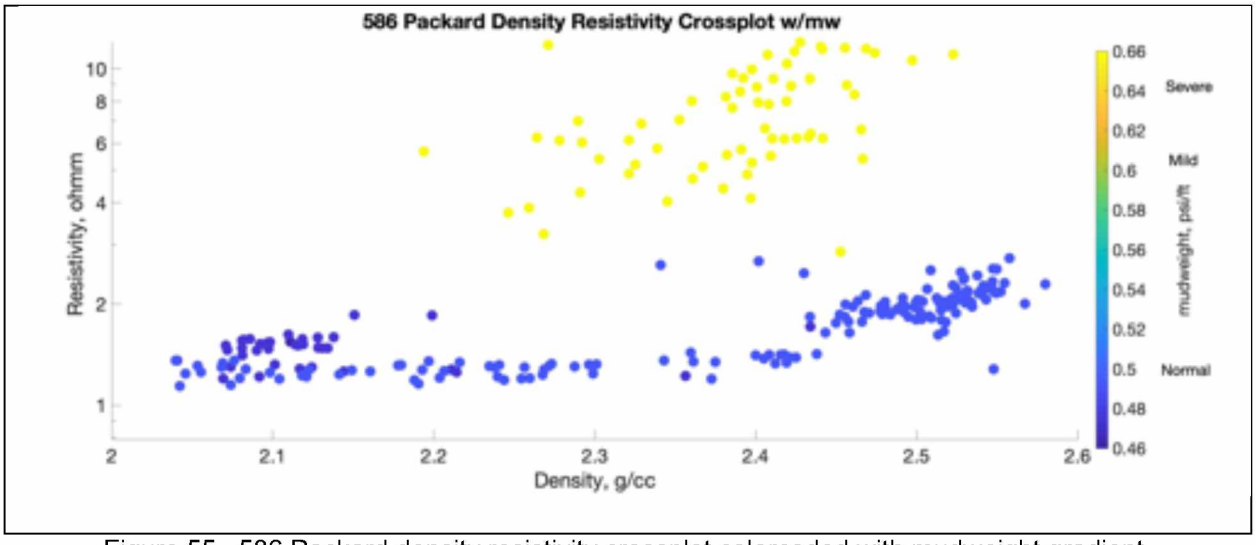

Figure 55. 586 Packard density resistivity crossplot colorcoded with mudweight gradient.

Well 599 Redwood 1 contains a zone of mild to severe overpressure at depths greater than 9,000 feet. The density velocity crossplots show that the overpressure zone is more scattered than in other wells; however, the overpressure zone still lies within the bounds of the normal compaction trend (Figure 56, Figure 57). The density resistivity crossplots don't show any significant trend (Figure 58, Figure 59). The lack of significant fluid expansion trends on the density velocity crossplot rules out fluid expansion mechanisms for overpressure generation (Figure 18). Since the data lies almost entirely within the compaction bounds and follows a compaction trend where velocity and density increase with depth and pressure, it is reasonable to conclude that disequilibrium compaction generates the overpressure in this well.

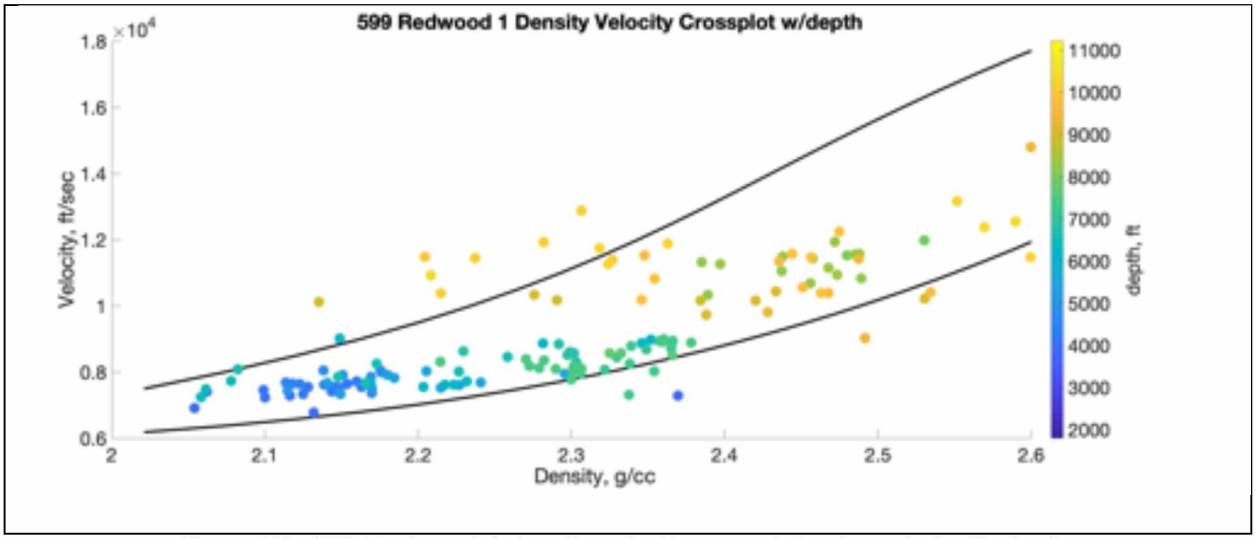

Figure 56. 599 Redwood 1 density velocity crossplot colorcoded with depth.

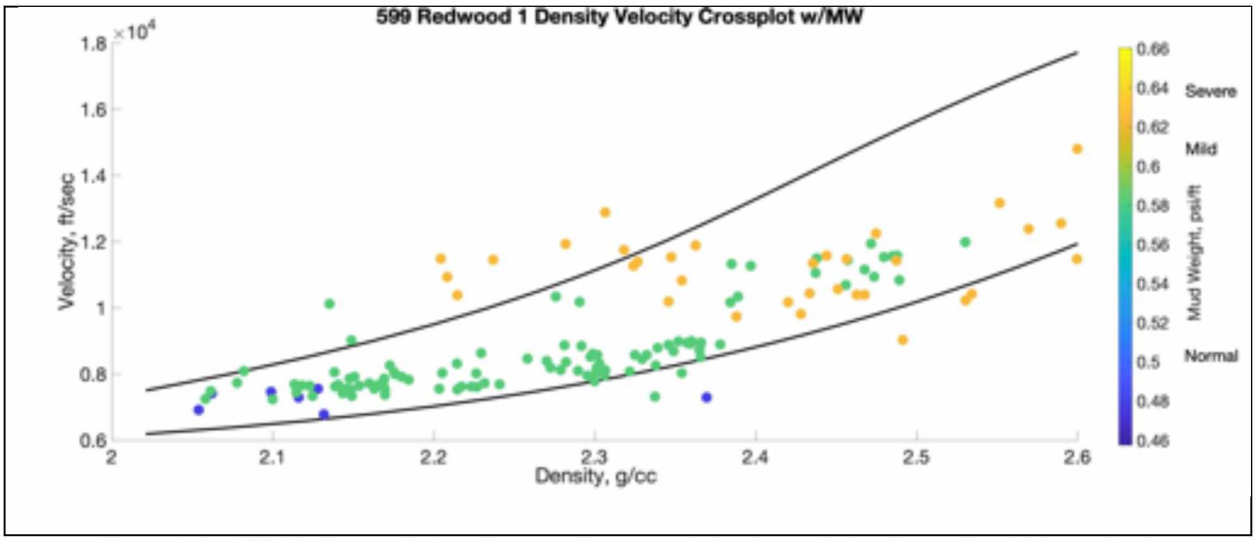

Figure 57. 599 Redwood 1 density velocity crossplot colorcoded with mudweight gradient.

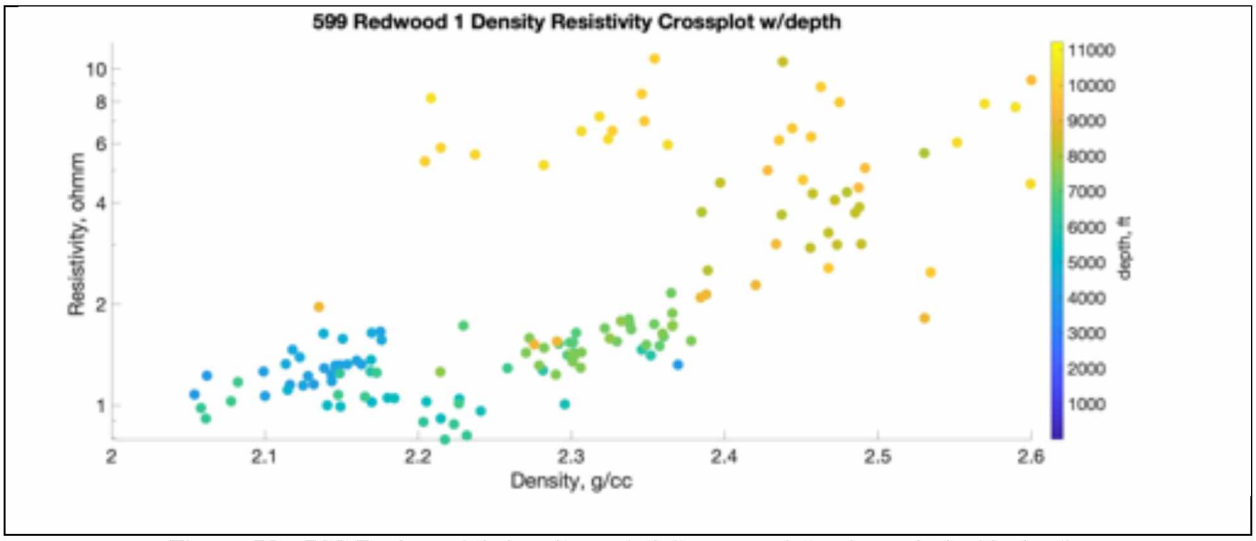

Figure 58. 599 Redwood 1 density resistivity crossplot colorcoded with depth.

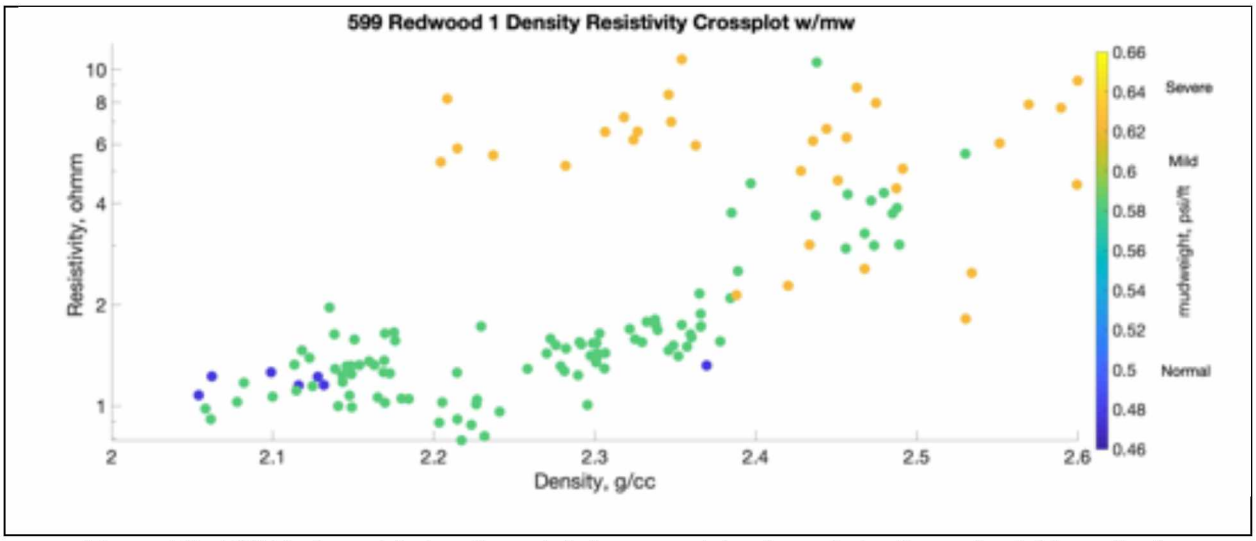

Figure 59. 599 Redwood 1 density resistivity crossplot colorcoded with mudweight gradient.

Well 719 Nancy exhibits mild overpressure at depths greater than 7,000 feet. The density velocity crossplots also show the data fitting entirely within bounds and following a normal compaction trend (Figure 60, Figure 61). The density resistivity crossplots are not as clear and are therefore not considered reliable to determine origins of overpressure (Figure 62, Figure 63). There is a lack of any characteristics of fluid expansion mechanisms from the density velocity crossplots (Figure 18). There is evidence of a slow or reversal trend on the velocity and density data, which is also indicative of disequilibrium compaction where pore fluid is unable to escape the pore space under increasing vertical stress. Therefore, disequilibrium compaction is most likely the primary mechanism or origin of overpressure generation in well 719 Nancy. The crossplots for the remaining non overpressured wells are listed in Appendix A.

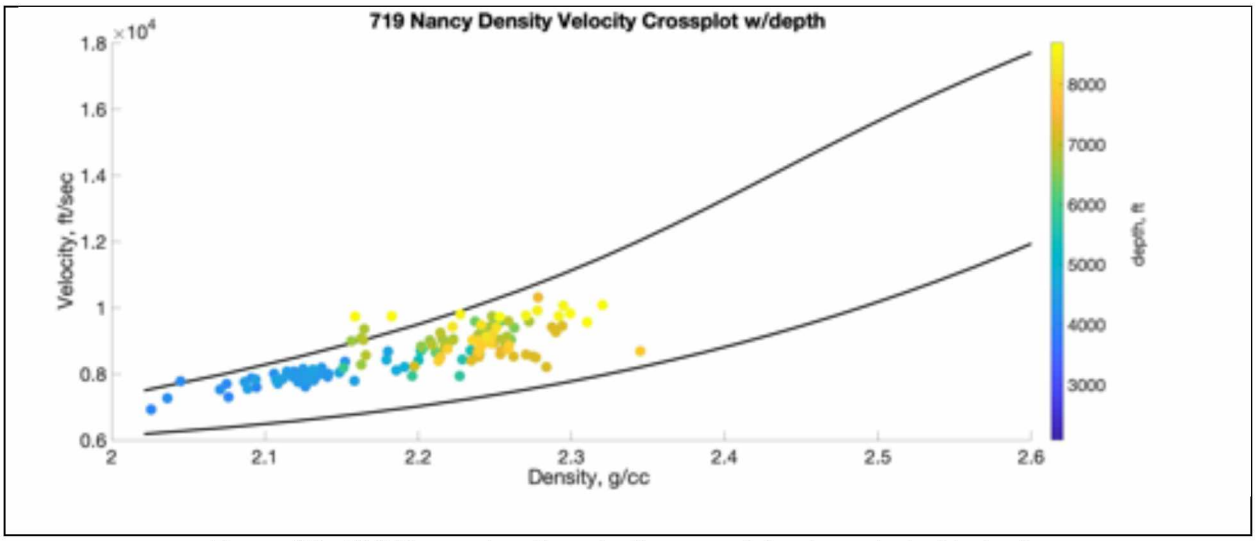

Figure 60. 719 Nancy density velocity crossplot colorcoded with depth.

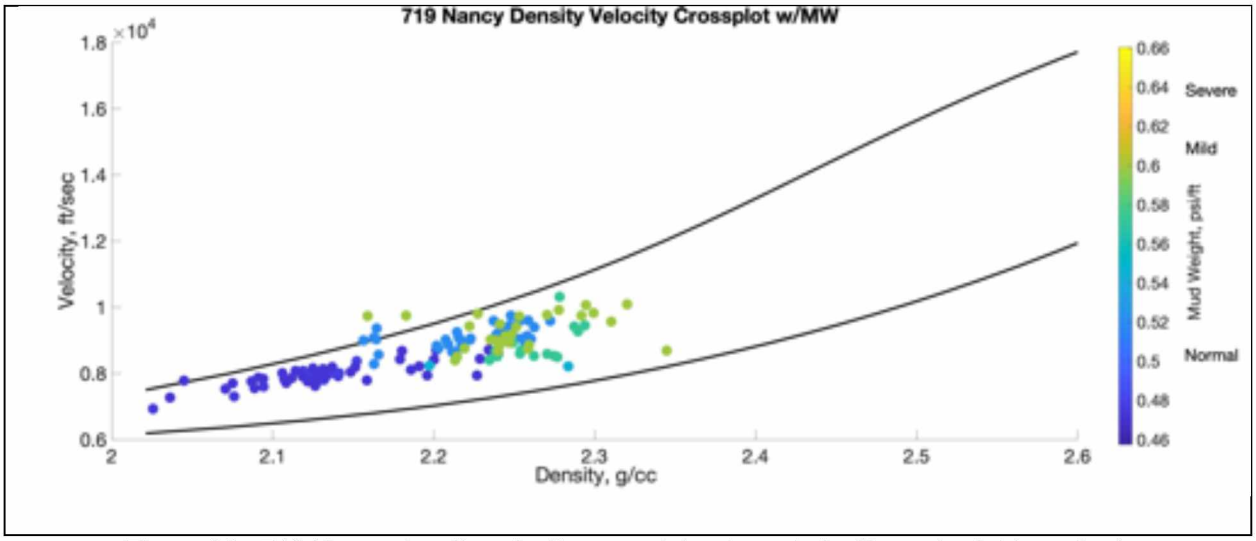

Figure 61. 719 Nancy density velocity crossplot colorcoded with mudweight gradient.

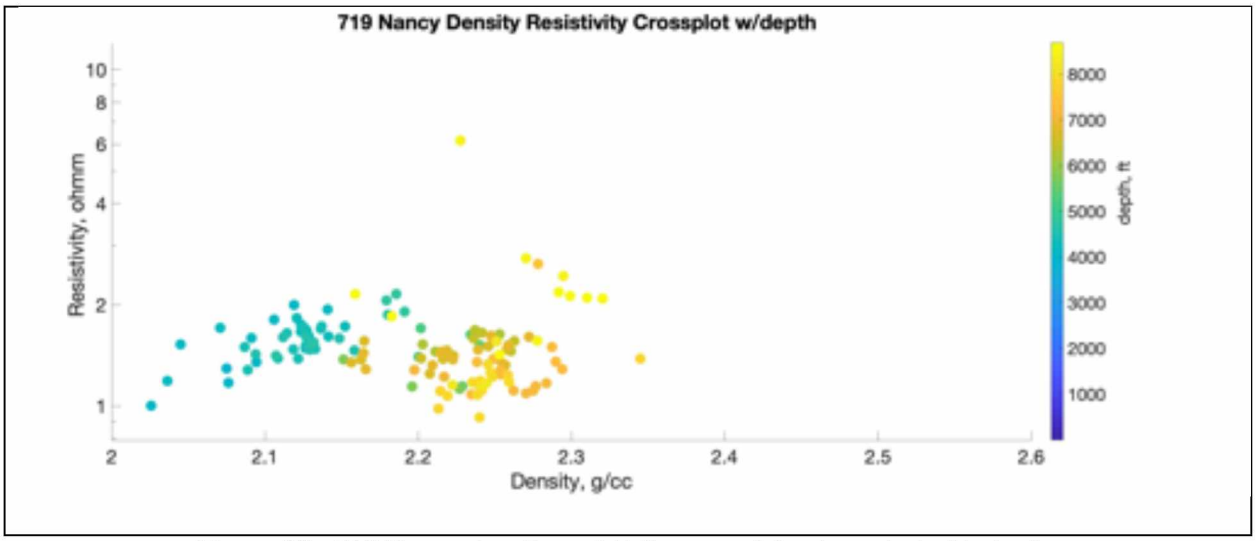

Figure 62. 719 Nancy density resistivity crossplot colorcoded with depth.

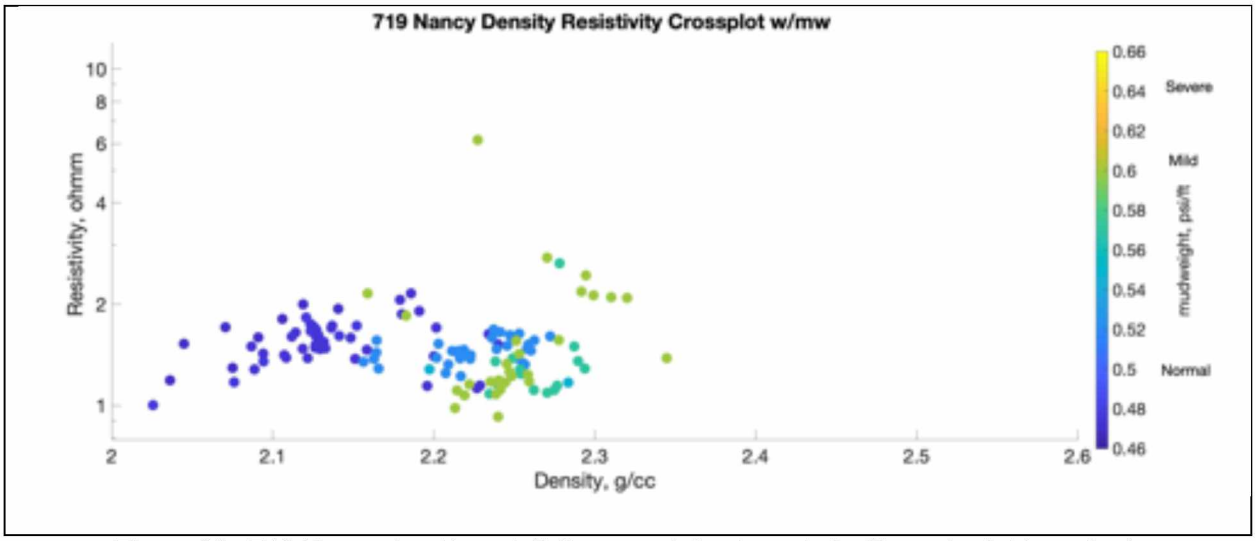

Figure 63. 719 Nancy density resistivity crossplot colorcoded with mudweight gradient.

Conclusion

For all exploratory wells with overpressure regions, the plots of vertical effective stress against sonic velocity show trends of normal compaction. The crossplots for the remaining non overpressured wells are listed in Appendix A. A deviation from normal

compaction, an identifying characteristic of fluid expansion overpressure generation, is not observed in any plots. Specifically, no marked changes in vertical effective stress or sonic velocity are evident outside of the expected compaction trend when the plots are organized for pressure and depth. Density velocity crossplots show a proportional decrease in sonic velocity with decrease in density (as a reversal trend on the loading zone) in regions where overpressure is observed. This proportional decrease is also characteristic of disequilibrium compaction. Fluid expansion mechanisms are not observed in the density velocity crossplots. Therefore, the Effective stress plots and Density velocity crossplots suggests an origin of overpressure from disequilibrium compaction

6. Pore Pressure Prediction in the Navarin Basin

Introduction

Pore pressure prediction can aide better understanding the origins of overpressure by further identifying the formations where overpressure can occur (Barron, Weakley et al. 1990, Alixant and Desbrandes 1991, Lesage, Hall et al. 1991, Yassir and Bell 1996). Hottman and Johnson (1965) developed one of the first methods of relating pore pressure to data from well log measurements (Hottmann and Johnson 1965, Hottman, Smith et al. 1979). They examined shales in the Texas and Louisiana gulf coast and determined that porosity decreased as depth increased. They obtained this trend from observing an increase in shale transit time measurements that increased incrementally with depth. This trend of decreasing porosity with depth was termed the normal compaction trend and has been a critical concept of overpressure characterization since (Hottmann and Johnson 1965, Hottman, Smith et al. 1979).

Fifteen years after the work of Hottman and Johnson, Gardner et al. (1974) examined the Texas and Louisiana gulf coast shale transit time data to develop a pore pressure prediction equation (Gardner, Gardner et al. 1974):

$$P_p = \sigma_v - \frac{(\sigma_{grad} - P_{hyd})(A - Bln\Delta t)^3}{Z^2}$$

Equation 12.

where P_p is pore pressure (psi); σ_{grad} is the overburden pressure gradient (psi/ft); P_{hyd} is the normal hydrostatic pressure gradient (psi/ft); Δt is the shale transit time (μs/ft); Z is depth (feet); and A, B are constants where A=82,776 and B=15,695 (Gardner, Gardner et al. 1974, Zhang 2011, Zhang 2013).

Methodology

Eaton Method

Eaton (1974) later used resistivity well log data to predict pore pressure with the following equation:

$$P_p = \sigma_{grad} - (\sigma_{grad} - P_{hyd})\left(\frac{R}{R_n}\right)^n$$

Equation 13.

where P_p is pore pressure gradient (psi/ft); σ_{grad} is overburden pressure gradient (psi/ft); P_{hyd} is normal hydrostatic pressure gradient (psi/ft); R is the well log measured resistivity (ohmm); R_n is the normal compaction trend derived resistivity (ohmm); and n is the exponent that can be varied from 0 to 2 (Eaton 1969, Eaton 1972, Eaton 1972, Eaton 1975, Zhang 2013). Eaton (1974) also determined a pore pressure prediction equation similar to the Gardner et al.'s (1974) equation, but without the constant values:

$$P_p = \sigma_{grad} - (\sigma_{grad} - P_{hyd})\left(\frac{t}{t_n}\right)^n$$

Equation 14.

where P_p is pore pressure gradient (psi/ft); σ_{grad} is overburden pressure gradient (psi/ft); P_{hyd} is normal hydrostatic pressure gradient (psi/ft); t is the well log measured transit time (μs/ft); t_n is the normal compaction trend derived resistivity (μs/ft); and n is the Eaton exponent that has been used in different formations and has been found to vary depending on the type of target formation.(Eaton 1969, Eaton 1972, Eaton 1972, Eaton 1975, Zhang 2013). Tingay (2009) found that using an Eaton exponent of 3 was accurate in predicting pore pressure where the source of overpressure was disequilibrium compaction (Tingay, Hillis et al. 2009). Overpressure in the Carnarvon Basin, Western Australia attributed to disequilibrium compaction was also accurately predicted with an Eaton exponent of 3 (van Ruth, Hillis et al. 2004). Using an Eaton exponent of 6.5 was accurate in predicting pore pressure in formations where the origin of overpressure was vertical transfer (Tingay, Hillis et al. 2009). An Eaton exponent of 6 accurately predicted pore pressure in formations where overpressure was attributed to fluid expansion in the Carnarvon Basin (van Ruth, Hillis et al. 2004).

The Bowers Method

The Bowers method used both a virgin loading curve and an unloading curve to account for overpressure from disequilibrium compaction and fluid expansion (Bowers 1995, Figure 64). When the vertical effective stress data follow the compaction trend, then the virgin curve equation is used to predict the pore pressure (Bowers 1994, Bowers 1995, Bowers 2001, Bowers 2002, Bruce and Bowers 2002). When the vertical effective stress data show a deviation or reversal outside the normal compaction trend, the unloading curve equation is used (Bowers 1994, Bowers 1995, Bowers 2001, Bowers 2002, Bruce and Bowers 2002).

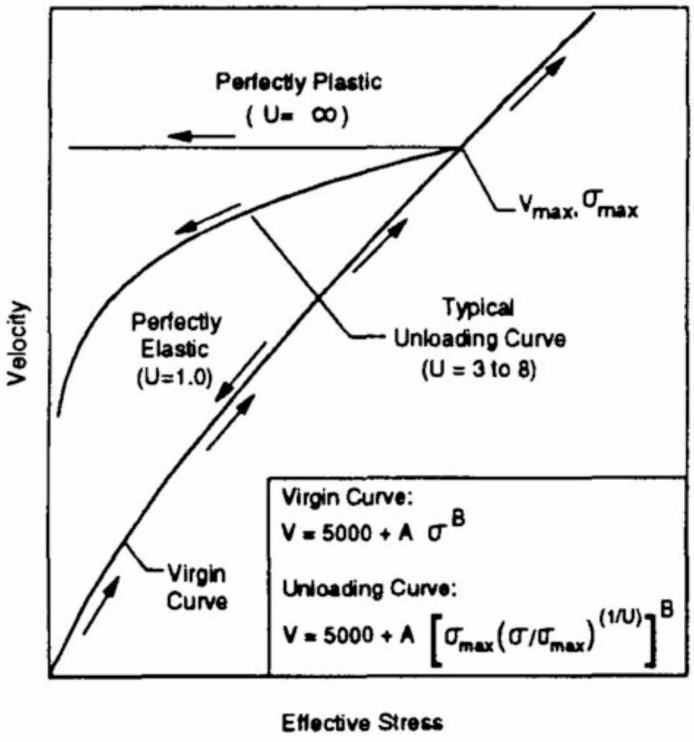

Figure 64. Representation of the virgin loading curve and unloading curve from vertical effective stress vs. velocity graph (Bowers, 1994).

The virgin curve equation is determined from plotting the vertical effective stress against the velocity data and determining curve fitting parameters from the normal compaction trend given in the following equation (Bowers, 1995):

$$V = 5000 + A{\sigma_{ve}}^B$$

Equation 15.

where V is the sonic velocity (ft/sec); A and B are parameters calculated from offset velocity vs. effective stress plots; 5000 is the surface velocity (ft/sec); and σ_{ve} is the vertical effective stress calculated from measured pore pressure and overburden stress

data (psi). The relationship between vertical effective stress, pore pressure, and overburden stress is used to manipulate Equation 15 to obtain the following equation (Bowers, 1994):

$$P_p = \sigma_{ov} - \left(\frac{V - 5000}{A}\right)^{1/B}$$

Equation 16.

where V is the sonic velocity (ft/sec); A and B are parameters calculated from offset velocity vs. effective stress plots; 5000 is the surface velocity (ft/sec); and σ_{ov} is the overburden stress (psi). The unloading equation is similar to the virgin curve equation with the addition of the maximum vertical effective stress and velocity before the reversal occurs (Bowers, 1994).

$$V = 5000 + A\left(\sigma_{max}(\sigma_{ve}/\sigma_{max})^{1/U}\right)^{B}$$

Equation 17.

where V is the sonic velocity (ft/sec); A and B are parameters calculated from offset velocity vs. effective stress plots; 5000 is the surface velocity (ft/sec); σ_{ve} is the vertical effective stress calculated from measured pore pressure and overburden stress data (psi); σ_{max} is the maximum vertical effective stress on the virgin curve before the reversal and deviation to the unloading curve; and U is a third parameter for the elasticity of the unloading curve that usually ranges between 3 and 8 (Bowers 2002). The unloading curve equation is then manipulated using the relationship between

overburden, pore pressure, and vertical stress to give the following equation for pore pressure prediction from the unloading curve, where all parameters are the same previous equation (Bowers 1994).

$$P_p = \sigma_{ov} - \left(\frac{V - 5000}{A}\right)^{U/B} (\sigma_{max})^{1-U}$$

Equation 18.

Normal Compaction Trend

Previous literature involving pore pressure prediction determines that in general the Bowers method is fairly accurate in predicting pore pressure with some tendency to overestimation of pore pressure (Sayers, Johnson et al. 2000, Sayers, Hooyman et al. 2002, Sayers and Woodward 2002). Although the Navarin Basin data does not include reliable direct pore pressure measurements as required by the Bowers method, an attempt is made to utilize the method by calculating the vertical effective stress from normal hydrostatic pressure for the virgin curve.

A normal compaction trend needs to be established for the Navarin Basin in order to utilize the Eaton (1974) and Bowers (1995) methods as shale formations have been shown to follow a compaction trend (Smith 1973, Dutta 1983). Figure 65 shows the normal compaction trend line for sonic velocity with depth. Although it is possible to use a straight line to fit the sonic velocity data, an exponential trend is routine to account for maximum and minimum velocity values that do not follow a linear trend (Wallace 1965, Bowers 1995, Zhang 2013).

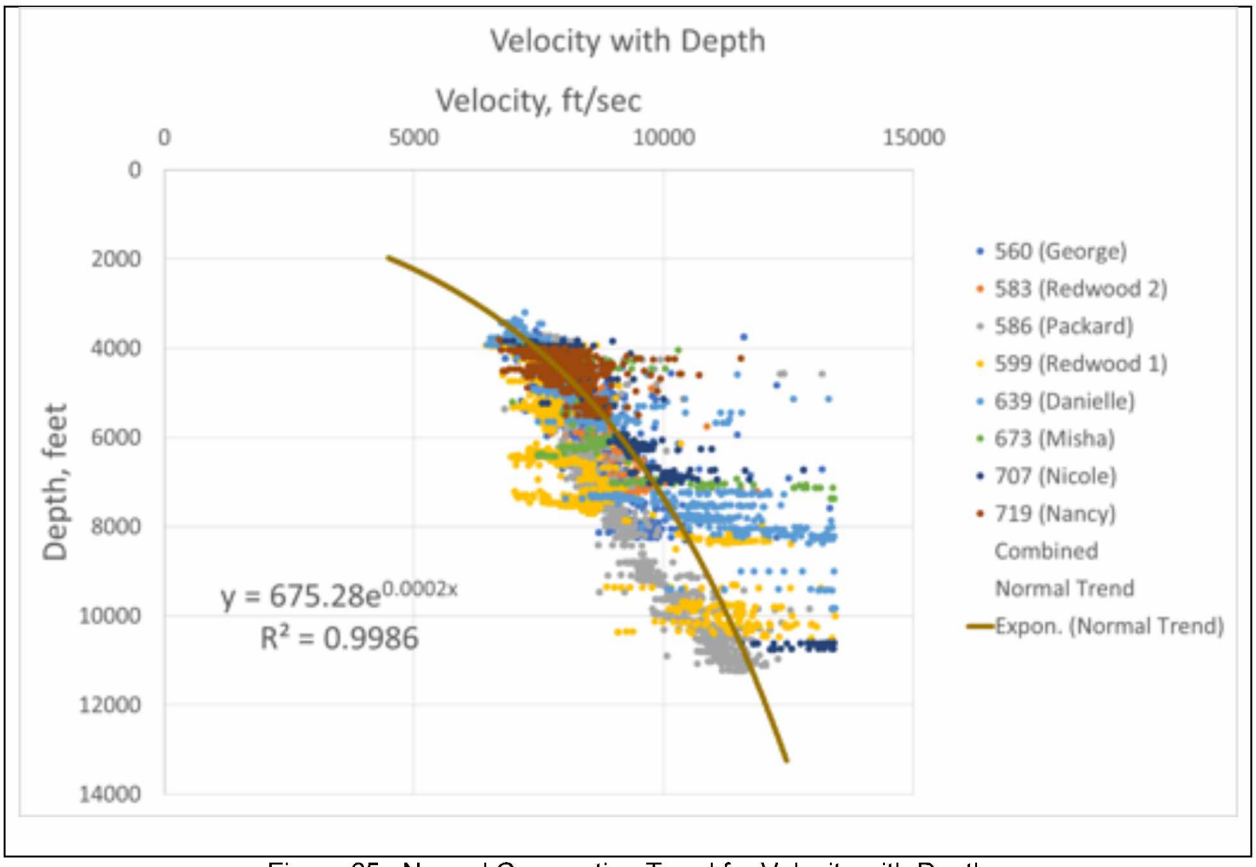

Figure 65. Normal Compaction Trend for Velocity with Depth

Figure 66 shows an attempt to find a normal compaction trend for the resistivity data with depth. The normal compaction trend does not adequately fit the resistivity data as there is too much variation between the different exploratory wells.

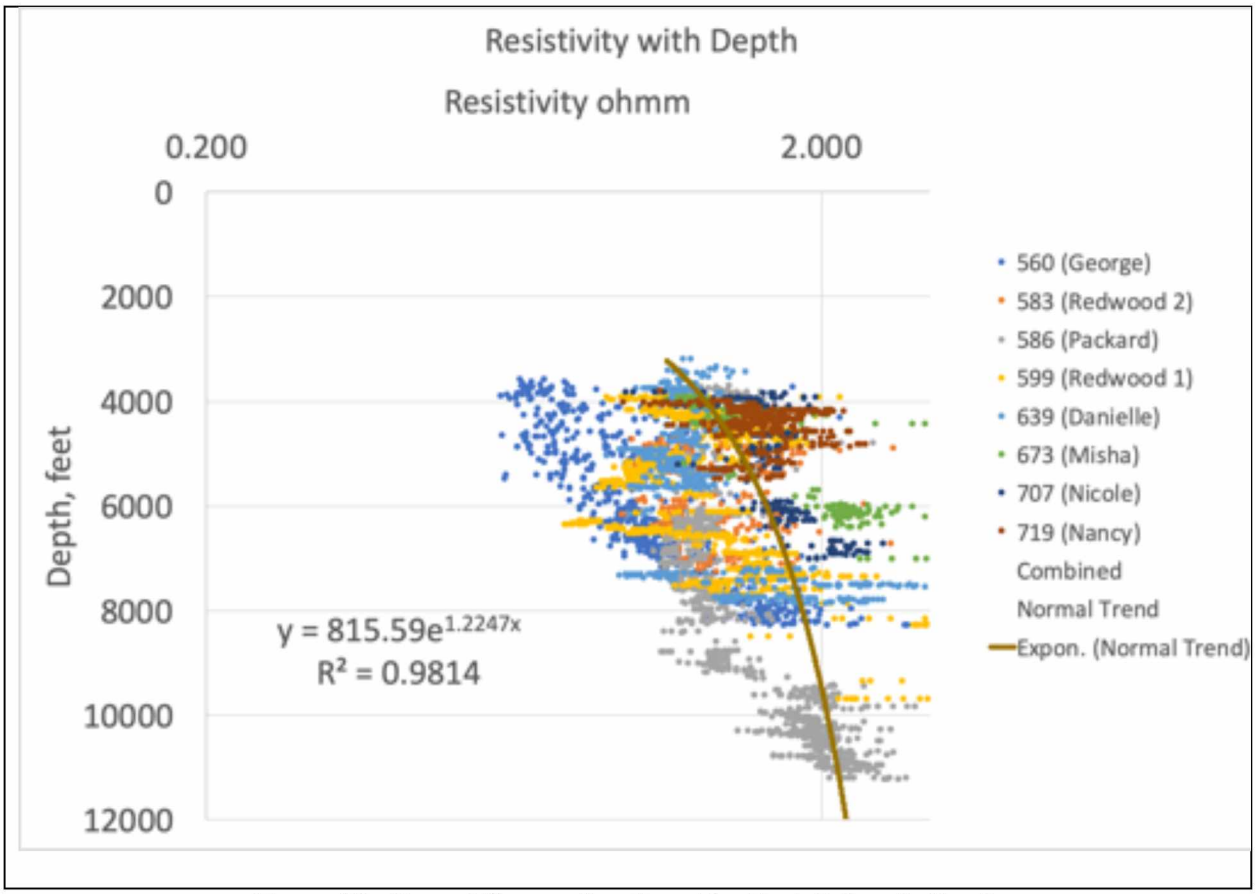

Figure 66. Normal Compaction Trend for Resistivity with Depth

Figure 67 shows the fit of a normal compaction trend for the bulk density well data with depth. The bulk density normal compaction trend is utilized for pore pressure prediction when the sonic velocity normal compaction trend differs from the well log data for an individual case. For the Navarin Basin exploratory wells, the sonic velocity normal compaction trend was shown to be an adequate prediction tool for the Eaton and Bowers Methods.

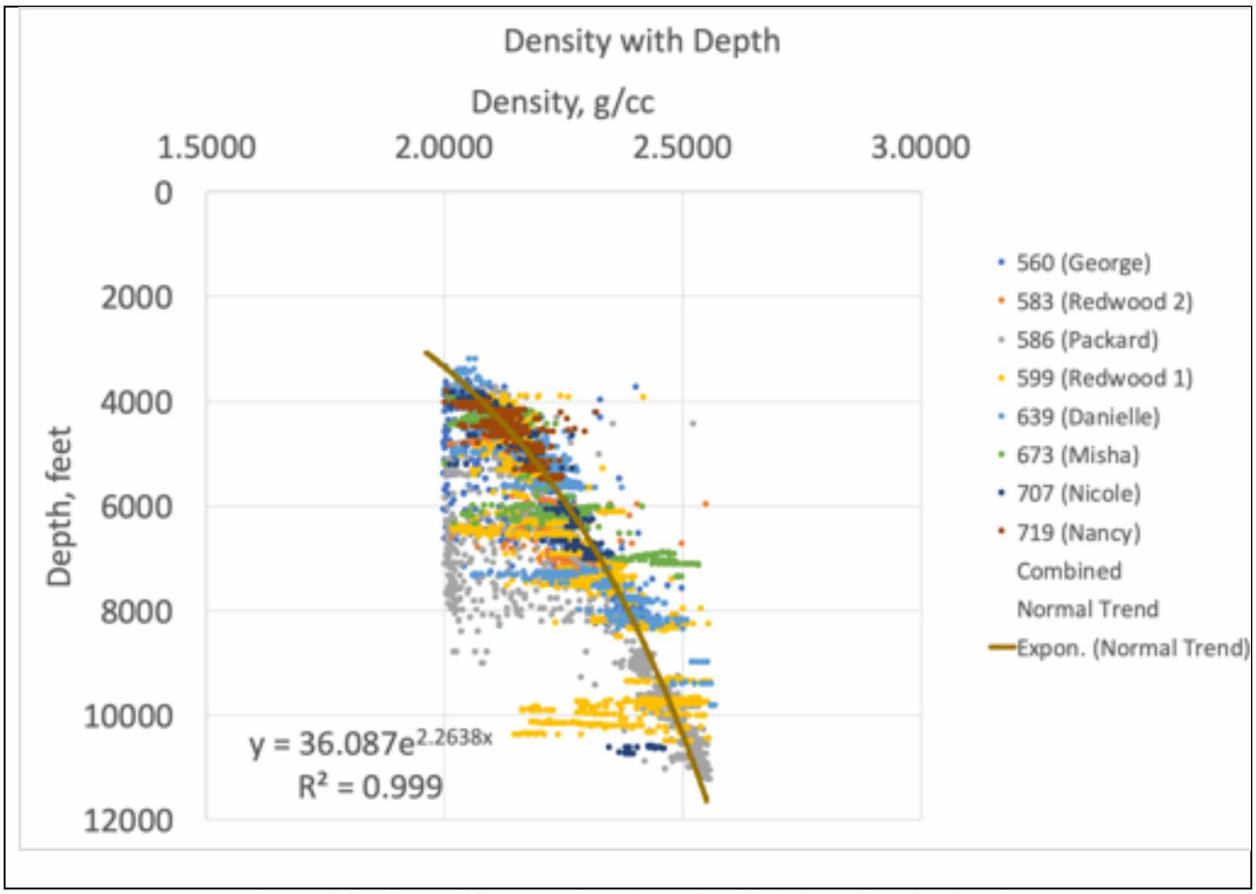

Figure 67. Normal Compaction Trend for Bulk Density with Depth

Results and Discussion

The pore pressure prediction results for well 583 Redwood 2 for the Eaton and Bowers methods are shown in Figure 68. The normal compaction trend line from the sonic velocity data (Figure 65) was used to calculate normal velocity values since the curve accurately fits the sonic velocity data for well 583 Redwood 2. Figure 68 shows an increase in pore pressure from 8,000 to 12,000 feet which is located at the Eocene age shale target formation and deeper formations where overpressure is expected. The Bowers method and Eaton method predict pore pressure increases at similar depths,

but the Bowers method predicts a higher pore pressure than the Eaton method. These results support the existence of overpressure at the target formation.

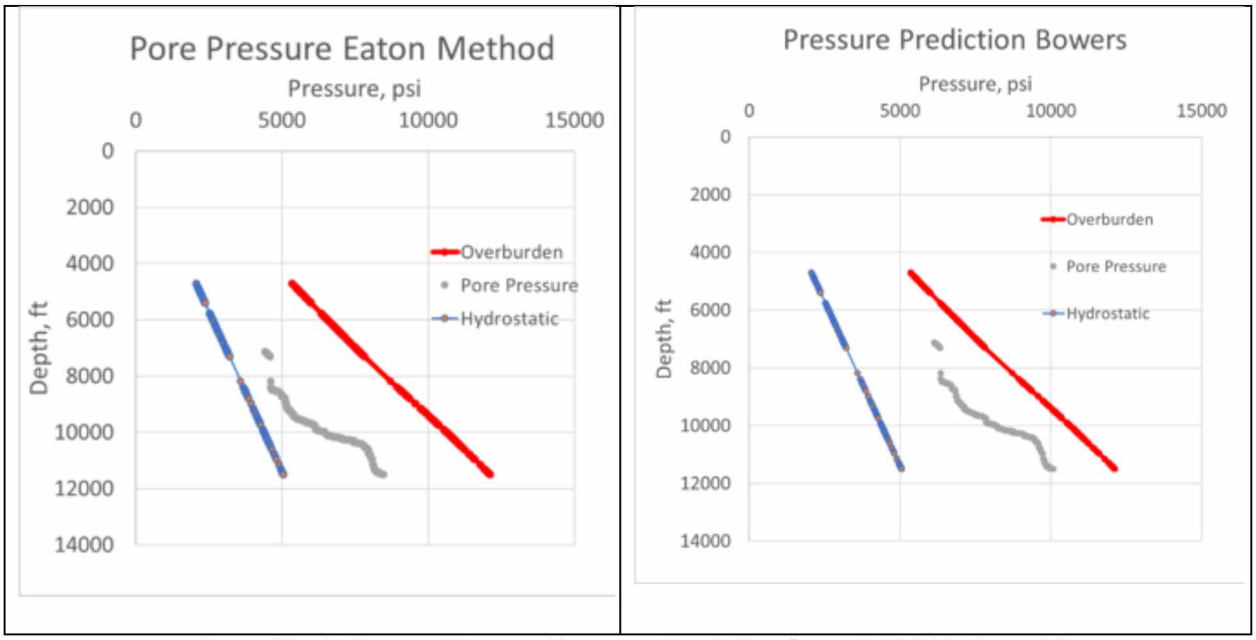

Figure 68. Eaton and Bowers Pressure Prediction for well 583 Redwood 2

Well 586 Packard pore pressure was also predicted using the normal compaction trend form sonic velocity data for the Navarin Basin (Figure 65). The pore pressure predictions from Eaton and Bowers methods show an increase in pore pressure at the expected depth of the target shale formation for the Eocene age at depths from approximately 7,000 to 9,000 feet. The Bowers method and Eaton method predict pore pressure increases at similar depths, but the Bowers method predicts a higher pore pressure than the Eaton method (Figure 69). These results support the existence of overpressure at the target formation.

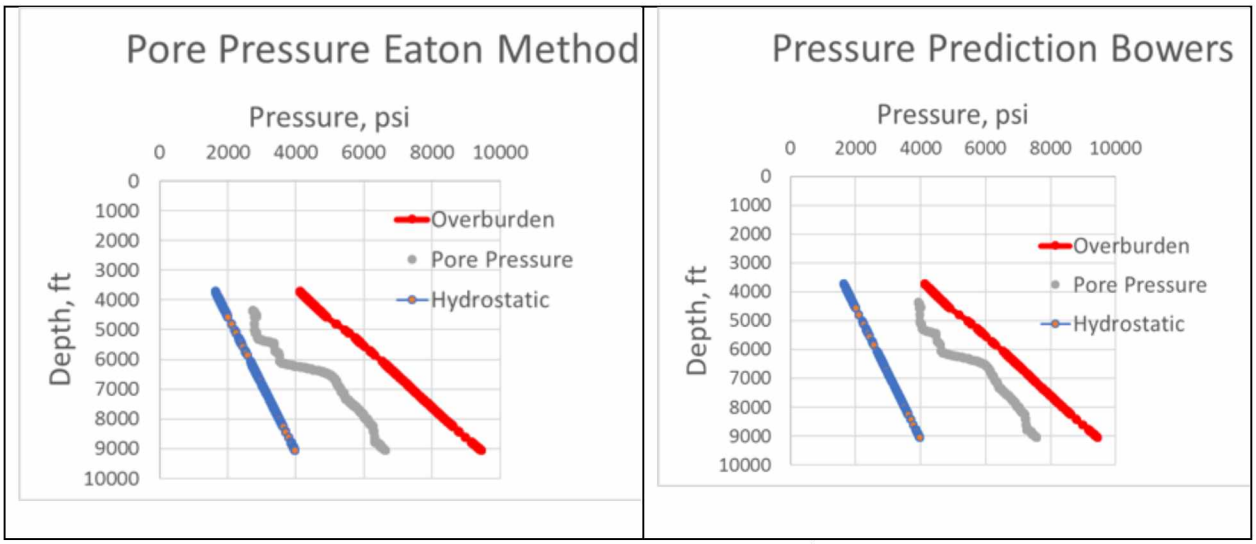

Figure 69. Eaton and Bowers Pressure Prediction for well 586 Packard

Well 599 Redwood 1 pore pressure was utilized using the normal compaction trend from sonic velocity data (Figure 65). The pore pressure is likely over predicted by the Bowers method (Figure 70) – as possibility explained in the methodology. However, the Eaton method shows an increase in pore pressure from 6,000 to 8,000 feet, which is the expected depth of the target shale formation. The Bowers method and Eaton method predict pore pressure increases at similar depths, but the Bowers method predicts a higher pore pressure than the Eaton method. These results support the existence of overpressure at the target formation.

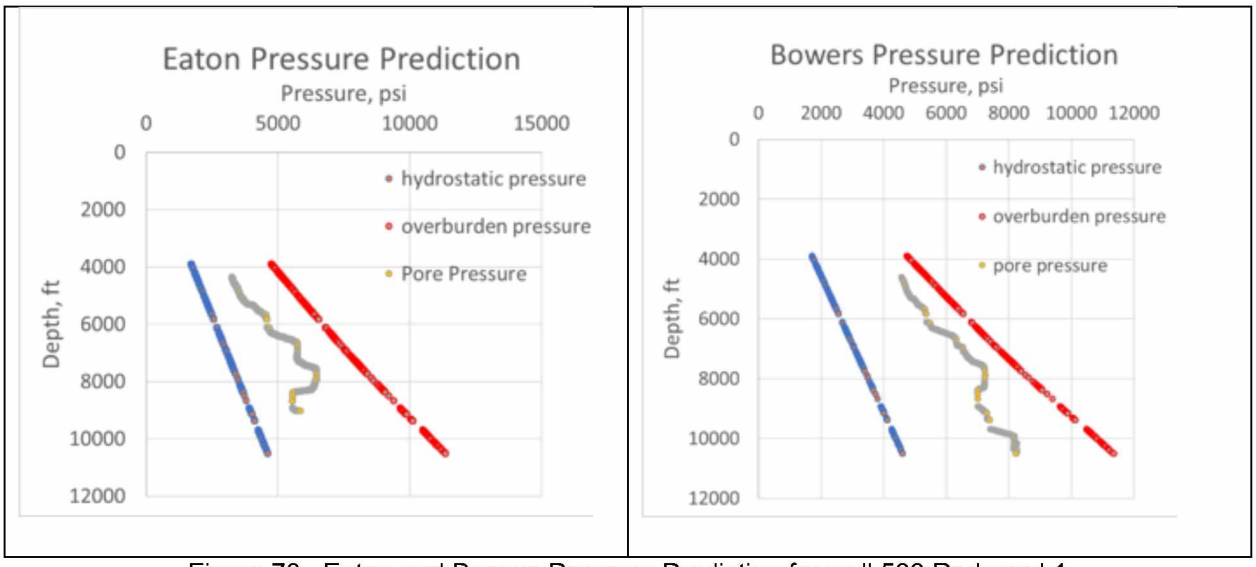

Figure 70. Eaton and Bowers Pressure Prediction for well 599 Redwood 1

The pore pressure for well 719 Nancy was calculated using the normal compaction trend for sonic velocity (Figure 65) and the Bowers and Eaton Methods. Both methods showed an increase in pore pressure between 7,000 and 9,000 feet. Pressure increases at around the depth of the target shale formation (Figure 71). The Bowers method and Eaton method predict pore pressure increases at similar depths, but the Bowers method predicts a higher pore pressure than the Eaton method. These results support the existence of overpressure at the target formation.

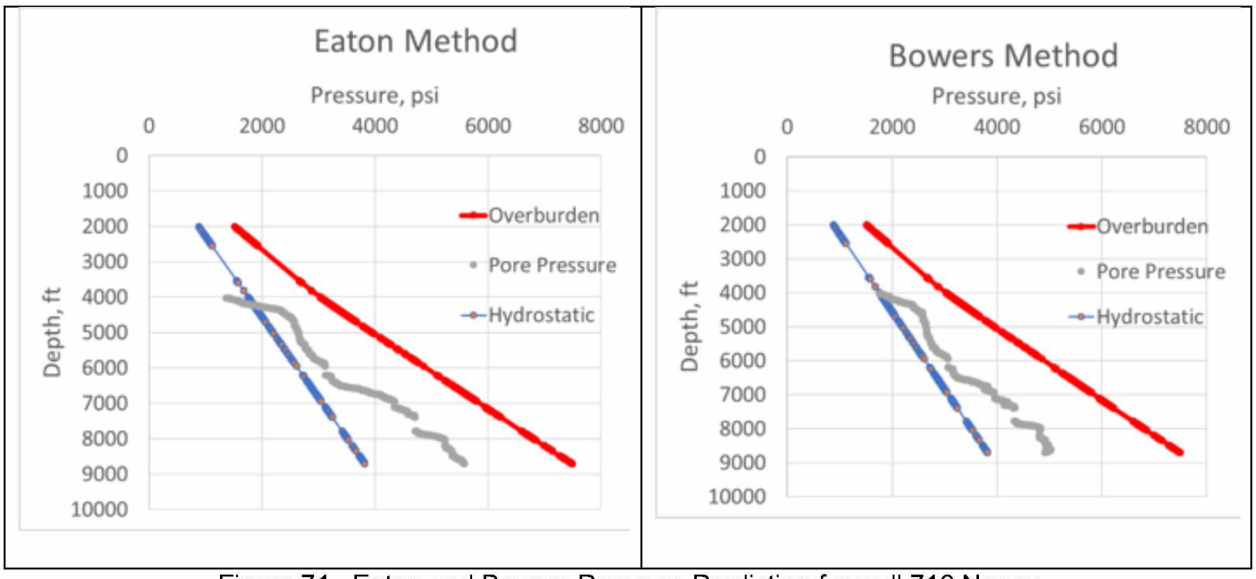

Figure 71. Eaton and Bowers Pressure Prediction for well 719 Nancy

Conclusion

The pore pressures were predicted for the eight exploratory wells of the Navarin Basin using normal compaction trends over the entire basin. The normal compaction trends were established using sonic velocity, resistivity, and bulk density data. In all cases, the sonic velocity compaction trend produced the most easily observable results in agreement with established literature practices explained in the methodology. The pore pressure prediction calculations for the overpressure wells showed an increase in pore pressure from both Eaton and Bowers methods at around the expected depth of the Eocene age target shale formation which shows the effectiveness of these pore pressure predictions methods to support the existence and region of overpressure. The pore pressure prediction from the Bowers method was universally higher than the pore pressure predicted from the Eaton method. Overall, the two methods were effective in

predicting the overpressure in the Eocene target formation identified in previous chapters. The pore pressure prediction results for the remaining exploratory wells are included in Appendix B.

7. Conclusions and Recommendations

Data from 8 exploratory wells of the Navarin Basin are studied in this project. Well log information was obtained from the Alaska BOEM and digitized and organized using photo editing and Microsoft Excel software to obtain stratigraphic and other geologic information in order to construct the characteristics of the Navarin Basin such as the burial rates, effective stress, and tectonic activity. These results support a conclusion that overpressure in the Navarin Basin was primarily generated through disequilibrium compaction.

The depth of observed overpressure combined with the stratigraphy information led to identification of the target formation as the shale formation from the Eocene age. The burial rate of formations above the target formation in the Navarin Basin can give support to the origin of overpressure. Since disequilibrium compaction is caused by burial rates that exceed the rate at which excess pore fluid is able to escape a formation, a rapid burial rate could lend evidence to a disequilibrium compaction origin of overpressure. In the Navarin Basin, a pattern was discovered where the burial rates were greater in the overlying younger formations and lower in the deeper older formations. Therefore, the calculated burial rates from the Navarin Basin wells support an origin of overpressure from disequilibrium compaction.

The results from the vertical effective stress plots for the Navarin Basin show sonic velocity and vertical effective stress relationships correlating within a normal compaction trend. All wells show no deviation from the normal compaction trend on the vertical

effective stress plots. Therefore, a disequilibrium compaction origin of overpressure is supported by this method.

The density velocity crossplots for the Navarin Basin exploratory wells show no evidence of fluid expansion relationships. The exploratory wells exhibited no deviation from the loading zone (decreasing sonic velocity or increasing bulk density with respect to the loading zone). Absence of fluid expansion mechanisms in the density velocity crossplots for the Navarin Basin supports the mechanism of overpressure as disequilibrium compaction.

Pore pressure prediction methods were used to characterize the overpressure in the Navarin Basin. Although the predictions could not be compared to direct pore pressure measurements due to unavailability of direct pore pressure measurements, the predictions obtained from the Eaton and Bowers methods showed an increase in pore pressure at the depth of the target Eocene shale formation for the eight exploratory wells.

The target formation is more shallow and of greater thickness around the region of overpressure. This thicker target formation in the region of the overpressured wells supports the idea of active syncline folding. Active syncline folding could contribute to rapid burial rates and suggest overpressure generation from disequilibrium compaction. Further study is needed to quantify the tectonic contribution to overpressure such as more direct pore pressure measurement and more extensive tectonic examination.

Although the tectonic characteristics and the pore pressure predictions lend support to the existence of overpressure in the target formation, direct pore pressure

measurements (if obtained) and tectonic information could support the location of the target formation and any error in pore pressure prediction values. Additional tectonic study in the Navarin Basin could support the conclusions based on the calculated burial rates and the accompanying active syncline folding. Other possible tectonic contributions to overpressure such as faulting may be discovered with further investigation.

List of References

Alixant, J.-L. and R. Desbrandes (1991). "Explicit Pore-Pressure Evaluation: Concept and Application." SPE Drilling Engineering **6**(03): 182-188.

Athy, L. F. (1930). "Density, porosity, and compaction of sedimentary rocks." AAPG Bulletin **14**: 1-22.

Atwater, T. and J. Stock (2010). "Pacific-North America Plate Tectonics." International Geology Review **40**(5).

Barker, C. (1972). "Aquathermal pressuring: role of temperature in development of abnormal pressure zone." AAPG Bulletin **56**: 2068-2071.

Barron, J. G., et al. (1990). Pore Pressure Analysis Indicates Abnormal Pressure as Reason for Shale Instability in Offshore California Field. SPE/IADC Drilling Conference. Houston, Texas, Society of Petroleum Engineers: 7.

Bethke, C. M. (1986). "Inverse hydrologic analysis of the distribution and origin of Gulf Coast type overpressure zones." Journal of Geophysical Research **91**: 6535-6545.

Bour, O. (1994). "Numerical modelling of abnormal fluid pressures in the Navarin Basin, Bering Sea." Marine and Petroleum Geology **11**(4): 491-500.

Bowers, G. (1994). Pore Pressure Estimation From Velocity Data: Accounting for Overpressure Mechanisms Besides Undercompaction. SPE Drilling Conference. Dallas, Texas.

Bowers, G. (2001). Determining an Appropriate Pore-Pressure Estimation Strategy. Offshore Technology Conference. Houston, Texas.

Bowers, G. L. (1995). "Pore Pressure Estimation From Velocity Data: Accounting for Overpressure Mechanisms Besides Undercompaction." SPE Drilling & Completion **10**(02): 89-95.

Bowers, G. L. (2002). "Detecting high overpressure." The Leading Edge **21**(2): 174-177.

Brocher, T. (2005). "Empirical Relations between Elastic Wavespeeds and Density in the Earth's Crust." Bulletin of the Seismological Society of America **95**: 2081-2092.

Bruce, B. and G. Bowers (2002). "Pore Pressure Terminology." The Leading Edge: 170-173.

Burley, S., et al. (1989). "Timing diagenesis in the Tartan Reservoir." Marine and Petroleum Geology **6**: 98-120.

Chapman, R. (1980). "Mechanical versus thermal cause of abnormally high pore pressure in shales." AAPG Bulletin **64**(12): 2179-2183.

Chenevert, M. E. and A. K. Sharma (1993). "Permeability and Effective Pore Pressure of Shales." SPE Drilling & Completion **8**(01): 28-34.

Chilingar, G. V. (2002). Origin and prediction of abnormal formation pressures. Amsterdam, Elsevier.

Christensen, N. and W. Mooney (1995). "Seismic velocity structure and composition of the continental crust." Journal of Geophysical Research **100**: 9761-9788.

Core Laboratories, I. (1987). Core Analysis Report. Dallas, Texas.

DeMets, C. and R. G. Gordon (1990). "Current Plate Motions." Geophysical Journal International **101**(2).

Dutta, N. C. (1983). Shale Compaction And Abnormal Pore- Pressures: A Model of Geopressures In the Gulf Coast Basin. 1983 SEG Annual Meeting. Las Vegas, Nevada, Society of Exploration Geophysicists**:** 3.
No preview is available for this paper.

Dutta, N. C. (2001). "Deepwater geohazard prediction using prestack inversion of large offset p-wave data and rock model." The Leading Edge **Feb 2002**: 193-198.

Dutta, N. C. (2002). "Geopressure prediction using seismic data." Geophysics **67**: 2012-2041.

Eaton, B. (1972). "The Effect of Overburden Stress on Geopressure Prediction from Well Logs." Petroleum Technology **August 1972**.

Eaton, B. (1975). The equation for Geopressure Prediction from Well Logs, Society of Petroleum Engineers.

Eaton, B. A. (1969). "Fracture Gradient Prediction and Its Application in Oilfield Operations." Journal of Petroleum Technology **21**(10): 1353-1360.

Eaton, B. A. (1972). "The Effect of Overburden Stress on Geopressure Prediction from Well Logs." Journal of Petroleum Technology **24**(08): 929-934.

Elowe, K. E. and K. W. Sherwood (2017). Abnormal Formation Pressure in the Chukchi Shelf, Alaska. 51st U.S. Rock Mechanics/Geomechanics Symposium. San Francisco, California, USA, American Rock Mechanics Association**:** 13.

Fall, A., et al. (2012). "Testing the basin-centered gas accumulation model using fluid inclusion observations: Southern Piceance Basin, Colorado." AAPG Bulletin **96**: 2297-2318.

Fertl, W. H. and G. V. Chilingar (1977). "Importance of Abnormal Formation Pressures." Journal of Petroleum Technology **29**: 347-354.

Gardner, G., et al. (1974). "Formation Velocity and Density." Society of exploration geophysicists **39**: 770-780.

Godfrey, N., et al. (1997). "Ophiolitic basement to the Great Valley forearc basin, california, from seismic and gravity data." GSA Bulletin **108**: 1536-1562.

Goulty, N. and A. Ramdhan (2011). "Chemical compaction of mudrocks in the presence of overpressure." Petroleum Geoscience **18**: 471-479.

Griffin, D. G. and D. A. Bazer (1969). "A Comparison of Methods for Calculating Pore Pressures and Fracture Gradients from Shale Density Measurements Using the Computer." Journal of Petroleum Technology **21**(11): 1463-1474.

Hart, B. S. (1995). "Porosity and Pressure - Role of Compaction Disequilibrium in the Developement of Geopressures in a Gulf-Coast Pleistocene Basin." Geology **23**: 45-48.

Hoesni, M. J. (2004). Origins of overpressure in the Malay Basin and its influence on petroleum systems, Durham. **Doctor of Philosophy**.

Holbrook, P. W., et al. (1995). "Real-Time Pore Pressure and Fracture Gradient Evaluation in All Sedimentary Lithologies." SPE Formation Evaluation **10**(04): 215-222.

Hottman, C. E., et al. (1979). "Relationship Among Earth Stresses, Pore Pressure, and Drilling Problems Offshore Gulf of Alaska." Journal of Petroleum Technology **31**(11): 1477-1484.

Hottmann, C. E. and R. K. Johnson (1965). "Estimation of Formation Pressures from Log-Derived Shale Properties." Journal of Petroleum Technology **17**(06): 717-722.

Hower, J., et al. (1976). "Mechanism of burial metamorphism of argillaceous sediment " Geological Society of America Bulletin **87**: 725-737.

Katahara, K. (2003). Analysis of Overpressure on the Gulf of Mexico Shelf. Offshore Technology Conference. Houston, Texas.

Katahara, K. (2006). "Overpressure and shale properties: stress unloading or smectite-illite transformation?" SEG Technical Program: 1520-1524.

Lahann, R. (2001). Influence of clay diagenesis on shale velocities and fluid pressure. Offshore Technology Conference. Houston, Texas.

Lane, R. A. and L. A. Macpherson (1976). "A Review of Geopressure Evaluation From Well Logs - Louisiana Gulf Coast." Journal of Petroleum Technology **28**(09): 963-971.

Law, B. E., et al. (1983). "Geologic Implications of Coal Dewatering." AAPG Bulletin **67**(12): 2255-2260.

Lesage, M., et al. (1991). "Pore-Pressure and Fracture-Gradient Predictions." Journal of Petroleum Technology **43**(06): 652-654.

Ludwig, W. J. (1970). Seismic refraction. The Sea,. A. E. Maxwell. New York, Wiley-Interscience. **4:** 53-84.

Luo, X. and G. Vasseur (1992). "Contributions of compaction and aquathermal pressuring to geopressure and the influence of environmental conditions." AAPG Bulletin **76**(10): 1550-1559.

Luo, X., et al. (2007). "Overpressure generation and evolution in a compressional tectonic setting." AAPG Bulletin **91**: 1123-1139.

Magara, K. (1980). "Comparison of porosity-depth relationships of shale and sandstone." Journal of Petroleum Technology **3**: 175-185.

Martinez, R. D., et al. (1991). "Formation Pressure Prediction With Seismic Data From the Gulf of Mexico." SPE Formation Evaluation **6**(01): 27-32.

Miller, T. W. (2002). "The interrelationships between overpressure mechanisms and in-situ stress." AAPG Bulletin **76**: 13-20.

Mouchet, J. and A. Mitchell (1989). Abnormal Pressures while Drilling. Boussens, France, Elf Aquitaine.

Neuzil, C. (1995). "Abnormal pressures as a hydrodynamic phenomena." American Journal of Science **295**: 742-786.

Osborne, M. and R. E. Swarbrick (1997). "Mechanisms for generating overpressure in sedimentary basins." AAPG Bulletin **81**: 1023-1041.

Osborne, M. and R. E. Swarbrick (1999). "Diagenesis in North Sea NPHT " Marine and Petroleum Geology **16**: 337-353.

Pennebaker, E. S. (1968). Detection Of Abnormal-Pressure Formation From Seismic Field Data. Drilling and Production Practice. New York, New York, American Petroleum Institute**:** 8.

Pennebaker, E. S. (1968). "An Engineering Interpretation of Seismic Data." Society of Petroleum Engineers.

Satti, I. A., et al. (2015). "Origin of Overpressure in a Field in the Southwestern Malay Basin." SPE Drilling & Completion **30**(03): 198-211.

Sayers, C. M., et al. (2002). Pore pressure prediction for the Cocuite Field. SPE Annual Technical Conference. San Antonio, Texas, Society of Petroleum Engineers.

Sayers, C. M., et al. (2000). "Predrill Pore Pressure Prediction Using Seismic Data." Geophysics **67**(4): 1286-1292.

Sayers, C. M. and M. J. Woodward (2002). "Predrill Pore Pressure Prediction Using 4C Seismic Data." The Leading Edge(February).

Serebryakov, V., et al. (1995). "Methods of estimating and predicting abnormal formation pressures." Journal of Petroleum Science and Engineering **13**: 113-123.

Smith, J. E. (1973). "Shale Compaction." Society of Petroleum Engineers Journal **13**(01): 12-22.

Spencer, C. W. (1987). "Hydrocarbon generation as a mechanism for overpressuring in rocky mountain region." AAPG Bulletin **71**: 368-388.

Steffy, D. (1991). Abnormal Formation Pressures in the Navarin Basin, Bering Sea, Alaska, U.S. Department of the Interior Minerals Management Service**:** 79.

Swarbrick, R. E. (2002). "Challenges of Porosity-Based Pore Pressure Prediction." CSEG Recorder **27**(7): 74-77.

Swarbrick, R. E. and M. Osborne (1998). "Mechanisms that generate abnormal pressures: an overview." AAPG Memoir **70**: 13-34.

Terzaghi, K. (1943). Theoretical Soil Mechanics, John Wiley and Sons.

Tingay, M. (2007). "Vertically transferred overpressures in Brunei: evidence for a new mechanism for the high magnitude overpressure." Marine and Petroleum Geology **35**: 1023.

Tingay, M. (2013). "Evidence for overpressure generation by kerogen-to-gas maturation in the northern Malay Basin." AAPG Bulletin **97**: 639-672.

Tingay, M., et al. (2009). "Origin of overpressure and pore-pressure prediction in the Baram province, Brunei." AAPG Bulletin **93**(1): 51-74.

Traugott, M. (1997). "Pore/fracture pressure determinations in deep water." World Oil **August 1997**.

Turner, R. (1984). Geological and Operational Summary Navarin Basin Cost No 1 Well. Alaska, United States Department of the Interior. **MMS 84-0031**.

Turner, R. (1985). Geological Report for the Navarin Basin, United States Department of the Interior. **MMS 85-0045:** 164.

van Ruth, P., et al. (2004). "The origin of overpressure in the Carnarvon Bain, Western Australia: implications for pore pressure prediction." Petroleum Geoscience **10**: 247-257.

Velde, B. and G. Vasseur (1992). "Estimate of the diagenetic smectite to illite transformation in time temperature space." American Mineralogist **77**: 967-976.

Wallace, W. E. (1965). "Abnormal Subsurface Pressures Measured From Conductivity Or Resistivity Logs." The Log Analyst **5**(04): 17.

Worrall, D. M. (1991). "Tectonic History of the Bering Sea and the Evolution of Tertiary Strike-Slip Basins of the Bering Shelf."

Xu, J., et al. (2014). "Origins of marginal basins of the NW Pacific." Earth Science Reviews **130**: 154-196.

Yassir, N. A. and J. S. Bell (1996). "Abnormally High Fluid Pressures and Associated Porosities and Stress Regimes in Sedimentary Basins." SPE Formation Evaluation **11**(01): 5-10.

Zhang, J. (2011). "Pore Pressure prediction from well logs: Methods, modifications, and new approaches." Earth Science Reviews **108**(1-2): 50-63.

Zhang, J. (2013). "Effective stress, porosity, velocity and abnormal pore pressure prediction accounting for compaction disequilibrium and unloading." Marine and Petroleum Geology **45**(August 2013): 2-11.

Zhang, J. and J. Wieseneck (2011). Challenges and Surprises of Abnormal Pore Pressures in the Shale Gas Formations. SPE Annual Technical Conference and Exhibition. Denver, Colorado, USA, Society of Petroleum Engineers**:** 9.

Appendix A

Crossplots for non overpressured wells

Density velocity crossplots for well 560 George show an increasing density and increasing velocity trend within the established bounds (Figure 72, Figure 73). The density velocity data follows a normal compaction trend when organized according to depth (Figure 72). The density velocity data again follows a normal compaction trend when organized by mudweight; the compaction trend continues with increasing density and velocity as mudweight increases (Figure 73). Density resistivity crossplots do not show a somewhat normal compaction trend and are not as reliable as the density velocity crossplots (Figure 74, Figure 75). Overall, well 560 George shows evidence of normal compaction and thus disequilibrium compaction when density velocity crossplots are analyzed.

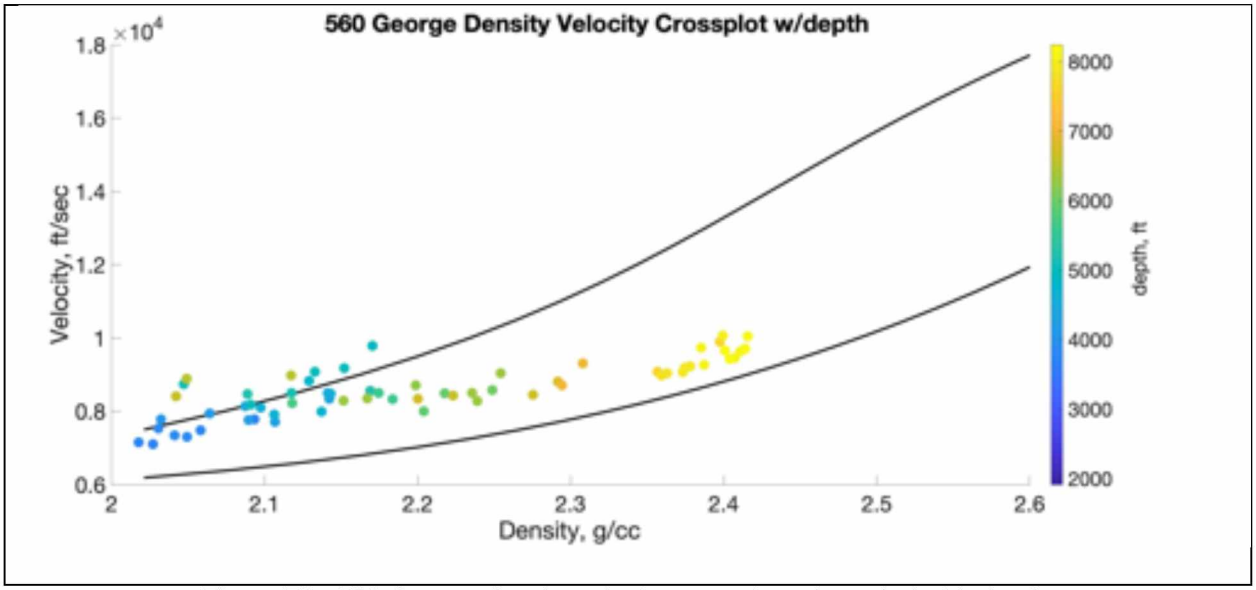

Figure 72. 560 George density velocity crossplot colorcoded with depth.

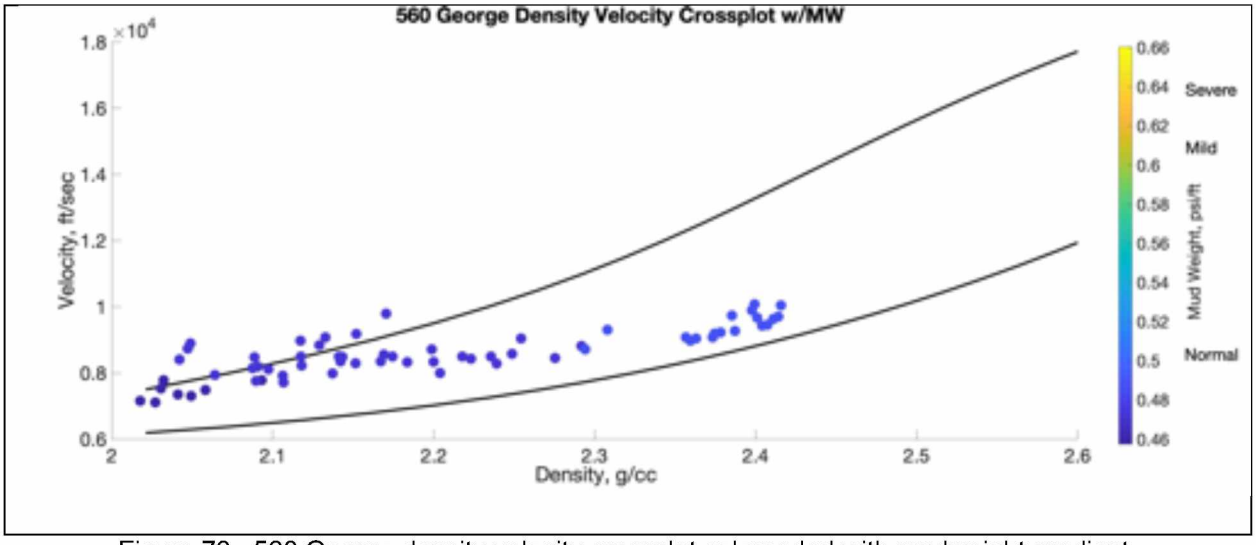

Figure 73. 560 George density velocity crossplot colorcoded with mudweight gradient.

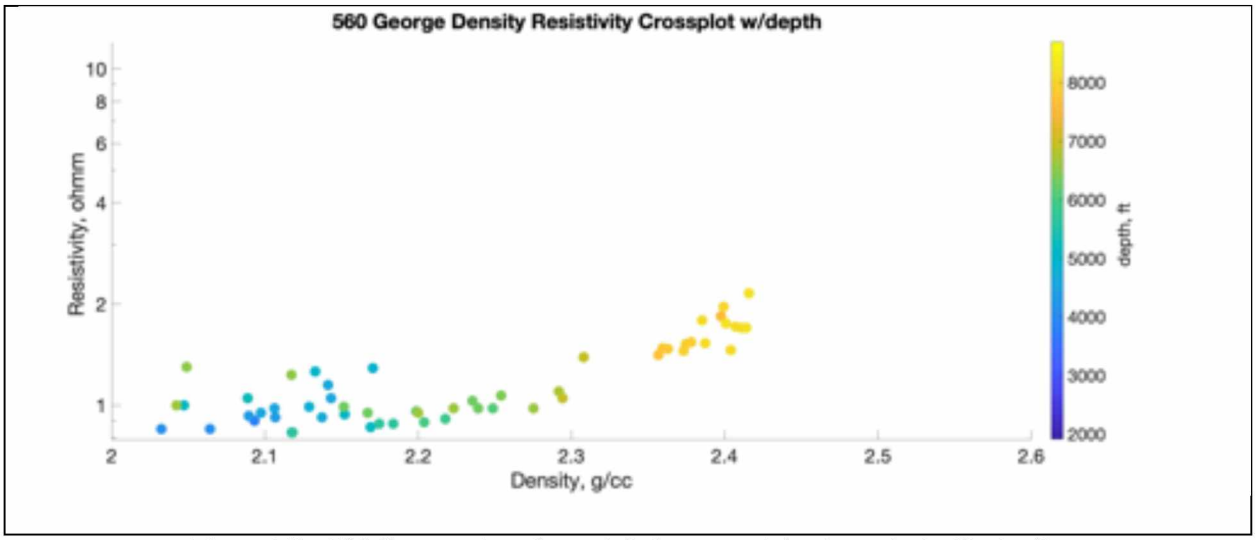

Figure 74. 560 George density resistivity crossplot colorcoded with depth.

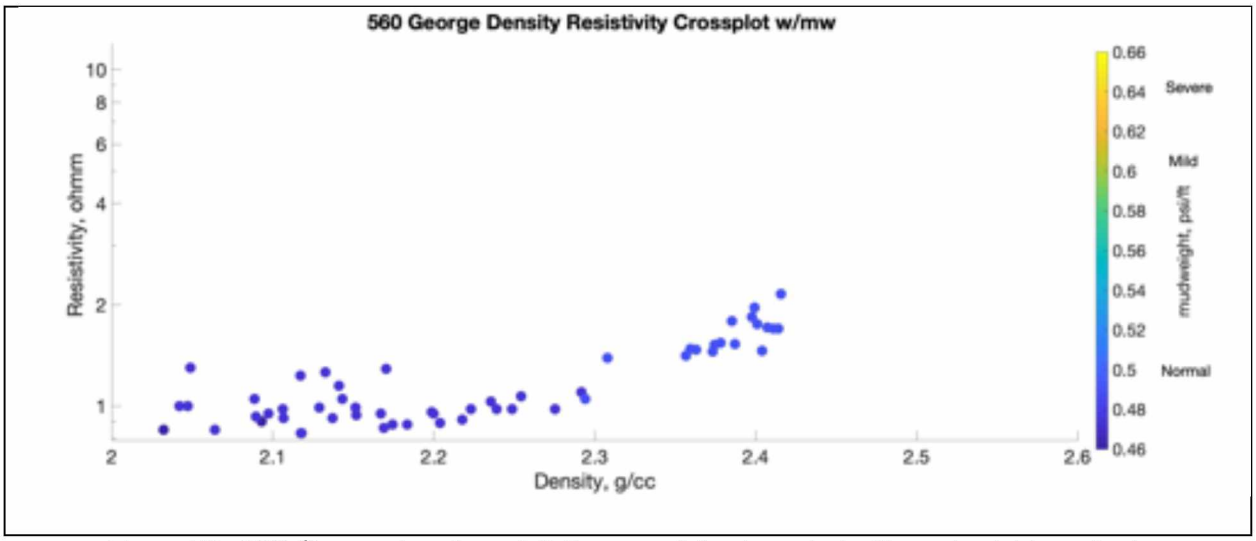

Figure 75. 560 George density resistivity crossplot colorcoded with mudweight gradient.

Density velocity crossplots for well 639 Danielle show the data following a compaction trend within the upper and lower bounds as depth and pressure increase (Figure 76, Figure 77). The density resistivity crossplots are not as reliable and do not show very clear patterns between density and resistivity (Figure 78, Figure 79). Although the density and velocity data continue to increase with depth, there is evidence that the trend slows with depth as there is an aggregate of similar density and velocity values at greater depths. This could signify that compaction has slowed due to water retention in the formation. Additionally, there is the absence of any fluid expansion trends in the density velocity crossplots (Figure 18). It is reasonable to conclude that the mechanism for overpressure in well 639 Danielle is identified as disequilibrium compaction.

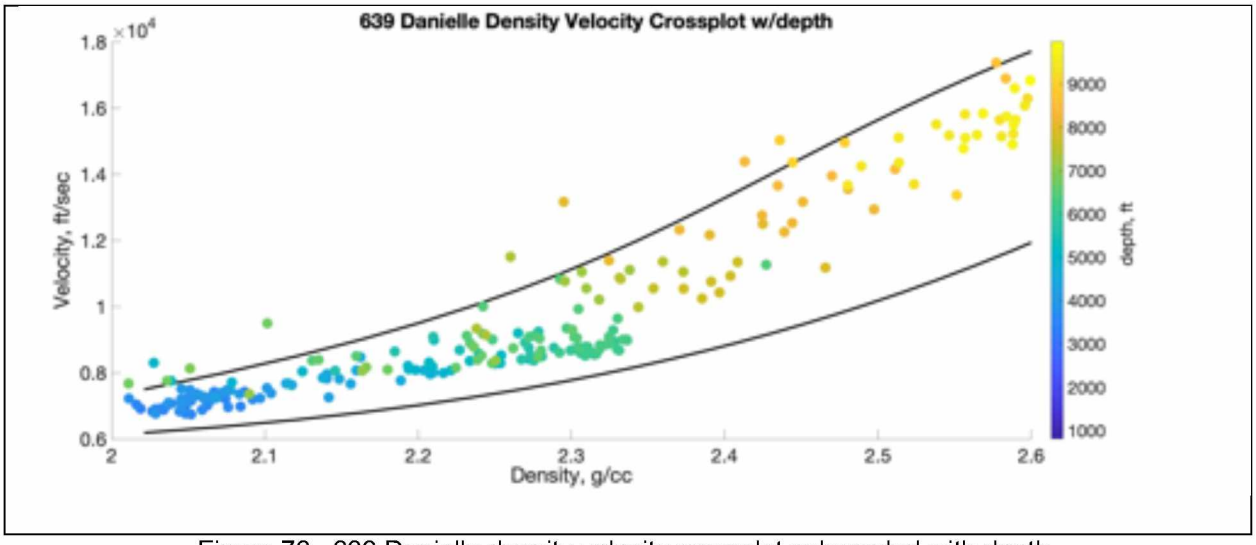

Figure 76. 639 Danielle density velocity crossplot colorcoded with depth.

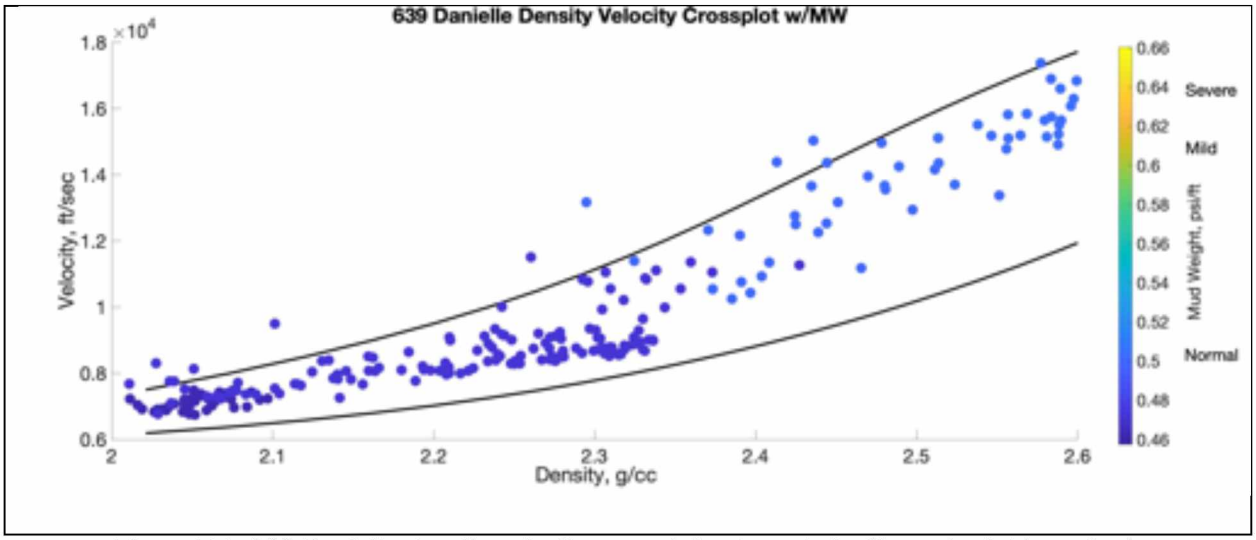

Figure 77. 639 Danielle density velocity crossplot colorcoded with mudweight gradient.

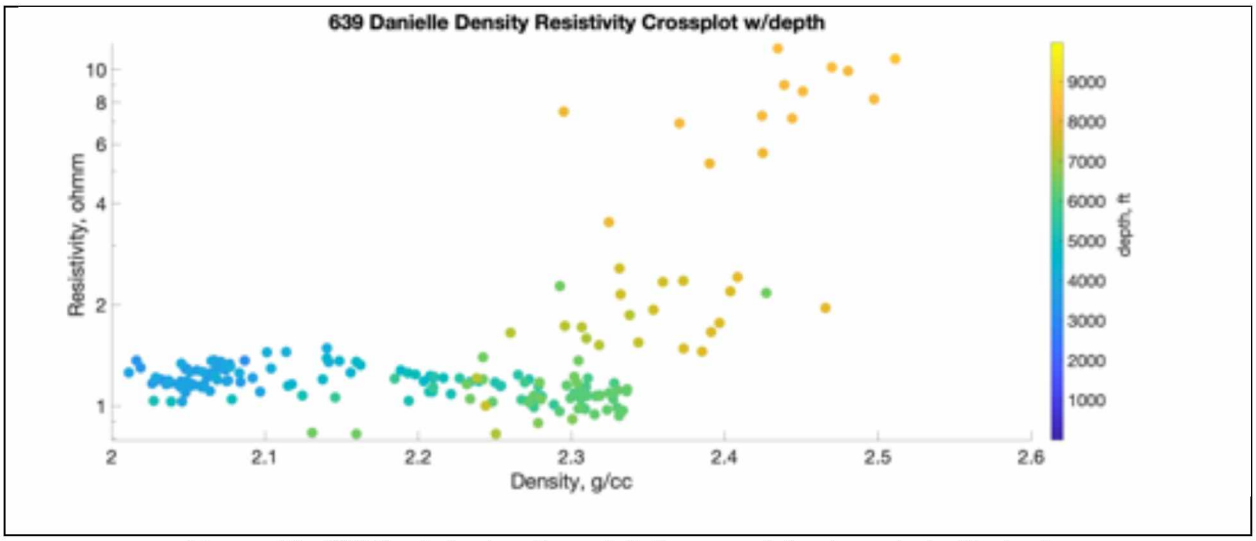

Figure 78. 639 Danielle density resistivity crossplot colorcoded with depth.

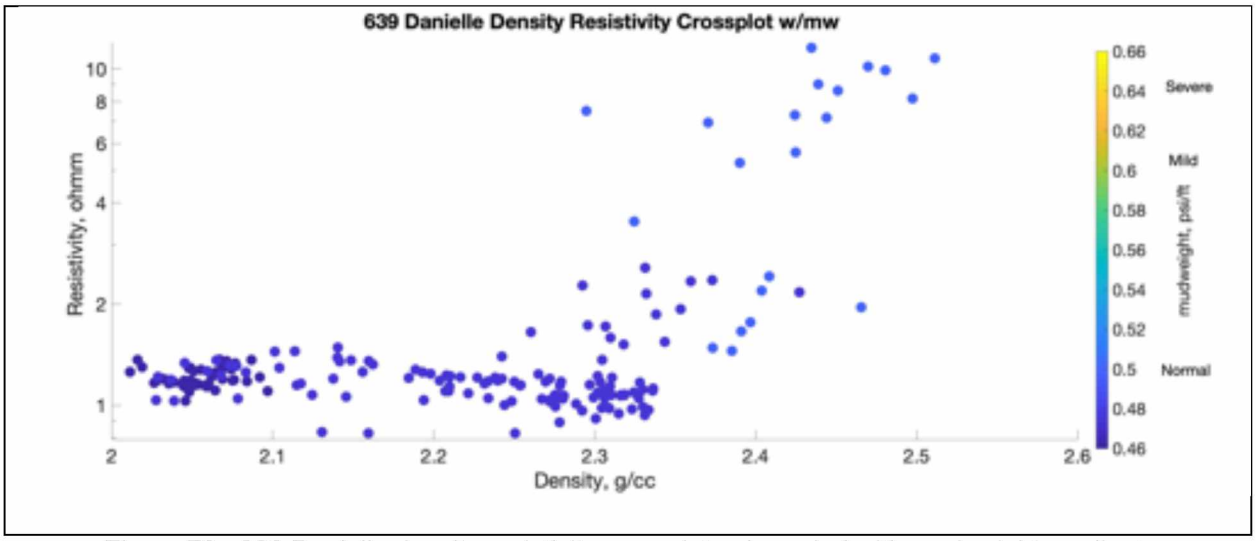

Figure 79. 639 Danielle density resistivity crossplot colorcoded with mudweight gradient.

Density velocity crossplots for Well 673 Misha show a clear compaction trend within upper and lower bounds where the velocity and density increase with depth and mudweight (Figure 80, Figure 81). The density resistivity crossplots show a similar clear compaction trend (Figure 82, Figure 83). There is an absence of any of the characteristics of fluid expansion overpressure generation from the density velocity crossplots (Figure 18). Since the density and velocity data fit entirely within the bounds, following a normal compaction trend, and failing to exhibit any characteristics of fluid expansion overpressure generation, it is reasonable to conclude that the mechanism for overpressure generation in well 673 Misha is most likely disequilibrium compaction.

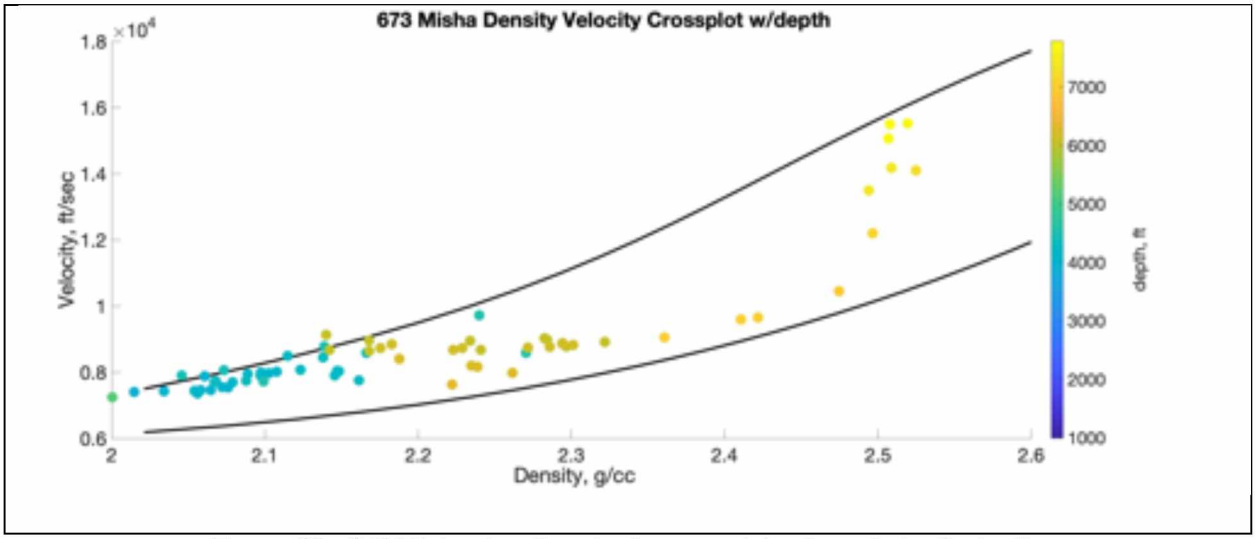

Figure 80. 673 Misha density velocity crossplot colorcoded with depth.

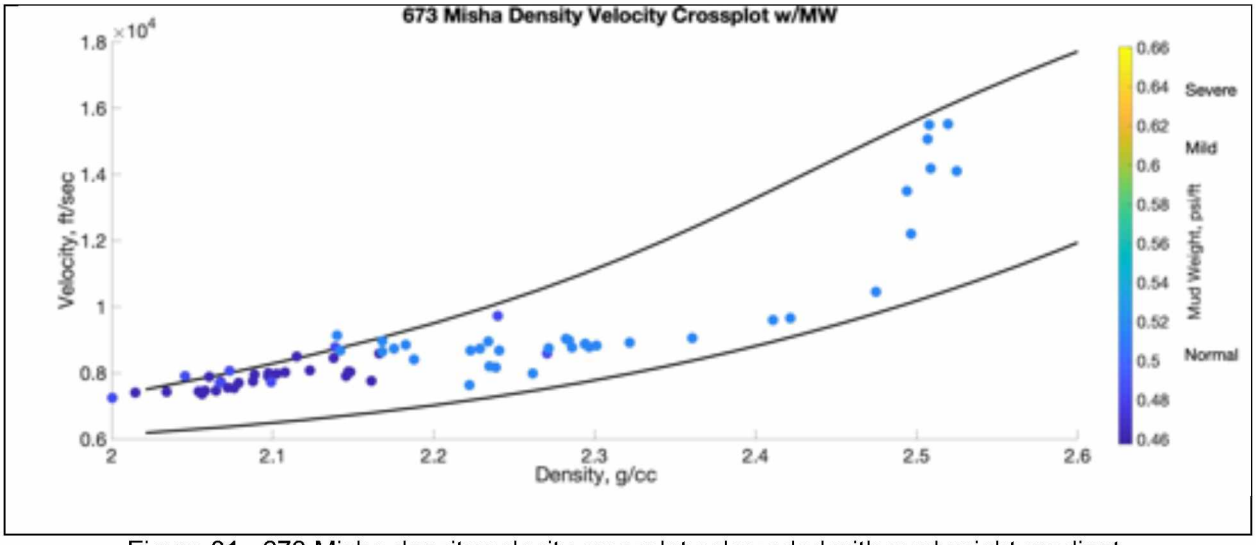

Figure 81. 673 Misha density velocity crossplot colorcoded with mudweight gradient.

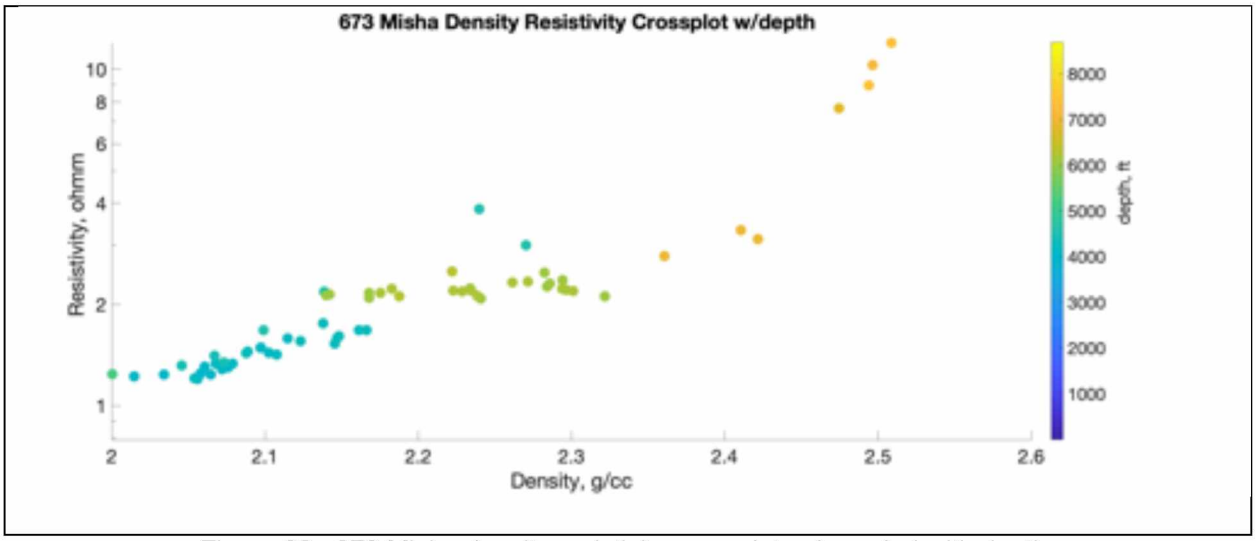

Figure 82. 673 Misha density resistivity crossplot colorcoded with depth.

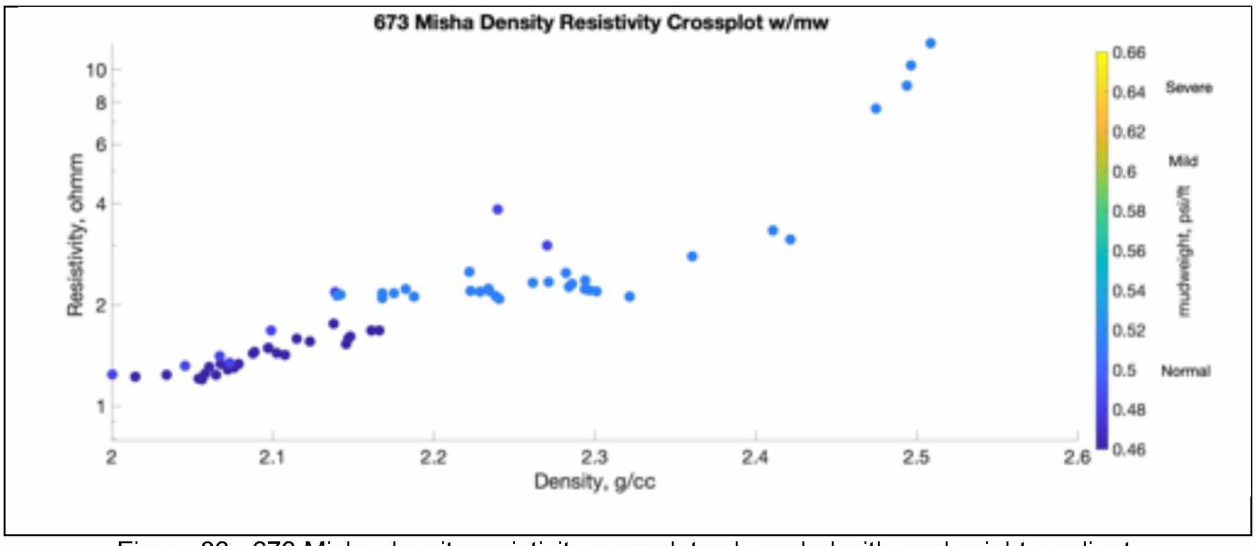

Figure 83. 673 Misha density resistivity crossplot colorcoded with mudweight gradient.

Density velocity crossplots for well 707 Nicole show a clear compaction trend within upper and lower bounds where the velocity and density increase with depth and mudweight (Figure 84, Figure 85). The density resistivity crossplots do not show any clear trend or organization of the data and are not reliable (Figure 86, Figure 87). There is an absence of any of the characteristics of fluid expansion overpressure generation from the density velocity crossplots (Figure 18). Since the density and velocity data fit entirely within the bounds, following a normal compaction trend, and failing to exhibit any characteristics of fluid expansion overpressure generation, it is reasonable to conclude that the mechanism for overpressure generation in well 707 Nicole is most likely disequilibrium compaction

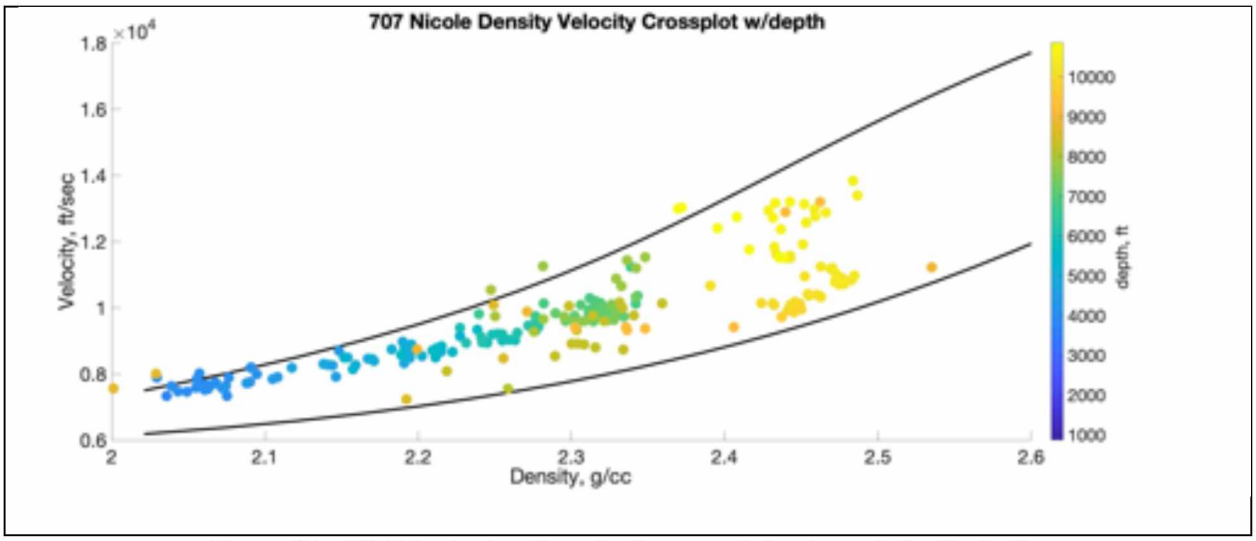

Figure 84. 707 Nicole density velocity crossplot colorcoded with depth.

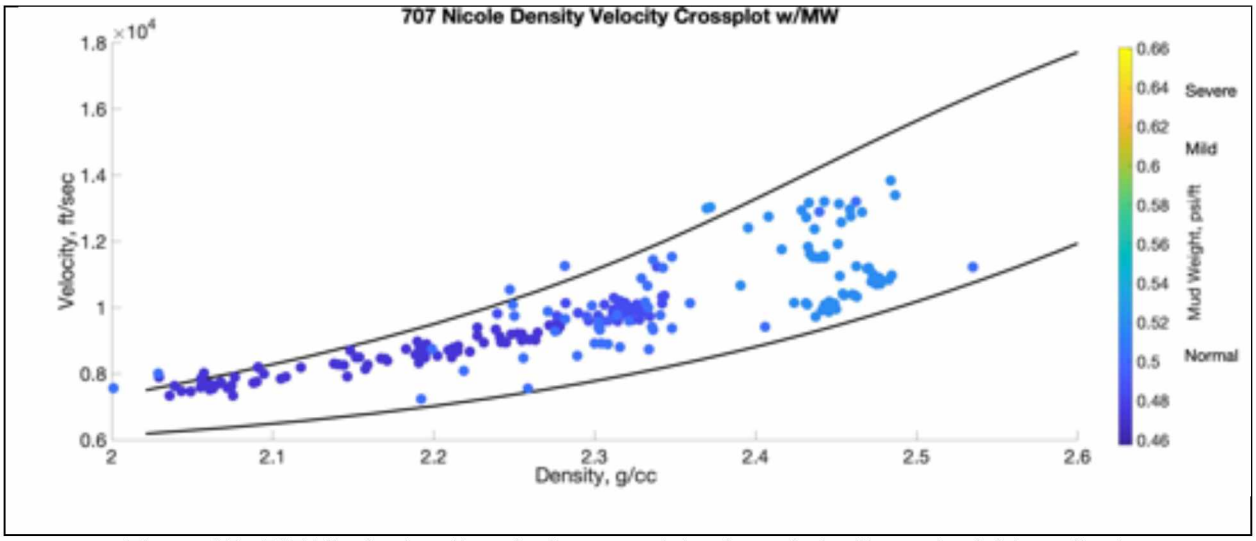

Figure 85. 707 Nicole density velocity crossplot colorcoded with mudweight gradient.

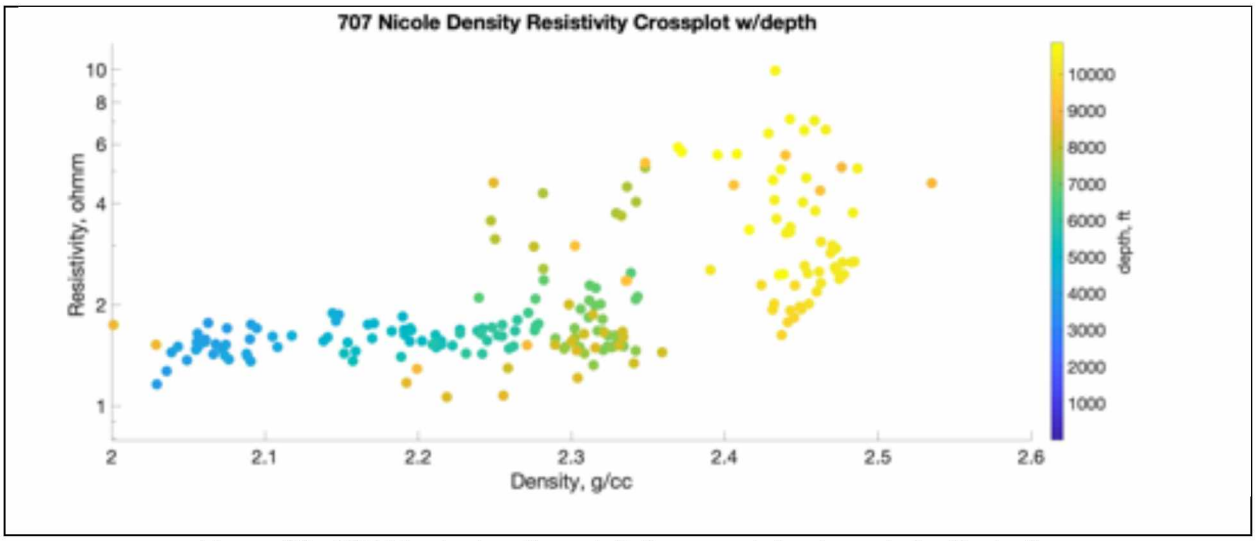

Figure 86. 707 Nicole density resistivity crossplot colorcoded with depth.

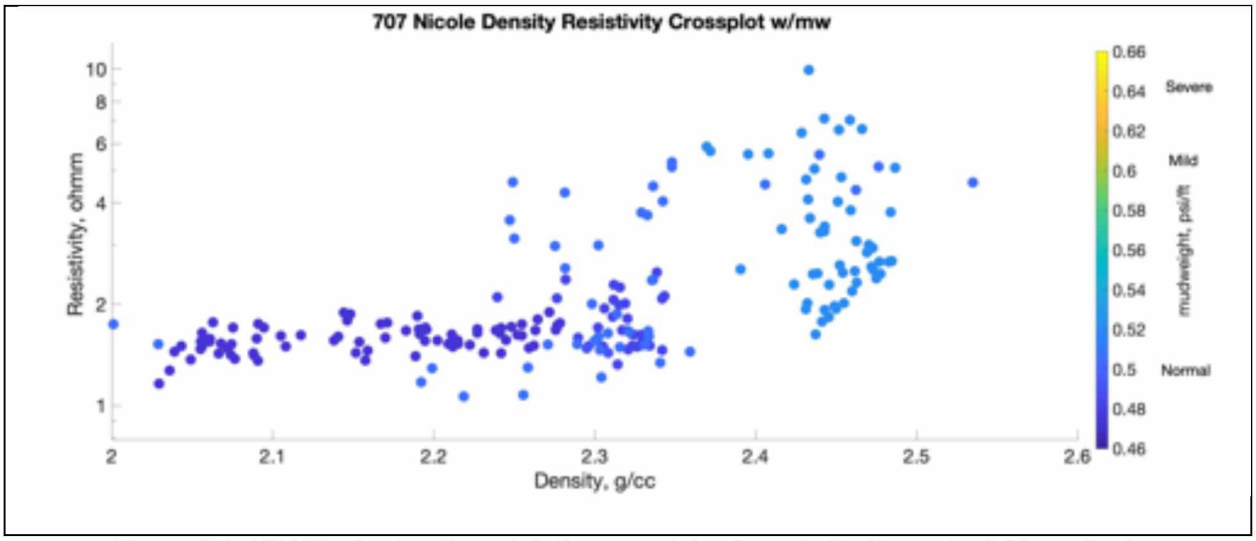

Figure 87. 707 Nicole density resistivity crossplot colorcoded with mudweight gradient.

Appendix B

Pressure Prediction for non overpressured wells

The pore pressure prediction results for well 560 George for the Eaton and Bowers methods are shown in Figure 88. The normal compaction trend line from the sonic velocity data (Figure 65) was used to calculate normal velocity values since the curve accurately fit the sonic velocity data for well 560 George. Figure 88 shows an increase in pore pressure from 6,000 to 8,000 feet which around the Eocene age shale target formation where overpressure is expected.

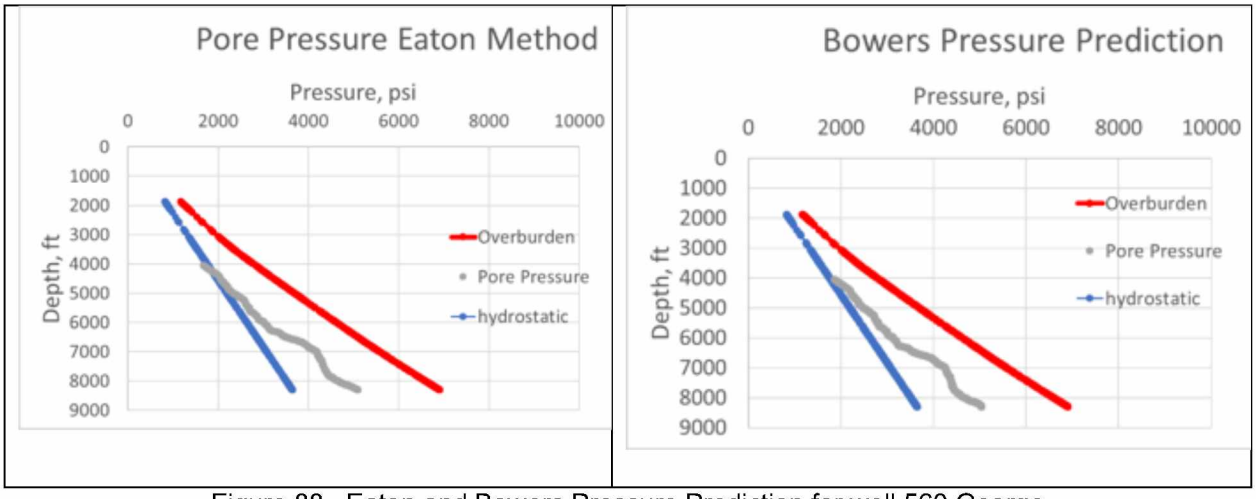

Figure 88. Eaton and Bowers Pressure Prediction for well 560 George

The pore pressure prediction values for well 639 Danielle (Figure 89) and well 673 Misha (Figure 90) show no observable patterns for an increase at depth. The normal

compaction trends from sonic velocity (Figure 65) were utilized to calculate pore pressure that show an increase at depth.

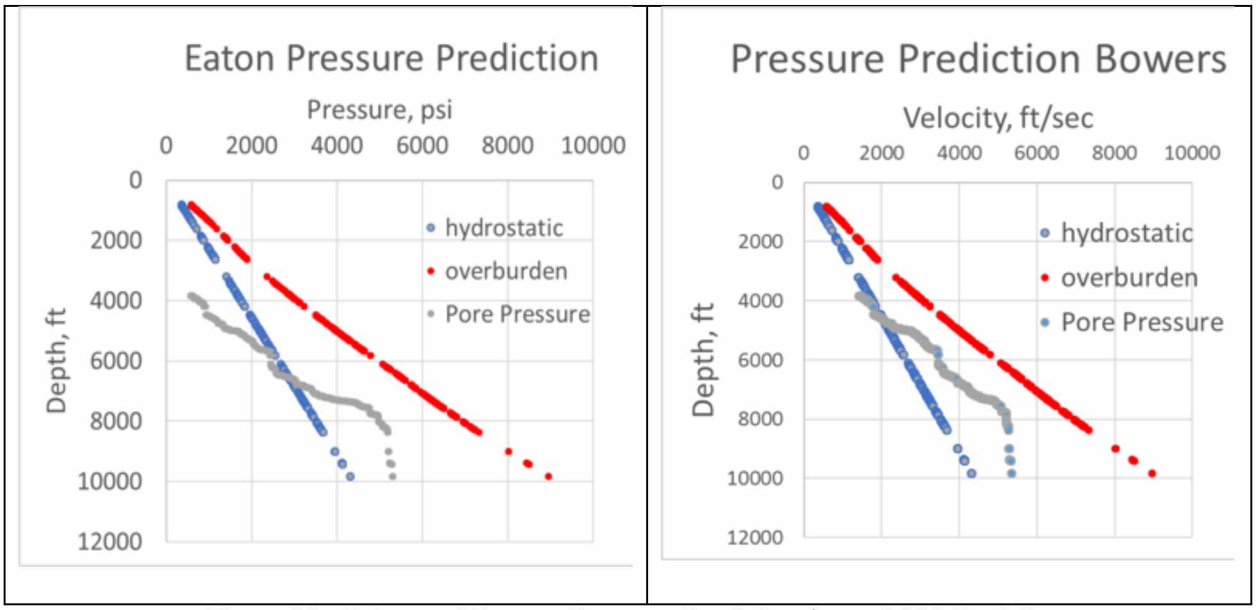

Figure 89. Eaton and Bowers Pressure Prediction for well 639 Danielle

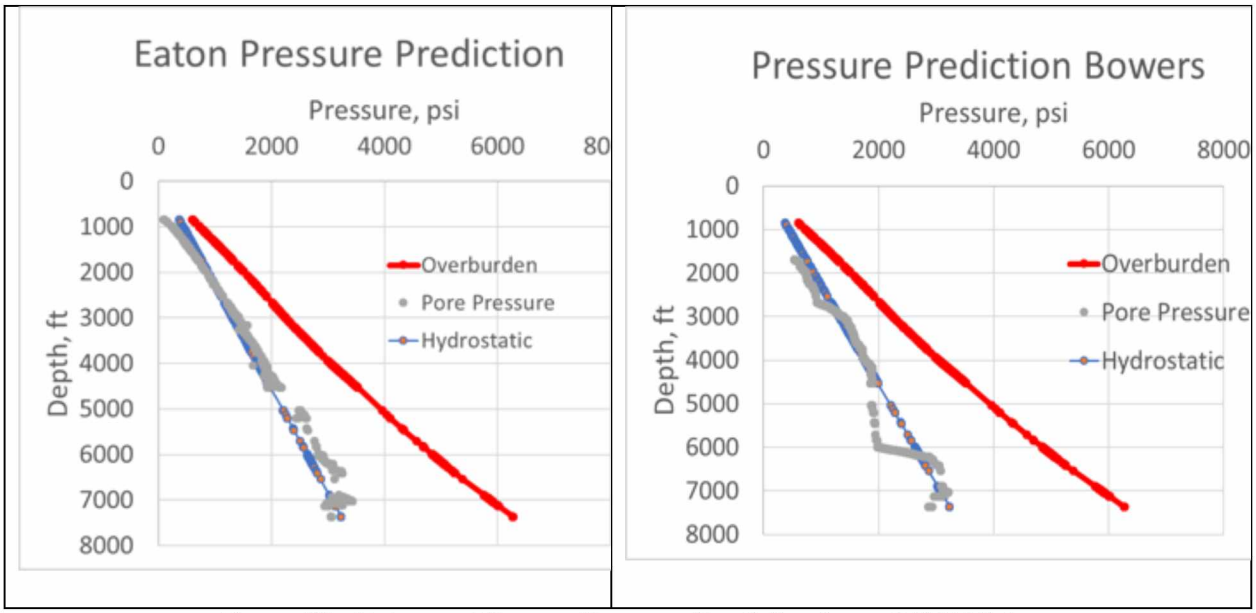

Figure 90. Eaton and Bowers Pressure Prediction for well 673 Misha

The pore pressure prediction results for well 707 Nicole for the Eaton and Bowers methods are shown in Figure 91. The normal compaction trend line from the sonic velocity data (Figure 65) was used to predict the normal sonic velocity values. Figure 91 shows an increase in pore pressure from 8,000 to 10,000 feet at the expected target formation.

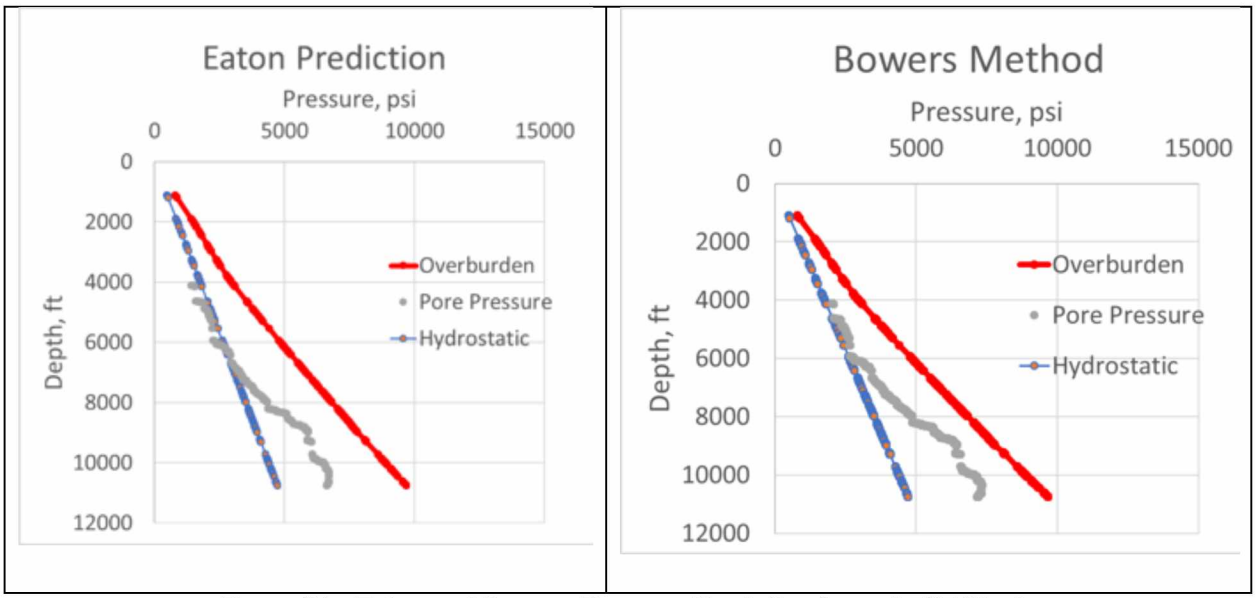

Figure 91. Eaton and Bowers Pressure Prediction for well 707 Nicole